UNIVERSITY OF TWENTE.

MASTER THESIS

# Dissolution modes of droplets on patterned surfaces

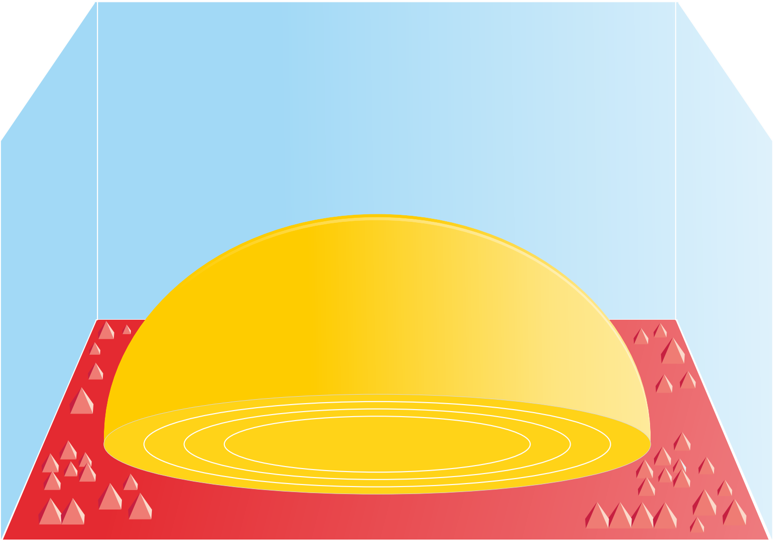

*Author:*
BSc. IGNAAS JIMIDAR

*Supervisors:*
Prof. Dr. JENS HARTING
Dr. ir. ERIK DIETRICH

*Committee:*
Prof. Dr. DETLEF LOHSE
MSc. SHANTANU MAHESHWARI
Dr. STEFAN KOOIJ

19th of August, 2016

Physics of Fluids

## Abstract

Evaporating droplets have many applications within the industry and droplets evaporating in air have been extensively studied. However droplets surrounded by another liquid have been studied less. Due to the emergence of the micro- and nanotechnology many research groups have shown interest in the contact line dynamics of surface nanodroplets and nanobubbles. Understanding of the contact line dynamics will be beneficial and relevant to diverse industries. Surface droplets dissolve in four different modes: the constant radius (CR) mode, the constant contact angle (CA) mode, the stick-slide mode and the stick-jump mode.

In this thesis we study the dissolution of these sessile droplets both numerically and experimentally. We employ the lattice Boltzmann model together with an evaporation model that has been developed by Hessling et al. [1] to study the contact line dynamics of dissolving sessile droplets on chemically patterned surfaces. At first we study a droplet placed in the system center in still fluid, i.e. we study the classical Epstein-Plesset [2] problem. From this benchmark we learn that the measured diffusion constant is not equal to the actual diffusivity in the system. We find that as the distance of the droplet to the boundary of the system increases, the measured diffusivity gets smaller. This is due to the infinite system size assumption in the theory.

By patterning surfaces we are able to study the dissolution modes of surface droplets. We achieve the CA mode by simulating droplets on flat surfaces with different wettability. We simulate droplets dissolve in the CR mode, by depositing the droplet on a hydrophylic disk, and the droplet gets pinned at the rim of the hydrophylic disk. The rest of the surface is hydrophobic. When the droplet depins, the droplet further dissolves in the CA mode. Thus this resembles what we call the stick-slide mode. We find that the droplets dissolve faster in the CR mode than the CA mode. We then continue by patterning the surface with concentric rings, which consists of hydrophylic and hydrophobic rings. We deposit the droplet on the outer most hydrophylic ring, and find that the droplet depins and thereafter “jumps” to the next available hydrophylic disk on the surface. This implies that the droplet dissolve in the stick-jump mode, if there are more hydrophylic disks on the surface.

Experimentally we prepare the samples with an chemical etching process which leads to pyramidal hillock formation on the samples. We measure the contact angle hysteresis. Due to random distribution of the pyramidal hillocks on the surface, the measurements result in a large spread of the data, i.e. we do not find any consistent result between etching time and contact angle hysteresis. On average the hysteresis does increase after etching the samples. Furthermore from dissolution experiments we find that the droplets solely dissolve in the stick-slide mode and the stick-jump mode. Also from this data we do not find any consistency between pinning behaviour and etching time of the samples.

**Key words:** dissolving sessile droplets, contact line dynamics, lattice Boltzmann model, surface roughness, contact angle hysteresis

# Contents

# CHAPTER 1

# Introduction

## 1.1 General Overview

Evaporating droplets in air have been studied extensively [3–6]. However systems where the droplet is surrounded by another liquid have been studied less. These systems are completely analogous to the liquid droplets in air systems and if both processes are diffusion controlled, they can be solved using the same equations [7]. Applications of evaporating droplets are found in controlling the deposition of particles on solid surfaces, in ink-jet printing, spraying of pesticides, thin film coatings, biochemical assays, drop wise cooling, deposition of DNA/RNA micro-arrays, and manufacture of novel optical and electronic materials in the last decades [3, 8]. With the emergence of micro- and nanotechnology, many research groups have also shown interest in the contact line dynamics of surface nanodroplets and nanobubbles. These nanodroplets can for instance spontaneously form in oil-water emulsions on solid surfaces [9]. Understanding the contact line dynamics of surface micro- and nanodroplets will lead to a diverse set of industrially important materials such as textile or biomedical micro- and nanofibers, powdered solids, and topographically or chemically nanopatterned surfaces, nanoassembly, modern biotechnology as well as micro- and nanoscale devices, with relevance in diverse industries from biomedical to petroleum engineering [10, 11]. The wetting of structured surfaces is also important in the area of microfluidics and microelectronics, printing and self-cleaning materials [12, 13].

Studies on both types of systems, droplets in air and droplets surrounded by another liquid, show that droplets dissolve in different modes with different life times [3, 5–7]. The pinning of the three-phase contact line during the stick phases is of crucial importance for the long (stable) life time of nanobubbles and nanodroplets [6, 14]. The pinning during experiments is caused by chemical or physical (geometrical) heterogeneities, which are naturally omnipresent on the surface and can be avoided to some extent only. On the other hand surface heterogeneities need to be explicitly introduced during numerical simulations, i.e. numerical simulations give us the opportunity to study droplets on ideal and non-ideal surfaces. Another characteristic property of the surface heterogeneities is that they enhance the contact angle hysteresis of sessile droplets. Apart from the three modes that are known, namely: (a) the constant radius (CR) mode, (b) the constant contact angle (CA) mode, and (c) the stick-slip mode, recently Zhang et al. [7] and Dietrich et al. [5] have reported a new mixed mode that they have observed experimentally for dissolving nanodroplets, namely the stick-jump mode (see fig. 1.1). In this mode the droplet "jumps" from the contact angle at the end of the first stick phase to a higher contact angle in a very short amount of time. Contrary to what the name "suggests", the droplet does not detach from the surface.

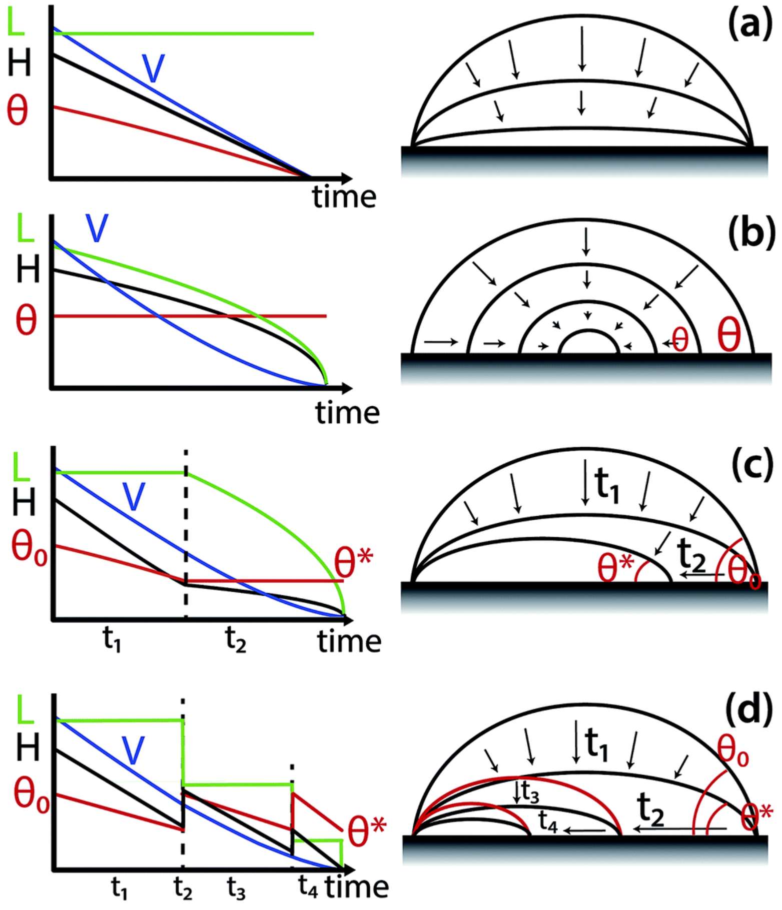

**Figure 1.1:** Schemes of the four possible dissolution modes of droplets: (a) the CR mode (b) the CA mode (c) the stick-slide mode and (d) the stick-jump mode. Here $V$ is the volume of the droplet with contact angle $\theta$, $H$ its height and $L$ the lateral diameter of the droplet. Figure taken from Zhang et al. [7]

To gain a better understanding of the dissolution modes of the experimentally observed droplets, we perform a numerical study on the contact line dynamics of droplets on flat chemically patterned substrates surrounded by another fluid. For this purpose we employ the lattice Boltzmann method. The lattice Boltzmann method is a mesoscale model which has developed into an alternative and promising numerical scheme for simulating fluid flows [15]. The method, with addition of multiphase and multicomponent models, is particularly successful in fluid flow applications which involve interfacial dynamics and complex boundaries, e.g., wetting and spreading phenomena [16], foams and emulsions [17]. The lattice Boltzmann method is based on microscopic models and mesoscopic kinetic equations. Its fundamental idea is to construct simplified kinetic models that incorporate the essential physics of microscopic or mesoscopic processes such that the properties obey the desired macroscopic equations [15]. To drive the diffusion process of the droplets during the numerical simulations, we need to incorporate a diffusion model. An evaporation model is developed by Hessling et al. [1]. They show that the lattice Boltzmann method extended with the Shan-Chen model follows the diffusion equation. The droplets in the numerical study are deposited on flat chemically heterogeneous surfaces that are immersed in a different liquid. The chemically patterned surfaces allow us to study the dissolving droplet dynamics numerically, because with this chemical patterning we closely mimic the different pinning sites that droplets experience from the surface during experiments. The chemical patterning in simulations is achieved by creating disks or rings of different wettability with the aid of the Shan-Chen model.

This research is further extended experimentally by studying the behaviour of droplets on surfaces with physical heterogeneities. To reach this purpose, the samples are first prepared by an anisotropic wet chemical etching process for different amounts of time. We characterize the roughness of these samples and perform dissolution experiments on them.

## 1.2 Structure and Scope

In this thesis first the relevant theory on dissolving droplets and contact angle hysteresis is given in chapter 2. We then shed light upon the relevant theory of the lattice Boltzmann method and the evaporation model developed by Hessling et al. [1] in chapter 3. In chapter 4 we continue with the numerical study to understand how pinning affects the contact line dynamics of dissolving droplets. To test the consistency of the evaporation model [1], we perform simulations on free spherical droplets in still fluid, i.e. we study a classical problem first solved by Epstein and Plesset [2] for bubbles. After a parametric study on these free spherical droplets, we carry on with the dissolving droplets on chemically patterned substrates. In practice it is difficult to observe droplets dissolving in the CA and the CR mode, due to different pinning sites which are omnipresent on the surface. Numerically we can achieve these modes easily, because we can create surfaces such that droplets dissolve in these modes. We also perform simulations on droplets dissolving in the mixed modes. When are droplets dissolving in the stick-slide mode and when are they dissolving in the stick-jump mode? Or is the stick-jump mode not always observed due to experimental limitations? The numerical results are compared to analytical solutions from the theory. Finally we give the conclusions on the numerical part at the end of chapter 4. To investigate how roughness affects the contact line dynamics of dissolving droplets, we also perform experiments on surfaces with roughness. We apply this roughness by a chemical etching process. In chapter 5 we first describe this etching process and the experimental set-ups used during the experiments. First the set-up employed during the dissolution experiments is described, continued by the set-up used for the measurement of contact angle hysteresis. We determine this contact angle hysteresis implicitly by performing advancing and receding contact angle (ARCA) measurements. Does the amount of etching time influences the roughness on the surfaces and if so, is the hysteresis increased and can we predict if a droplet dissolves in a certain mode base on their hysteresis? In chapter 6 we first discuss the images of the samples taken with a Scanning Electron Microscope (SEM) and optical microscope. We then move on to the results of the ARCA measurements, which characterize the roughness of the samples. The results for the dissolution experiments are presented and discussed and we give the conclusions on the experimental part at the end of chapter 6. In chapter 7 we summarize the conclusions and compare the results of the numerical and experimental part and some recommendations for further research follow at last.

# CHAPTER 2

## Theory

### 2.1 On contact angle hysteresis

Wetting phenomena have been studied extensively over the past decades and are ubiquitously present in our daily lives, e.g. raindrops rolling down on windows, drops sitting on leaves, paints, wetting of the eye, spreading of creams on the skin, etc. [18]. Wetting refers to the study of how a liquid deposited on a solid(liquid) spreads out and three phases are involved at the contact line, e.g. it can explain us why water spreads out on clean glass but not on a plastic sheet. Understanding wetting phenomena enables us to modify surfaces from wettable to non-wettable or vice-versa. We call the surface wettable if the liquid has a (strong) affinity for the solid. It is widely known that if we place a droplet on a clean, solid surface, we can observe a contact angle $\theta_Y$ which is given by Youngs' relation [19] and depicted in fig. 2.1 for a wetting and a non-wetting fluid as

$$\cos(\theta_Y) = \frac{\gamma_{SV} - \gamma_{SL}}{\gamma_{LV}}, \tag{2.1}$$

where $\gamma_{SV}$ is the surface tension between the solid and vapour, $\gamma_{SL}$ between the solid and the liquid and $\gamma_{LV}$ between the liquid and the vapour.

If the contact angle is smaller than 90°, we call the surface hydrophilic (fig. 2.1(a)) and otherwise hydrophobic (fig. 2.1(b)). However, in practice the apparent contact angle is mostly not equal to Young's angle $\theta_Y$ due to natural surface roughness [20]. Thus another parameter which controls wettability is surface roughness. Surface roughness can also be caused by defects on the surface making them a non-ideal surface. These defects can be of chemical nature (stains, blemishes) or physical (surface irregularities). On a non-ideal surface the static contact angle is not unique. The contact angle $\theta$ depends on the way the system has been prepared. If we inflate a droplet, and the contact line is not moving, $\theta$ can exceed $\theta_Y$. It does so until it reaches a threshold value $\theta_A$, called *advancing angle*, beyond which the contact line starts moving. The other extreme is when we deflate a droplet, $\theta$ can decrease to $\theta_R$, called *receding angle*, without

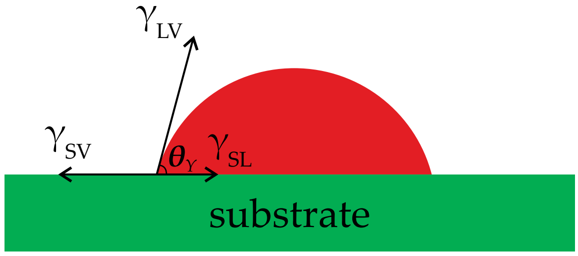

**(a)** Wetting fluid

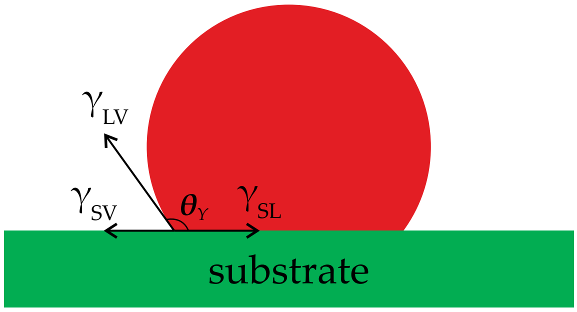

**(b)** Non-wetting fluid

**Figure 2.1:** Definition of the Young's angle $\theta_Y$ of a droplet sitting on a substrate as given in eq. (2.1).

any shift of the contact line. If the receding angle has reached the contact line moves. The difference in contact angle between these two limiting cases is called contact angle *hysteresis*. If the defects on the surfaces are strong enough, the contact line is pinned locally.

To model surface roughness Wenzel [21] and Cassie and Baxter [22] extended Young's model. Wenzel describes a state where the surface is completely covered by the liquid, whereas Cassie and Baxter describe a state where the vapour is enclosed between the liquid and rough surface. The transition between these two states also leads to the earlier mentioned hysteresis phenomena.

## 2.2 On dissolving droplets

Nanodroplets and nanobubbles have been of keen interest of many research groups in the recent years [6]. Surface nanodroplets are droplets at a solid-liquid interface that have at least one dimension smaller than a micrometer [7]. Due to the lens-shape of these droplets we can easily write down equations for the droplet's volume $V$ and its contact angle $\theta$ by means of geometric equations:

$$V = \frac{1}{24}\pi H(3L^2 + 4H^2), \tag{2.2}$$

$$\theta = \sin^{-1}\left(\frac{4LH}{L^2 + 4H^2}\right), \tag{2.3}$$

where $L$ is the lateral diameter of the droplet and $H$ its height as illustrated in fig. 2.2.

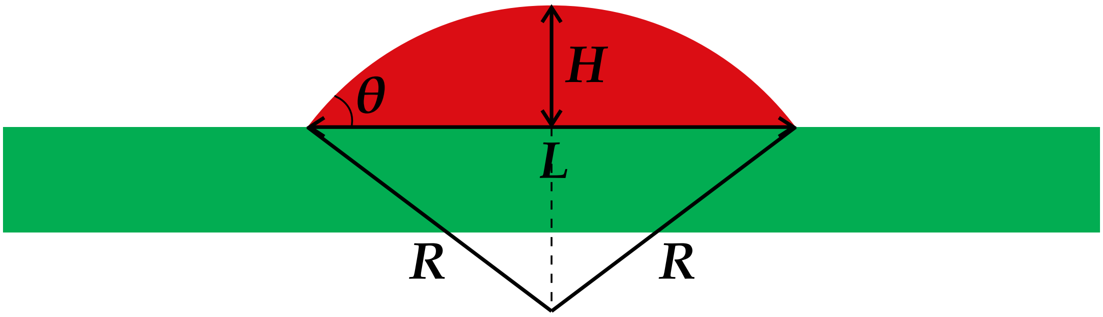

**Figure 2.2:** Geometry of a droplet sitting on a substrate with contact angle $\theta$, height $H$, lateral diameter $L$ and radius of curvature $R$.

Diffusion is the random motion of molecules to a region with a lower concentration of these molecules, i.e. a concentration gradient drives the diffusion process [23]. Due to the diffusion process e.g. sugar mixes (dissolves) up to saturation with water, droplets evaporate or soluble droplets dissolve in water.

Analogous to the system of evaporating water droplets in air, surface oil droplets dissolving in water can be studied. These oil droplets are immiscible in water. The solubility of alcohols depends on the length of their carbon chain [24]. The OH group(s) of alcohols is (are) polar and thus attracted to water and form(s) hydrogen bonds with neighbouring water molecules, whereas the carbon tails are non-polar and thus repelled by the polar water. These types of droplets do not mix with water and slowly dissolve in the water in the quasi-steady limit where diffusion is the rate-limiting mechanism. In this limit the diffusion equation governs the transport of molecules with a concentration field $c(r, z)$ around the droplet [7] as

$$\frac{\partial c}{\partial t} = D\nabla^2 c, \tag{2.4}$$

where $r$ and $z$ are the radial and vertical coordinates respectively and $D$ is the diffusion constant. The boundary conditions that are applicable to solve this problem are: at the droplet-water interface the concentration is equal to the saturation concentration $c_s$, secondly far away from the droplet as z $\rightarrow \infty$ the concentration field is equal to $c_\infty$ and the no-flux condition $\frac{\partial c}{\partial z}$ on the surface holds. Fick's first law also governs the diffusive flux $J = -D\nabla c$. Approximate solutions for the dissolution of droplets in the small contact angle regime have been first calculated by Deegan et al. [25] and Hu and Larson [26], whereas Popov [27] has used an elegant approach to solve this problem for all contact angles, i.e. he has solved this problem analogous to the electric potential around a charged lens-shaped conductor by introducing a correction factor $f(\theta)$ for the presence of the surface (substrate). This wall correction factor is depicted in fig. 2.3. The mass loss is given by [27]

$$\frac{dM}{dt} = -\frac{\pi}{2} LD(c_s - c_\infty) f(\theta), \tag{2.5}$$

where

$$f(\theta) = \frac{\sin(\theta)}{1+\cos(\theta)} + 4 \int_0^\infty \frac{1+\cosh(2\theta x)}{\sinh(2\pi x)} \tanh[(\pi-\theta)x] dx. \tag{2.6}$$

If steady state has been reached and given that the density $\rho$ does not change during dissolution, the mass of the droplet $M = \rho V$ can be expressed in terms of its contact angle (using equation (2.2) and (2.3)) as

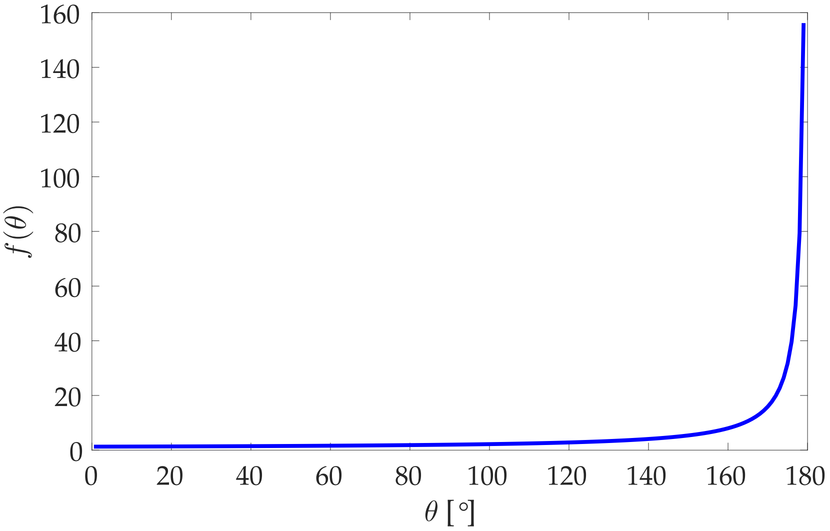

**Figure 2.3:** The wall correction factor $f(\theta)$ introduced by Popov [27] as a function of the contact angle $\theta$.

$$M(\theta) = \rho \frac{\pi}{8} L^3 \frac{\cos^3(\theta) - 3\cos(\theta) + 2}{3\sin^3(\theta)} = \rho \frac{\pi}{8} L^3 g(\theta). \tag{2.7}$$

From eq. (2.5) and (2.6) we can infer that the dissolution process timescale $\tau(L)$ is

$$\tau(L) = \frac{L^2 \rho}{8 D c_s}. \tag{2.8}$$

A direct implication of eq. (2.5) is that droplets of the same liquid and same volume, but different geometries (contact angles) have different lifetimes. Another parameter that influences the dissolution time is the undersaturation or oversaturation $\zeta$, which is defined as

$$\zeta = 1 - \frac{c_\infty}{c_s}. \tag{2.9}$$

This quantity has a maximum value equal to 1 if water or another liquid are initially not contaminated by the droplet's fluid, i.e. $c_\infty = 0$. It is equal to 0 if $c_\infty = c_s$, $\zeta < 0$ if the fluid is oversaturated and $\zeta > 0$ if the fluid is undersaturated. Thus in experiments the following cases can be studied: (i) droplets surrounded by fresh liquid which will be contaminated by the droplet's liquid during the experiment, (ii) droplets surrounded by a liquid that is saturated with the droplet's liquid, (iii) droplets surrounded by a liquid that is oversaturated with the droplet's liquid and (iv) droplets surrounded by a fresh liquid which is continuously being renewed (refreshed), which guarantees $c_\infty = 0$ apart from a transient effect in the beginning when there is still some contamination left from the droplet's liquid. In this thesis we explore the first case experimentally. During the experiments, the droplet is surrounded by a large amount of fluid, which enhances the droplet's dissolution. In the lattice Boltzmann numerical simulations, one could also simulate a droplet that is surrounded by a large amount of fluid, i.e. a much larger domain is needed, such that the droplet can dissolve in the system. However this requires more computing time. Thus in favour of computing time, we have implemented an evaporation model. This model will be further discussed in section 3.5.

The lifetime $t$ of dissolving droplets with an initial volume $V_0$ depends on their dissolution dynamics, which can be characterized by four modes. We non-dimensionalize the droplet's lifetime for these four modes as $\tilde{\tau} = \frac{t}{T}$, with

$$T = \left(\frac{3V_0}{2\pi}\right)^{\frac{2}{3}} \frac{\rho}{2D(c_s - c_\infty)}. \tag{2.10}$$

Picknett and Bexon [4] describe the two extreme modes that are possible: the constant contact angle mode and the constant radius mode. A combination of these two extreme modes is also possible. The dynamics of dissolving droplets can be characterized by four modes:

(i) *CA-mode*: In this mode the contact angle remains constant, i.e. $\theta = \theta_0$, while the lateral diameter changes as [7]

$$L(t) = \left({L_0}^2 - \frac{8(c_s - c_\infty)D}{\rho}\frac{f(\theta)}{3g(\theta)}t\right)^{1/2}. \tag{2.11}$$

It should be mentioned that apart from the wall correction factor $\frac{f(\theta)}{3g(\theta)}$ this solution is the same result as it was first derived by Epstein and Plesset [2] for an individual bubble in the bulk. When the droplet has a hemispherical shape, eq. (2.11) is the exact solution of Epstein and Plesset. We can find the lifetime of the droplet dissolving in the CA mode, $\tilde{\tau}_{CA}$ by integrating eq. (2.11) from $L_0$ to zero [3]:

$$\tilde{\tau}_{CA} = \left(\frac{2(1+\cos\theta_0)^2}{\sin\theta_0(2+\cos\theta_0)}\right)^{\frac{2}{3}} \frac{\sin\theta_0(2+\cos\theta_0)}{f(\theta_0)(1+\cos\theta_0)^2}. \tag{2.12}$$

(ii) *CR-mode*: In this mode the droplet remains pinned on the surface keeping its lateral diameter constant, i.e. $L = L_0$, while its contact angle is changing in time as

$$\frac{d\theta}{dt} = -\frac{4D(c_s - c_\infty)}{\rho L^2}(1+\cos(\theta))^2 f(\theta). \tag{2.13}$$

We can find the lifetime of the droplet dissolving in the CR mode, $\tilde{\tau}_{CR}$, by integrating eq. (2.13) from $\theta_0$ to $\theta_d$ [3]:

$$\tilde{\tau}_{CR} = \left(\frac{2(1+\cos\theta_0)^2}{\sin\theta_0(2+\cos\theta_0)}\right)^{\frac{2}{3}} \int_{\theta_d}^{\theta_0} \frac{2}{f(\theta)(1+\cos\theta)^2} d\theta. \tag{2.14}$$

(iii) *Stick-slide mode*: Several authors [4, 25–28] mention and confirm that in practise the evaporation or dissolution of droplets can be characterized by a mixed mode, one of which is the stick-slide mode. As the name already implies the dissolution process consists of "stick" phases, i.e. the contact line remains pinned (CR mode), and "slide" phases in which the contact line depins and the droplet dissolves further in the CA mode. These mixed modes occur when the initial contact angle $\theta_0$ of the droplet is higher than the receding (depinning) angle $\theta_d$. If the droplet reaches this receding angle, the contact line depins [3, 5]. Stauber et al. [3] describe the lifetime of a droplet evaporating in this mode. The key result of their work is the fact that the lifetime of the droplet dissolving in this mode is not constrained by the lifetimes of the droplet dissolving in the two extreme modes. The life time of the droplet dissolving in this mode can be calculated by superposing the time of the droplet dissolving in the CR mode (eq. (2.14)) and that of the droplet dissolving in the CA mode (eq. (2.12)):

$$\tilde{\tau}_{stick-slide} = \left(\frac{2(1+\cos\theta_0)^2}{\sin\theta_0(2+\cos\theta_0)}\right)^{\frac{2}{3}} \left[\int_{\theta_d}^{\theta_0} \frac{2}{f(\theta)(1+\cos\theta)^2} d\theta + \frac{\sin\theta_d(2+\cos\theta_d)}{f(\theta_d)(1+\cos\theta_d)^2}\right]. \tag{2.15}$$

(iv) *Stick-jump mode*: Recently Zhang et al. [7] mention another mixed mode in which a droplet can dissolve. They have experimentally observed that at the moment of depinning (during the slide phase), the contact angle and the height of the droplet increases, thus the droplet “jumps” from $\theta_d$ to $\theta_j$ as depicted in fig. 2.4. From experiments [5, 7] it is clear that the duration of this jump is very short. Dietrich et al. [5] predict the lifetime of a droplet dissolving in the stick-jump mode, where they follow the same route as Stauber et al. [3]. The experimental result for the contact angle $\theta$ in time for a droplet is depicted in fig. 2.4, with initial contact angle $\theta_0$ dissolving in the stick-jump mode. From this figure it is clear that the duration of the jump, from $\theta_d$ to $\theta_j$, is really short, thus mass loss can be neglected and the total dissolution time for the the stick-jump mode is modelled as consecutive dissolutions in the CR mode. They assume that during the jump the droplet jumps from $\theta_d$ to $\theta_j$ and returns to $\theta_d$ and also a different lateral diameter $L$ each time. The total dissolution time for a droplet dissolving in the stick-jump mode is [5]

$$\tilde{\tau}_{stick-jump} = \left(\frac{2(1+\cos\theta_j)^2}{\sin\theta_j(2+\cos\theta_j)}\right)^{\frac{2}{3}} \left[ \left( \int_{\theta_d}^{\theta_j} \frac{2}{f(\theta)(1+\cos\theta)^2} d\theta \right) \left(1 - \left(\frac{\sin\theta_d(2+\cos\theta_d)}{f(\theta_d)(1+\cos\theta_d)^2}\frac{(1+\cos\theta_j)^2}{\sin\theta_j(2+\cos\theta_j)}\right)^{\frac{2}{3}}\right)^{-1}\right]. \qquad (2.16)$$

Shanahan [28] has derived a theory for the maximum excess free energy $\delta\tilde{G}$ per unit length associated with the jump from $\theta_d$ to $\theta_j$, i.e. he has modelled the pinning of the contact line as an energy barrier $U$,

$$\delta\tilde{G} = \frac{\gamma L(\delta\theta)^2}{4(2+\cos\theta_j)}, \qquad (2.17)$$

where $\gamma$ is the interfacial tension, $\delta\tilde{\theta} = \theta_j - \theta_d$. The contact line only depins if $\delta\tilde{G}$ exceeds the pinning energy barrier. After the jump the lateral diameter changes with $\delta L$, and eq. (2.17) can also be expressed in terms of $\delta L$ instead of $\delta\theta$. During our experiments the starting contact angle $\theta_0$ is not equal to $\theta_d$. According to Oksuz and Ebril [29], who recently have commented on the work of Shanahan, $\delta\tilde{\theta}$ should be redefined for the first jump, taking $\theta_0$ as the equilibrium angle. Thus $\delta\tilde{\theta} = \theta_0 - \theta_d$ and the value for the lateral diameter $L$ is taken just before the jumps $L_d$. For the first jump we can write $\delta\tilde{G}$ as

$$\delta\tilde{G} = \frac{\gamma L_d(\theta_0 - \theta_d)^2}{4(2+\cos\theta_0)}. \qquad (2.18)$$

Assuming that the energy barrier $U$ remains constant during dissolution, Shanahan [28]

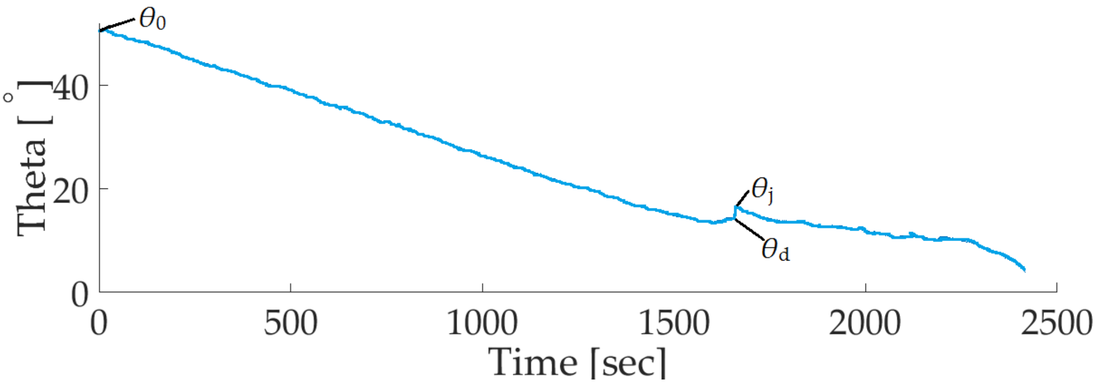

**Figure 2.4:** Experimental result for a 1-hexanol droplet dissolving on an etched silicon wafer surrounded by water in a closed glass container. The droplet dissolves in the stick-jump mode where the initial contact angle is $\theta_0$, the depinning contact angle is $\theta_d$ and $\theta_j$ is the value the contact angle reaches during the jump phase. With a camera we record the dissolution process and analyze these images to obtain the contact angle, lateral diameter and height of the droplet. Experimental set-up and the image analysis are described in chapter 5.

has shown that

$$\delta L \approx \left[ \frac{4LU}{\gamma \sin^2(\theta_0)(2+\cos(\theta_0))} \right]^{\frac{1}{2}}. \tag{2.19}$$

This enables us to compare small droplets with larger droplets. Since $\delta L \propto L^{\frac{1}{2}}$, we know that $\frac{\delta L}{L} \propto \frac{1}{(L)^{\frac{1}{2}}}$, thus the jumps in lateral diameter are relatively larger for smaller droplets, which makes it easier during experiments to observe the stick jump mode for small droplets [5].

# CHAPTER 3

# Lattice Boltzmann theory

## 3.1 Introduction

Simulation of fluid flows has been frequently used in the industry as an aid to design industrial products or constructions, e.g., cars, bridges, pumps, compressors, etc.. It also allows us to analyze parameters which are inaccessible to experiments and determines the impact of different physical phenomena on product performances. Depending on the scale of the problem at hand, we can use different simulation techniques. We depict these techniques in fig. 3.1 and discuss them in this section.

One way to model problems in the fluid dynamics domain is to solve the continuum transport equations such as the Navier-Stokes (N-S) equations, which can be derived by applying conservation of momentum, mass and energy for an infinitesimal volume. It is a requirement that these three quantities are conserved locally. When solving problems with the N-S equations, the complexity increases, because a coupled set of partial differential equations needs to be solved iteratively. This is done by use of finite difference or finite element methods. A domain is divided into elements or grids containing a huge number of particles, making it suitable for macroscopic problems. Solutions of the N-S equations can be regarded as a *top-down* approach, since the pressure, density, viscosity and velocity of the flow are directly analyzed. Also the N-S equations do not account for effects arising from molecular interactions [30], i.e. individual interactions are not resolved, but their ensemble average is resolved correctly.

For problems which require the effects of molecular interactions, other models have been implemented, where the transport equations have been obtained by modelling each molecule or atom individually. These models are thus suitable for simulating microscale problems. Within these models the particles collide with each other and the interparticle forces must be specified. In order to obtain the correct dynamics, the ordinary differential equations of Newton's second law must be solved. This is typically done in Molecular Dynamics (MD) simulations. This immediately leads us to the drawback of this approach. For rather "large" systems, a great number of molecules are involved. Thus the computation time is simply too large to obtain real-life timescales

[30]. The strength of the MD simulations lies in microscale systems where the Knudsen number is large.

Another way to solve the problems is using pseudo-particle approaches, which can be grouped into off-lattice and lattice based cellular automaton approaches. These methods pursue, unlike the N-S solvers, a *bottom-up* approach, i.e. the macroscopic quantities can be computed by averaging the interaction and density of the pseudo-particles locally [31]. The dissipative particle dynamics method is the most important off-lattice pseudo particle approach. It uses discrete fluid portions which can freely move in space at discrete time increments. This method can be derived from molecular dynamics by means of coarse-graining, i.e. the pseudo-particles do not represent single atoms or molecules, but rather clusters of atoms which carry the position and momentum of coarse-grained fluid elements. Using such pseudo-particles lead to a substantial gain in computational efficiency as compared to conventional molecular dynamics methods. However this happens at the expense of a loss in microscopic detail [31]. The pseudo-particles interact pairwise through a short-range interparticle potential and their dynamical behaviour, just like in MD, is realized by integration of the Newtonian equations of motions. Compared to MD simulations, with this approach longer timescales can be reached, due to the fact that the pairwise forces between the pseudo-particles are soft-repulsive. This method is used to simulate mesoscale problems in which both, hydrodynamic interactions and Brownian motion are important. Another off-lattice pseudo particle method is the direct simulation Monte Carlo method. In this method the state of the system is given by positions and velocities of a set of pseudo-particles. In this method the positions of these particles are updated without considering interparticle collisions at first. After this step a fixed number of particles are randomly selected for collisions. The particular strength of this method lies in the field of dilute gases [31].

The fictive particles in lattice gas automata can be regarded as coarse-grained groups of molecules of which the Newtonian mechanics are not explicitly taken into account. The fluid portions in lattice gas move at different speed and different directions on a fixed lattice and interact locally. Boolean lattice gas has the same unit mass and the same magnitude of the velocity vector. Motion of the particles consists of moving them from one lattice node to their neighbour in one unit of time according to their given unit momentum vector [31]. The main advantage of the lattice gas concept compared to classical N-S solvers consists of its excellent numerical stability under complex geometrical boundary conditions [31]. Due to the discrete treatment of the pseudo-particles and the discreteness of the collision rules, Boolean lattice gas automata violate the Galilean invariance and large fluctuations occur. To overcome these shortcomings, the lattice Boltzmann approach has evolved [31]. The main difference between the original lattice gas and the lattice Boltzmann method is that the former uses collision rules of the particles, while the latter uses relaxations rules and a collision operator [31].

The lattice Boltzmann modeling, which has been used in this thesis, originates from the theory developed for gases [30, 32], and lies in between the five previously mentioned methods. It does not model the continuum equations directly, but it also does not model individual molecules as it is the case in MD simulations. It models an ensemble of particles, which collide with each other, making it a mesoscale simulation method. It has the advantage of both the micro- and macroscopic approaches, with manageable computational sources. The conceptual difference with other methods, as we will see in the coming subsections, is that it uses discrete velocities [32]. It is a technique that can be used to simulate a wide range of fluid dynamics problems, e.g. boiling, capillary filling, coalescence of drops, drop impact, gas solid interaction, porous media, particle suspensions, moving contact lines, wetting on chemical heterogeneous surfaces, corrugated surfaces [30, 32]. It is also proven [33] that the Navier-Stokes equation can be derived from the lattice Boltzmann equation (eq. (3.4)).

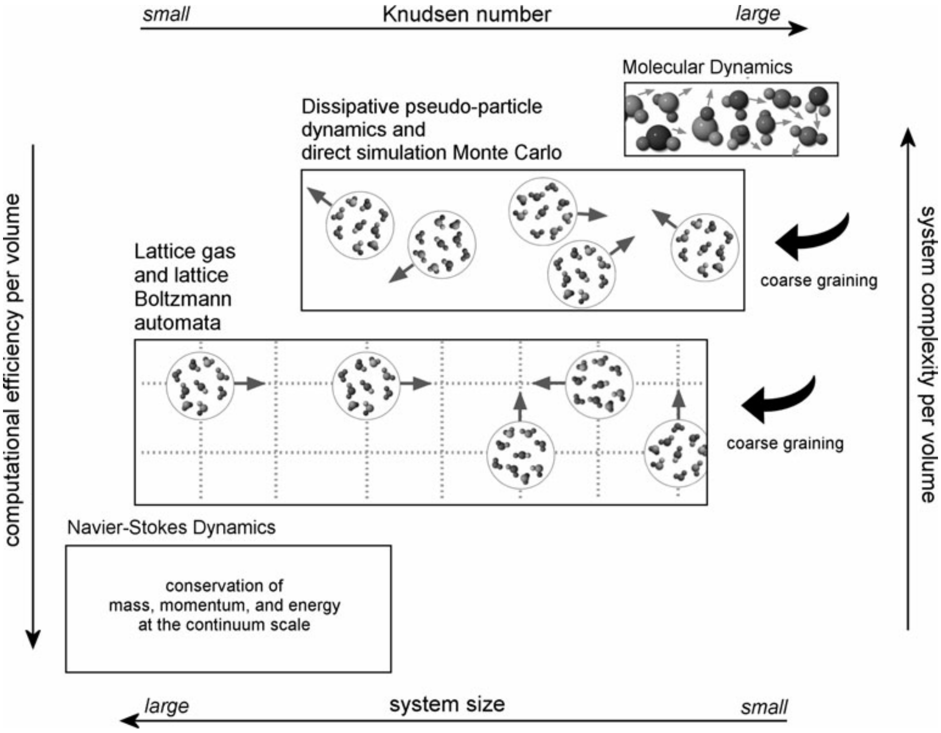

**Figure 3.1:** Various approaches, discussed in section 3.1 to computational fluid dyanmics with their preferred range of applicability. The methods have their repsective strength at different Knudsen numbers. Figure taken from Raabe [31].

## 3.2 Kinetic theory and the Boltzmann equation

Kinetic theory describes the behaviour of a dilute gas of hard spherical particles moving at high velocities ($\sim 300 m/s$). These particles travel in space and elastic collisions limit their interactions. Due to these collisions, particles have different velocities in different directions. If it is possible to know the position vector, $\mathbf{x}$, and momentum, $\mathbf{p}$, of each particle at some instant in time, then we are able to determine the exact dynamical state of the system. With the aid of classical mechanics we can predict all future states.

Since we have a large amount of particles a statistical mechanics approach is needed and appropriate, i.e. we need a particle distribution function, $f(\mathbf{x},\mathbf{v},t)$, in phase space to describe the system of particles [32]. The general form of the Boltzmann equation accounts for the streaming (left part of the equation) of the particles, whereas the right part of the equation accounts for the interparticle collisions [32, 34, 35]:

$$\frac{\partial f}{\partial t} + \mathbf{v} \cdot \nabla_x f + \mathbf{F} \cdot \nabla_p f = \Omega(f), \tag{3.1}$$

where $f$ denotes the particles' distribution function that represents the number density of particles with velocity $\mathbf{v}$ at location $\mathbf{x}$ at time $t_0$ , $\mathbf{F}$ is an external force on the particle that is small relative to the intermolecular forces and $\Omega$ is the collision integral that handles the collisions of the particle densities.

Bhatnagar, Gross and Krook (BGK) [36] have introduced the Single Relaxation Time collison operator (SRT) which describes the collisions as a relaxation towards the Maxwell-Boltzmann equilibrium distribution function $f^{eq}$. The characteristic time between collisions, $\tau$, is the rate at which the system relaxes towards the local equilibrium $f^{eq}$:

$$\Omega_{BGK} = -\frac{1}{\tau}(f - f^{eq}), \tag{3.2}$$

with

$$f^{eq} = n\left(\frac{m}{2\pi k_b T}\right)^{\mathrm{D}/2} e^{\left(-\frac{m(\mathbf{v}-\mathbf{u})^2}{2k_b T}\right)}, \tag{3.3}$$

where $n, u, T$ are the macroscopic number density, fluid velocity, and temperature. $m$ is the particle mass, D is the dimension of the space and in our case this is equal to three, and $k_b$ is the Boltzmann constant.

## 3.3 Lattice Boltzmann lattice

As has been mentioned briefly in section 3.1 the lattice Boltzmann method is a discrete method, i.e. it simplifies Boltzmann's original conceptual idea by reducing the number of possible spatial positions to a number of lattice nodes and by allowing only certain directions for momentum transfer (discrete velocities). The total lattice size is specified in terms of the number of lattice nodes in each spatial direction, e.g. $l_x$, $l_y$ and $l_z$. In this thesis our interest lies in the 3D behaviour of a droplet and we employ the well known D3Q19 lattice. This implies that we have a 3D lattice (depicted in fig. 3.2) where 19 discrete velocity directions are allowed, each pointing in direction $\mathbf{c}_i$ [37]:

$$\begin{bmatrix} 1 & -1 & 0 & 0 & 0 & 0 & 1 & 1 & 1 & 1 & -1 & -1 & -1 & -1 & 0 & 0 & 0 & 0 & 0 \\ 0 & 0 & 1 & -1 & 0 & 0 & 1 & -1 & 0 & 0 & 1 & -1 & 0 & 0 & 1 & 1 & -1 & -1 & 0 \\ 0 & 0 & 0 & 0 & 1 & -1 & 0 & 0 & 1 & -1 & 0 & 0 & 1 & -1 & 1 & -1 & 1 & -1 & 0 \end{bmatrix}$$

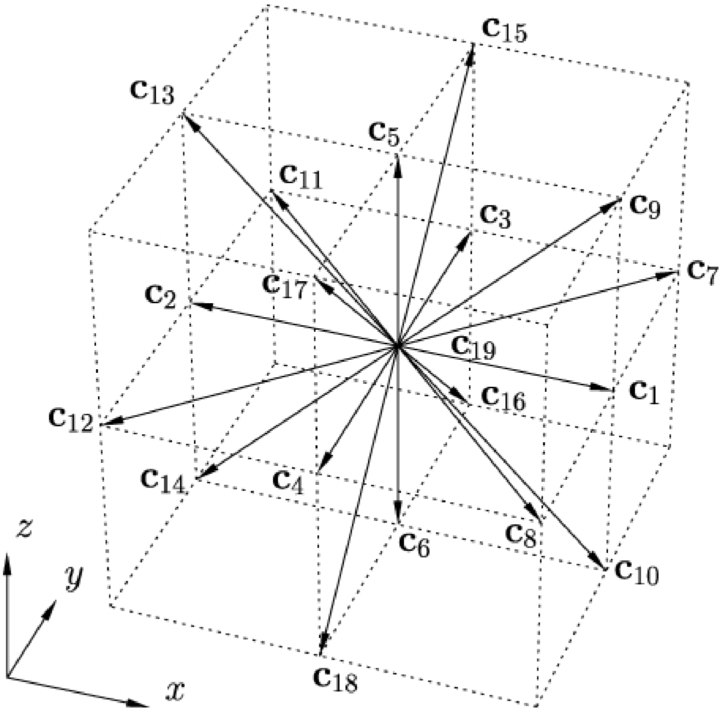

**Figure 3.2:** Geometry of the D3Q19 lattice with the discrete velocity directions $\mathbf{c_i}$. Figure taken from Hecht and Harting [37].

If we assume that no external force is acting on the particles, the discretized Boltzmann equation for the streaming of particles in a short amount of time $\Delta t$ is given by [16, 32, 38]

$$f_i{}^{\sigma}(\mathbf{x} + \mathbf{c}_i \Delta t, t + \Delta t) - f_i{}^{\sigma}(\mathbf{x}, t) = -\frac{\Delta t}{\tau^{\sigma}}[f_i{}^{\sigma}(\mathbf{x}, t) - f_i{}^{\sigma,eq}(\mathbf{x}, t)], \tag{3.4}$$

where $f_i$ is the distribution function for a specific direction $i$, and since we model a two fluid system, i.e. a multicomponent system, $\sigma$ refers to each specific component of the system (red fluid or blue fluid of the system), $\tau^{\sigma}$ is a relaxation time of component $\sigma$, which is related to the kinematic viscosity [35] as $\nu^{\sigma} = c_s{}^2(\tau^{\sigma} - \frac{1}{2})\Delta t$, where $c_s$ is the speed of sound. The speed of sound in the lattice is given by $c_s = \frac{1}{\sqrt{3}} \frac{\Delta x}{\Delta t}$.

If the distribution function $f_i{}^{\sigma}$ is known, we can calculate the macroscopic physical properties. The number density at a lattice site becomes

$$\rho_{\sigma} = \sum_{i=1}^{19} f_i{}^{\sigma}, \tag{3.5}$$

and the streaming velocity is calculated from

$$u_\sigma = \frac{1}{\rho_\sigma} \sum_{i=1}^{19} f_i{}^\sigma \mathbf{c}. \tag{3.6}$$

The equilibrium distribution function $f_i{}^{\sigma,eq}(\mathbf{x},t)$ is given by[16, 37]

$$f_i{}^{\sigma,eq}(\mathbf{x},t) = w_i \rho_\sigma \left[ 1 + \frac{\mathbf{c}_i \cdot \mathbf{u}^\sigma}{c_s{}^2} + \frac{(\mathbf{c}_i \cdot \mathbf{u}^\sigma)^2}{c_s{}^2} - \frac{\mathbf{u}^{\sigma 2}}{2 c_s{}^2} \right], \tag{3.7}$$

where $w_i$ is the weight that each velocity direction has,

$$w_i = \begin{cases} \frac{1}{18} & \text{for } i = 1..6 \\ \frac{1}{36} & \text{for } i = 7..18 \\ \frac{1}{3} & \text{for } i = 19 \end{cases} .$$

## 3.4 The Shan-Chen multicomponent model

Answering the main question of this thesis requires a multicomponent and single phase method to describe the behaviour of droplets on heterogeneous surfaces surrounded by another immiscible fluid. To reach this purpose we implement the Shan-Chen multicomponent model [39, 40]. This model introduces an interparticle potential that involves nearest neighbour interactions. This potential adds an attractive or repulsive tail to the local elastic collision. A distinct feature of this model is that it does not conserve momentum locally at each site, but summing over the net momenta at each site conserves the total momentum of the system. The Shan-Chen model sets the interaction force between the fluids through a phenomenological interaction parameter. The value of the interaction parameter between the two components, called $g_{\sigma\overline{\sigma}}$, determines to what extent the force between the two fluid species is attractive or repulsive; a positive value of $g_{\sigma\overline{\sigma}}$ mimics a repulsive force, i.e. it causes the fluids to be immiscible. The force due to the interparticle potential at each site $\mathbf{x}$ can be calculated from

$$\mathbf{F}_\sigma(\mathbf{x}) = -g_{\sigma\overline{\sigma}} \Phi_\sigma(\mathbf{x}) \sum_i \Phi_{\overline{\sigma}}(\mathbf{x} + \mathbf{c}_i)\mathbf{c}_i, \tag{3.8}$$

where $\Phi(\mathbf{x})$ can be regarded as the so-called effective mass, where we define $\Phi_\sigma(\mathbf{x}) = 1 - e^{\rho_\sigma}$ [41]. Moreover, the interaction parameter also determines the magnitude of the repulsive force between the two fluids and causes a surface tension between the droplet and the surrounding fluid [16, 41].

With the Shan-Chen model we can indirectly set the contact angle of the droplet sitting on a substrate. We then need an interaction parameter between each individual fluid and the wall. The interaction parameter between each of the fluid species and the wall, called $g_{\sigma w}$ and $g_{\overline{\sigma} w}$ respectively determines the strength of the adhesive force between the substrate and each of the fluids separately. This adhesive force is only present at the substrate, i.e. it is purely a local force between the fluids and the wall [16, 30]. To ensure this, a switch function $s$ has been included which is equal to 1 at a solid node and 0 elsewhere:

$$\mathbf{F}_{\sigma,w}(\mathbf{x}) = -g_{\sigma w}\Phi_\sigma(\mathbf{x})\sum_i s(\mathbf{x}+\mathbf{c}_i)\mathbf{c}_i. \tag{3.9}$$

Furthermore, the wall parameters has been chosen independent of $g_{\sigma\overline{\sigma}}$ and as has been reported by Huang et al. [16] a positive value of the wall parameter implies that we have a non-wetting fluid, whereas a negative value indicates a wetting fluid. Thus by simply tuning these three interaction parameters, this model allows to simulate droplets placed on hydrophylic, hydrophobic and even super hydrophobic surfaces.

## 3.5 Evaporation model

As has been mentioned in section 3.4, a positive value of the fluid-fluid interaction parameter $g_{\sigma\overline{\sigma}}$ creates a repulsive force between the two components (see eq. (3.8)). This results in phase separation of the two fluids, i.e. each component will separate into a denser phase (majority phase) and a lighter phase (minority phase), respectively. If we initialize a droplet surrounded by a large amount of another fluid (large system size), the droplet then separates into a majority phase, the droplet, and into the minority phase. In order for us to enhance this dissolution process of the droplet, we employ a evaporation model developed by Hessling et al. [1]. We first let the system equilibrate and then impose the density of component $\sigma$ at the boundary $x_H$ to a constant value $\rho_H^\sigma = m_{evp}$. If we study the density profile of the droplet's fluid, component $\sigma$ in the system as depicted in fig. 3.3, then we see that the density is first constant and that it decreases when passing through the interface and enters its minority phase (the majority phase of component $\overline{\sigma}$). As we can see the transition from the majority to the minority phase is not sharp, due to the fact that we have a diffuse interface model. In case of a shrinking droplet this specified density $m_{evp}$ at the evaporation (system) boundary should be smaller than the minority density of component $\sigma$. This density gradient drives the diffusion process in the system, i.e. component $\sigma$ is forced to diffuse from the denser phase to the evaporation boundary at $x_H$. At the evaporation boundary the amount of density of component $\sigma$ that is turned into another component $\overline{\sigma}$ is equal to the density specified at this boundary $m_{evp}$. To ensure total mass conservation in the system, the density of component $\overline{\sigma}$ at the evaporation boundary is set to

$$\rho_H^{\overline{\sigma}} = \rho^\sigma(\mathbf{x},t-1) + \rho^{\overline{\sigma}}(\mathbf{x},t-1) - \rho_H^\sigma. \tag{3.10}$$

In a fluid mixture the components diffuse into each other if their mean velocities are

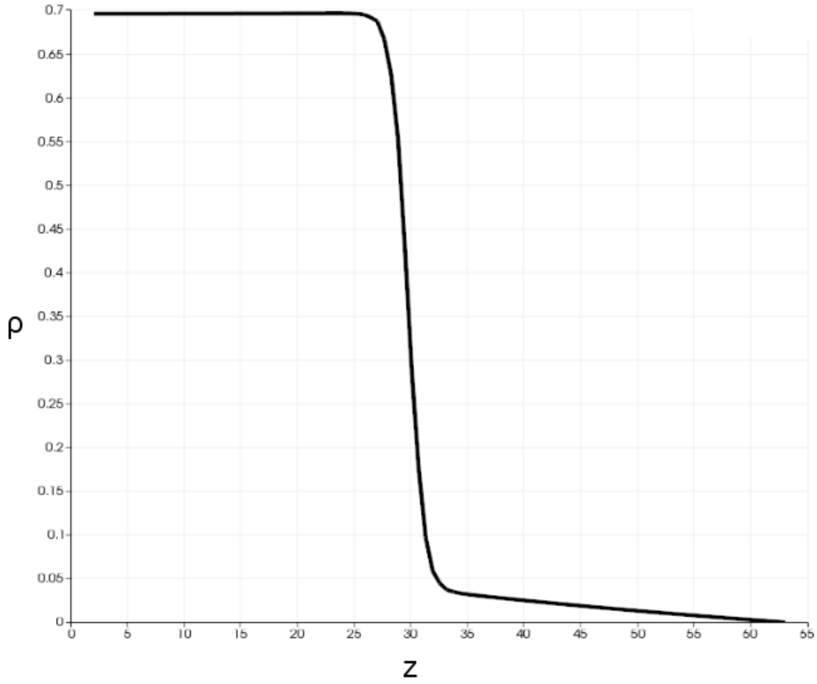

**Figure 3.3:** Sketch of density profile of component $c_1$ in the system, with a majority density of 0.7 and minority density of 0.04 and $m_{evp} = 0$. The substrate has a thickness of 2.

different [38]. The mass flux $j$ of component $\sigma$ in a binary system is given as [38]

$$\mathbf{j}^\sigma = \rho^\sigma(\mathbf{u}^\sigma - \mathbf{u}), \tag{3.11}$$

where $\mathbf{u}^\sigma - \mathbf{u}$ is the mass-averaged diffusion velocity of component $\sigma$ relative to fluid mixture velocity $\mathbf{u}$, i.e. it indicates the motion of component $\sigma$ relative to the local motion of the fluid mixture. Fick's first law describes the mass flux in a binary system as [38]

$$\mathbf{j}^\sigma = -D^{\sigma\sigma}\nabla\rho^\sigma - D^{\sigma\overline{\sigma}}\nabla\rho^{\overline{\sigma}}, \tag{3.12}$$

where $D^{\sigma\sigma}$ is the self-diffusivity term and $D^{\sigma\overline{\sigma}}$ is the cross-diffusivity contribution. Furthermore it is known that the diffusion in the lattice Boltzmann model is given as

$$D = {c_s}^2(\tau - \frac{1}{2}). \tag{3.13}$$

If the fluid-fluid interaction parameter is set to zero, then the diffusion constant can be written as

$$D = \frac{{c_s}^2(\tau - \frac{1}{2})}{\rho^{\sigma} + \rho^{\overline{\sigma}}}(\rho^{\overline{\sigma}} - \rho^{\sigma}). \tag{3.14}$$

## 3.6 Boundary conditions

Apart from the density that we specify at the boundaries in the evaporation model, we also impose other boundary conditions for the simulations. All the boundaries, except for the boundary where the substrate is positioned, are periodic. With periodic boundary conditions the boundaries are treated as if they are attached to their opposite boundary, i.e. they are realized by propagating the distribution function $f$ leaving the system's edge on to the boundary nodes located on the opposite edge of the system [32, 37]. At the boundary where the solid substrate is positioned in the system, we impose a no-slip mid-plane bounce back boundary condition.

## 3.7 Contact angle determination

As has been stated in section 3.4, we can simulate our desired contact angles by choosing the three parameters independently, but a fully analytic solution from which we can calculate the contact angle is not available yet. Huang et al. [16] have used the concept of cohesive and adhesive forces and Young's equation (2.1) to propose an estimate for determining the contact angle, based on equilibrium densities $\rho_\sigma$ and $\rho_{\overline{\sigma}}$:

$$\cos(\theta) = \frac{g_{\overline{\sigma}w} - g_{\sigma w}}{g_{\sigma\overline{\sigma}}\frac{\Phi_\sigma - \Phi_{\overline{\sigma}}}{2}}. \tag{3.15}$$

We define $\Delta x = \Delta t = m_0 = \rho_0 = 1$. To test Huang's model we have initialized a droplet (labeled as red fluid "r") with a density of $\rho_r = 0.7$ on a flat substrate surrounded by an immiscible fluid (labeled as blue fluid "b") with a density of $\rho_b = 0.7$, in a system where $l_x = l_y = l_z = 64$, $g_{br} = 0.1$.

After the system has equilibriated ($t = 6000$), we use the geometrical concept (fig. 2.2) to determine the contact angle from (2.3). Since the droplet has a spherical cap shape, we only need 3 points to determine its contact angle as depicted in fig. 3.4. The transition from the substrate to the droplet gives rise to an error for the contact angle measurement, therefore the height $H$ and the lateral diameter $L$ are measured $5\Delta x$ above the substrate.

From fig. 3.5 it is clear that we can simulate droplets on any type of surface and that the predicted value for the contact angle from Huang and the one measured from the simulation are in close agreement. Some error comes from the fact that we are dealing with a diffuse interface method, which makes it difficult to determine the exact points which we need for this simulation.

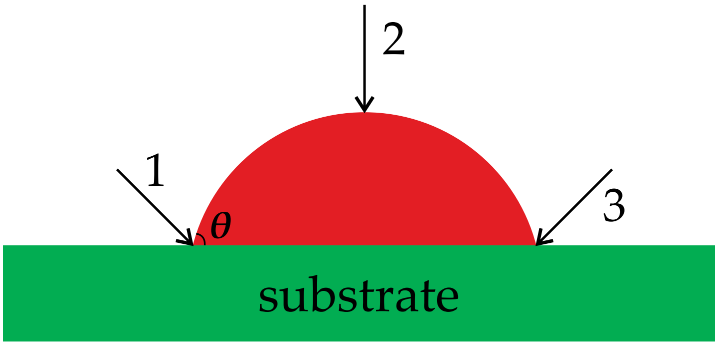

**Figure 3.4:** The three points of the droplet that are needed to determine its contact angle from the simulations.

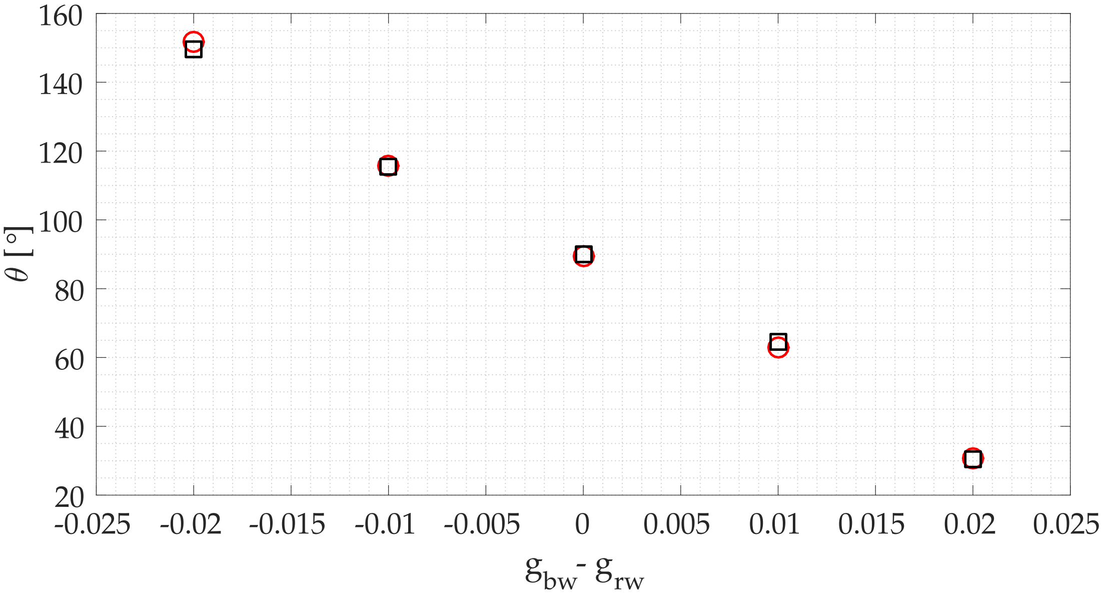

**Figure 3.5:** The contact angle measured from the simulations, marked with, ○, and the values predicted from Huang's model, marked with □, as a function of the difference between the fluid-wall interaction parameters.

.

# CHAPTER 4

## Numerical simulations of droplet dynamics

In this part of the thesis we study the contact line dynamics of dissolving sessile droplets numerically. For this purpose we employ the lattice Boltzmann method with an addition of the Shan-Chen multicomponent model and an evaporation model developed by Hessling et. al [1]. We first test the consistency of this evaporation model with a benchmark of a free spherical droplet surrounded by still liquid. From this benchmark we determine the diffusion constant $D$, which is an important parameter for us to compare our results with theory. We then carry on with simulations on dissolving sessile droplets. To closely model the pinning sites that droplets encounter on samples during experiments, we apply chemical patterning on our substrates for the simulations. We compare the results with the theory given in chapter 2. Furthermore we define $\Delta x = \Delta t = m_0 = \rho_0 = 1$ throughout this chapter.

### 4.1 A free spherical droplet in still liquid

To test the consistency of the model that has been described in 3.5, we simulate a free droplet at rest in the center of our system. This is a classical problem which has been reported in 1950 by Epstein and Plesset [2]. In their paper they calculate the lifetime of a spherical isolated bubble at rest with an initial radius $R_0$ in an infinitely extended liquid-gas solution in which the gas concentration far away from the bubble is $c_\infty$. Duncan and Needham [42] and Su and Needham [43] report and verify experimentally that the Epstein and Plesset theory is also applicable to droplets instead of bubbles, where the concentration field at the droplets interface is the saturation concentration $c_s$. Due to the concentration gradient in the system and given that the saturation concentration near the droplet's surface is higher than the concentration far from the droplet, the droplet shrinks through the diffusion process. For a shrinking droplet with radius $R$, the dynamics of its radius is given by [42]

$$\frac{dR}{dt} = \alpha \left( \frac{1}{R} + \frac{1}{\sqrt{\pi D t}} \right), \tag{4.1}$$

with

$$\alpha = \frac{Dc_s}{\rho}\left(\frac{c_\infty}{c_s} - 1\right). \tag{4.2}$$

This equation does not account for the interfacial tension $\gamma$ between two fluids. The interfacial tension defines the droplet's radius through the Laplace equation $\Delta P = \frac{2\gamma}{R}$, where $\Delta P$ is the increased pressure inside the droplet. Duncan and Needham [42] report that the lifetime of the droplet is not much affected if the interfacial tension is excluded, i.e. if the Laplace pressure is neglected and the droplet dissolves mainly due to the concentration gradient in the system. However, for the case where $c_\infty$ approaches the saturation concentration $c_s$, the actual lifetime of the droplet is much smaller than the lifetime calculated from eq. (4.1). In this case the concentration gradient is then relatively small, thus the driving force for dissolution is not the concentration gradient, but the pressure gradient, i.e. the interfacial tension becomes significant due to the Laplace pressure. Another consequence of the Laplace pressure is that it increases with a smaller radius of the droplets. Thus smaller droplets have a greater Laplace pressure and due to this a higher dissolution rate. In our simulations we choose the value of $c_\infty$ such that it is not close to the value of the saturation concentration, i.e. $m_{evp}$ is smaller than the value of the density in the minority phase $\rho^{minor}$.

We first simulate droplets in a $64^3$, a $128^3$ and a $256^3$ system, with an initial radius of $R_0 = 19.2$, $R_0 = 38.5$ and $R_0 = 77$, respectively. The distance to the evaporation boundary is not equal in all of the system sizes. The fluid interaction parameter, $g_{br}$ is equal to 0.10. Simulations are run for three different values of $m_{evp}$, namely: 0, 0.015 and 0.025. We depict the results in fig. 4.1. In order for us to test the consistency of the model and to extract the diffusion constant, which we need in order to discuss the results we obtain from simulations on dissolving sessile droplets, we fit our data to analytical solutions. We therefore solve eq. (4.1) numerically with the diffusion constant $D$ as a fitting parameter. Here $c_s = \rho^{minor}$, since this is the saturation concentration when crossing the interface of the droplet and $c_\infty$ is the density specified at the evaporation boundary, thus $c_\infty = m_{evp}$ and $\rho = \rho^{major}$. In fig. 4.2 we give the values for the diffusion constant obtained from the different simulations as a function of the system size. We assume that the droplet has an interface thickness of 5 and thus give error bars in fig. 4.2 for the diffusion constant $D$. We notice that the simulations of the $64^3$ system has a larger deviation from the fit and has larger error bars. The reason for this is the fact that the droplet is relatively small, which means that the droplet will mostly dissolve due to the Laplace pressure, i.e. surface tension becomes significant. We notice that the measured diffusion constant becomes smaller if we increase the system size, i.e. if we increase the distance of the droplet to the evaporation boundary. As has been discussed before, the Epstein-Plesset model assumes a droplet placed at the center of in infinite system, and thus if the droplet is farther from the boundary it better approximates the infinite system size assumption. Numerically it is difficult to simulate an infinite system, since this requires much more computing time. Thus the droplet dissolves much slower. From fig. 4.2 we can also conclude that we need to make the system size larger in order to reach convergence and to reasonably satisfy the infinite size from theory. To support this statement, we simulate a free spherical droplet at the center in a $128^3$ system with different radii, i.e. we study how the diffusion constant changes with the droplet's distance to the evaporation boundary. In fig. 4.3 we depict the diffusion constant as a function of the droplet's radius to illustrate that the diffusion constant becomes larger, if the droplet is closer to the evaporation boundary. This plot nicely shows that indeed we need a larger system to reach convergence, i.e. we get closer to the expected value of 0.12 (obtained from eq. (3.13)) for the actual diffusivity. From fig. 4.2 it is clear that the diffusion constant is not much affected for different values of $m_{evp}$. This is indeed what is expected from the theory. From fig. 4.1 it is also clear that if the droplet becomes small, it dissolves faster, due to the Laplace pressure. These results confirm that the evaporation model nicely describes the dynamics of the droplet and we now show through numerical simulations that the Epstein-Plesset theory is indeed valid for a free spherical droplet at the system's center in still liquid.

We also study the influence for different $g_{br}$ values on the equilibrated radius, $R_{eq}$ of the droplet and the diffusion constant in a $128^3$ system with an initial radius $R_0$ of 38.5. For values smaller than 0.10 for $g_{br}$ we expect a smaller droplet, since the Shan-Chen force between the two fluids is smaller and for higher values we expect the other way around. In table 4.1 we give the radius for different $g_{br}$ values after equilibration. From these results it is clear that for increasing $g_{br}$ value, the equilibrated radius also increases. As has been discussed before this is expected, since the repulsive Shan-Chen force increases. Due to this, we indeed see that the minority density decreases, with increasing value of the fluid-fluid interaction parameter, i.e. each of the components have been less separated into the lighter phase. It is also clear that for $g_{br} = 0.1$ the equilibrated radius is close to the initial radius of 38.5. We have set the evaporation density, $m_{evp}$, equal to 0.015. The diffusion constants have been calculated in the same way as has been described before. However, in case of $g_{br} = 0.09$, we had to cut off around $20 \sim 25\%$ of the data, due to the fact that the distance from the droplet's interface to the evaporation boundary is relatively larger and thus more time is needed to develop the density gradient in the system. Moreover the density in the minority phase is also relatively large compared to $g_{br} = 0.10$, thus the droplet shrinks much faster. From table 4.1 we can infer that the diffusion constant becomes larger if the fluid-fluid interaction parameter increases. This is counter-intuitive as one would expect that the diffusion constant becomes smaller if the repulsive force between the two species has increased. The reason for this is the fact that the surface tension between the droplet and the other fluid increases, if the fluid-fluid interaction parameter becomes larger. For $g_{br} < 0.10$, the droplets are relatively small, thus the Laplace pressure becomes significant, i.e. the diffusion process is mostly pressure driven. For $g_{br} > 0.10$, the surface tension becomes higher, and thus might be more significant to include in the equations than for $g_{br} = 0.10$.

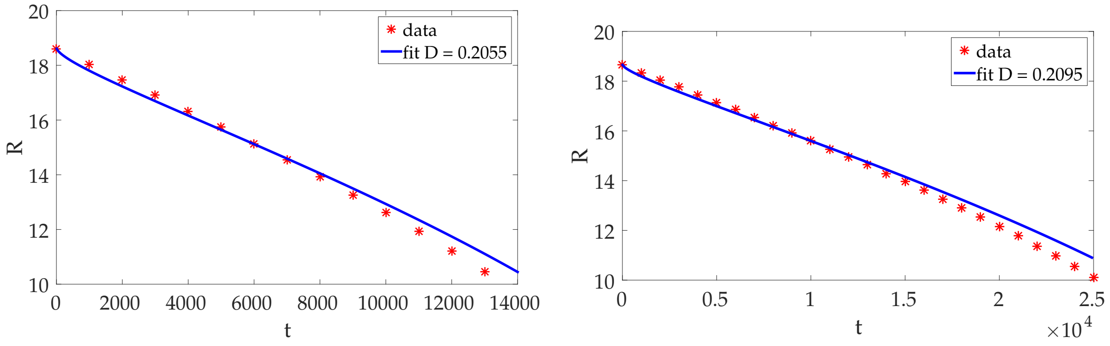

**(a)** $64^3, m_{evp} = 0.015$ **(b)** $64^3, m_{evp} = 0.025$

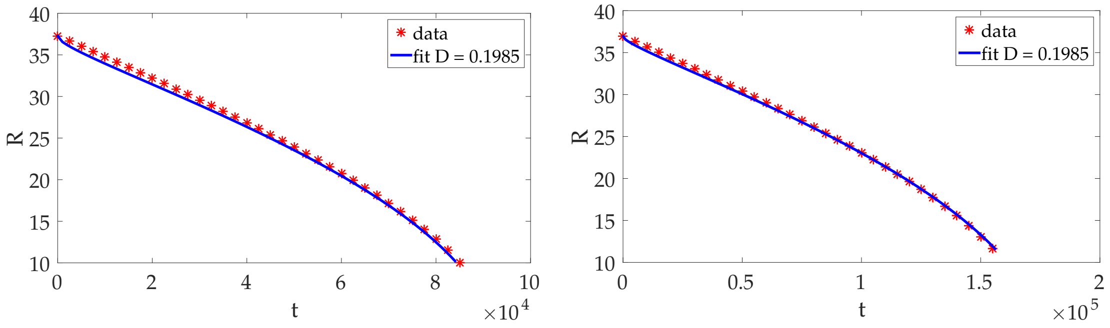

**(c)** $128^3, m_{evp} = 0.015$ **(d)** $128^3, m_{evp} = 0.025$

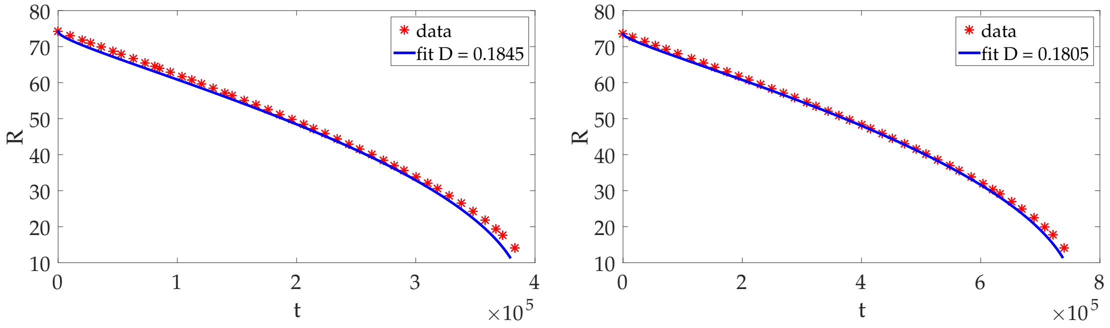

**(e)** $256^3, m_{evp} = 0.015$ **(f)** $256^3, m_{evp} = 0.025$

**Figure 4.1:** Numerical results of the Epstein-Plesset test, for three different system sizes and two different values for $m_{evp}$. From these results it is clear that the Epstein-Plesset theory can be extended to droplets surrounded by another liquid. Duncan and Needham [42] and Su and Needham [43] already confirmed this with their experimental work. We fit the data to solution of eq. (4.1) to find the diffusion constant. In the $64^3$ system the data has a larger deviation from the fit, because the droplet is very small, thus less fluid in the system and the droplet dissolution due to the Laplace pressure becomes significant.

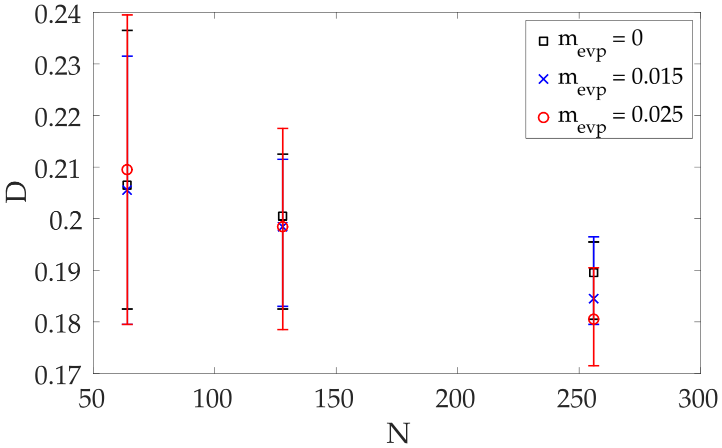

**Figure 4.2:** Diffusion constant obtained from shrinking droplet simulations in different system sizes: $64^3$, $128^3$ and $256^3$ and for three different values for the density set at the evaporation boundary: 0, 0.015 and 0.025. The initial radius of the droplet in the three different systems is $R_0 = 19.2$, $R_0 = 38.5$ and $R_0 = 77$, respectively. We learn from this figure that the error bars and the diffusion constant becomes smaller if we increase the system size.

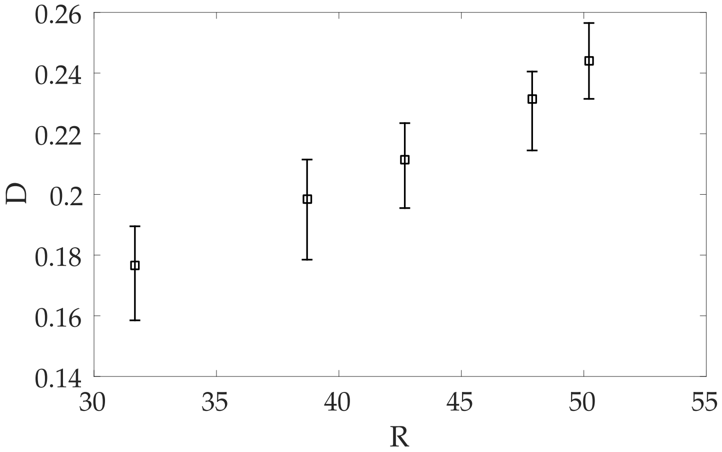

**Figure 4.3:** Diffusion constants obtained for freely floating droplets with different radii in a $128^3$ system and $m_{evp} = 0.015$. It is clear from this figure that in order to reach convergence, we must make the distance to the evaporation boundary larger, since the diffusivity becomes smaller if the distance to the evaporation boundary becomes larger.

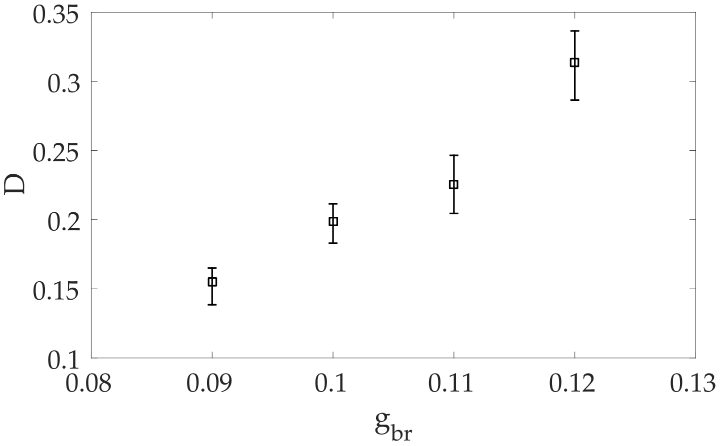

**Figure 4.4:** The results for a freely floating droplet in a $128^3$ system for different values of the fluid interaction parameter $g_{br}$. We have fitted the data to eq. (4.1) to find $\alpha$ which gave us diffusion constant through eq. (4.2).

**Table 4.1:** Results for different values of the fluid interaction parameter $g_{br}$. It it clear that the droplet radius increases as a function of $g_{br}$, because the Shan-Chen repulsive force between the fluids becomes larger and thus the major density increases and the minor density decreases.

| $g_{br}$ | $R_{eq}$ | $c_s$ | $\rho$ |
|---|---|---|---|
| 0.09 | 35.39 | 0.061 | 0.697 |
| 0.10 | 38.79 | 0.037 | 0.719 |
| 0.11 | 40.32 | 0.024 | 0.734 |
| 0.12 | 41.17 | 0.016 | 0.743 |

## 4.2 Different dissolution modes

### 4.2.1 Constant Contact Angle mode

As has been mentioned in chapter 1, it is experimentally difficult to achieve droplets dissolving solely in the CA mode due to pinning sites on the substrate. Numerically we can deposit droplets on completely flat surfaces, i.e. surfaces that do not have any patterning or roughness of any kind. As has been described in sections 3.4 and 3.7, we can achieve droplets with different contact angles on these flat surfaces with a set of fluid-fluid interaction parameters, $g_{br}$, and fluid-wall interaction parameters, $g_{rw}$ and $g_{bw}$.

To initialize a simulation with a droplet of the same volume, but different contact angles $\theta$, we need to determine the droplet's radius of curvature $R$ [44] from which we can determine the lateral diameter $L$ and height of the droplet $H$ (see fig. 2.2):

$$R = \left[\frac{V_{droplet}}{\frac{\pi}{3}(2 - 3\cos\theta + (\cos\theta)^3)}\right]^{\frac{1}{3}}. \tag{4.3}$$

$$H = R(1 - \cos\theta), \tag{4.4a}$$

$$L = 2R\sin\theta. \tag{4.4b}$$

The system size for these runs is 256 × 256 × 128 and the droplet has a volume equal to $4 \times 10^5$. The following combination of parameters resulted in different contact angles see table 4.2).

**Table 4.2:** The equilibrium contact angles achieved for different combinations of the interaction parameters $g_{br}, g_{bw}$ and $g_{rw}$.

| $g_{br}$ | $g_{bw}$ | $g_{rw}$ | $\theta$ [°] |
|---|---|---|---|
| 0.10 | 0.01 | -0.01 | 22 ± 4 |
| 0.10 | 0.005 | -0.005 | 62 ± 2 |
| 0.10 | -0.005 | 0.005 | 115 ± 2 |

We calculate the contact angle by determining the three points illustrated in fig. 3.4 from the simulations. Using eqs. (4.4a) and (4.4b), we then determine the contact angle. Assuming an interface thickness of 5, we determine the error for the measured contact angle. As can be seen from table 4.2, the largest error is obtained for a droplet with a contact angle of 22°. In this case the droplet has spread out to such an extent that it is close to the boundary of the system. Some error is also caused by low resolution, because in case of a contact angle of 22°, the droplet is flat at its rim, and thus it resembles a thin film of fluid.

For the CA mode simulations, we set the density at the evaporation boundary equal to 0.015 and 0.025. The results for three different contact angles, 22°, 62° and 115° are depicted in fig. 4.5 respectively. From these figures it is clear that the contact angle is not entirely constant during the entire simulation, i.e. it changes with ∼2°. This occurs due to the the fact that during the diffusion process the density in the system changes. Since the change is very small and within the range of the error obtained from measuring the contact angle, we consider the contact angle to be constant. It is also clear from fig. 4.5 that in case of 62° and 115° the contact angle becomes smaller at the end of the simulation. The reason for this is that there is not enough fluid left in the system, and thus the droplet starts dissolving on its own. However, if the contact angle is 22°, we learn from fig. 4.5 that the contact angle becomes larger in the end. Since we have a small amount of fluid left in the system, the droplet becomes very flat and thus the error in measuring the contact angle increases. We can fit the results of the lateral diameter to an analytical solution for dissolving droplets in the constant contact angle mode. We see that the lateral diameter deviates from the fit at the end of the dissolution. We ascribe this also due to the fact that the droplet becomes so small that the dissolution process is pressure driven. From [7] it is known that the lateral diameter $L$ shrinks during the dissolution process in the CA mode as follows:

$$L^2(t) = {L_0}^2 - \frac{8Dc_s\zeta}{\rho}\frac{f(\theta)}{3g(\theta)}t, \tag{4.5}$$

where $L_0$ is the initial lateral diameter of the droplet, $\zeta$ the undersaturation defined in eq. (2.9), and $f(\theta)$ and $g(\theta)$ are defined in eqs. (2.6) and (2.7), respectively. We can fit the data to the analytical function

$$L^2(t) = {L_0}^2 - \kappa(\theta)t, \tag{4.6}$$

and can then extract the fitting constant $\kappa(\theta)$ from the fit. As we can see this fitting constant depends on the contact angle $\theta$ of the droplet. Using this fitting constant $\kappa(\theta)$, we can determine the diffusion constant as

$$D = \frac{\rho\kappa(\theta)3g(\theta)}{8c_s\zeta f(\theta)}. \tag{4.7}$$

Taking transient effects into account, we cut off 10% of the dissolving droplet data, i.e. when the evaporation density is specified at the system's boundary a gradient needs to develop in the system. The density and the saturation concentration have been determined by measuring the major and minor density in the system. These are measured $5\Delta x$ above the substrate, because the fluid-wall interaction parameter affects the density near the wall. After these parameters have been determined, we are able to find diffusion constants for the runs with eq. (4.7). The results for the diffusion constants are given in fig. 4.6. We also compute the error for the diffusion constant. Compared to the results obtained for the freely floating droplets in a $256^3$ system, the diffusion constants for the CA mode deviate $10 \sim 15\%$ from the values we found for the diffusion constant if $g_{br} = 0.10$. Some deviation is caused by the difference in density gradient in each direction. In case of the freely floating droplet the density gradient is homogeneous. We notice that the diffusion constant obtained from the simulations where $m_{evp} = 0.025$ are smaller than the ones obtained for $m_{evp} = 0.015$. The reason for this is the fact that the density gradient in the former is smaller, and thus closely approximates the theoretical model of an infinite system. The theoretical model assumes that the boundary is far away from the droplet, thus a small concentration gradient. The measured diffusion constant for all three different contact angles and $m_{evp} = 0.015$ and $m_{evp} = 0.025$, are all within the range of the error bars, where the droplet with a contact angle of 22° has the largest error, because it is flat. With the measured diffusion constants, we are able to compare the lifetime of the droplet depicted from theory with our results from the simulations. We determine $\tilde{\tau}_{CA}$ from the simulations by rescaling the droplet lifetime $t_{life}$ with eq. (2.10). Therefore we measure the initial volume $V_0$ of the droplet from the simulation, the major and minor density, we determine the time step at which the droplet has completely dissolved ($t_{life}$) and the measured diffusivity. Using eq. (2.12) we determine the theoretical value of $\tilde{\tau}_{CA}$ and compare it with the simulation results as depicted in fig. 4.7. It should be noted that we have measured the diffusivity with an equivalent equation to fig. 4.7. We learn from fig. 4.7 that depending on the contact angle of the droplet, the lifetime increases and then decreases again. Furthermore the simulation data closely follows the theoretical prediction, and as is clear from the figure the deviation from the theory is $< 8\%$. The error is smaller if $m_{evp} = 0.025$. The reason for this might be the same as discussed before. Because the density gradient is smaller, it better approximates the theoretical assumptions.

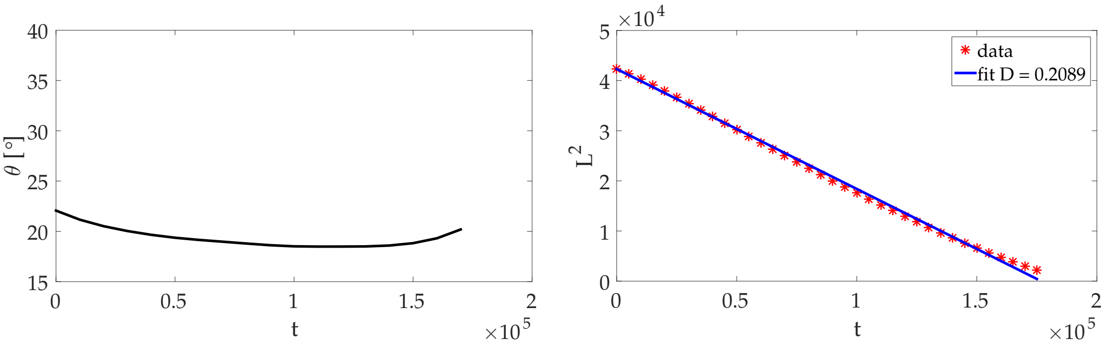

**(a)** Contact angle 22°

**(b)** Lateral diameter 22°

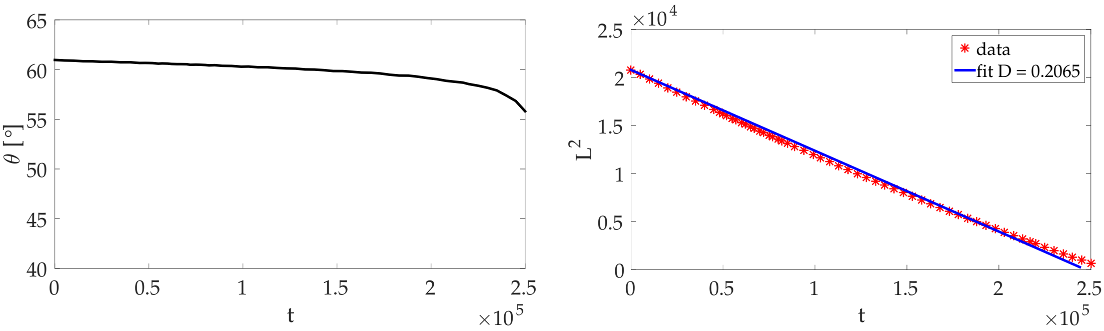

**(c)** Contact angle 62°

**(d)** Lateral diameter 62°

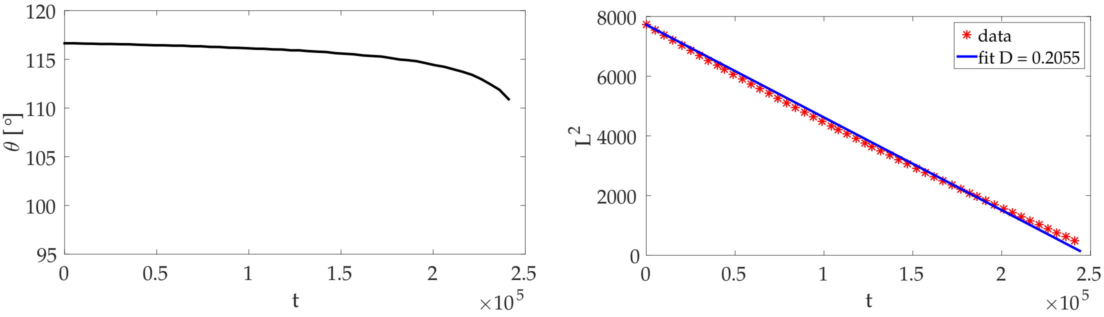

**(e)** Contact angle 115°

**(f)** Lateral diameter 115°

**Figure 4.5:** Results for the contact angle $\theta$ and lateral diameter $L$ of droplets dissolving in the CA mode with a contact angle of 22°, 62° and 115°. The initial volume of the droplet is $4 \times 10^5$ and $m_{evp} = 0.015$. Using eq. (4.7) we can determine the diffusion constant $D$ by fitting the lateral diameter data to eq. (4.6).

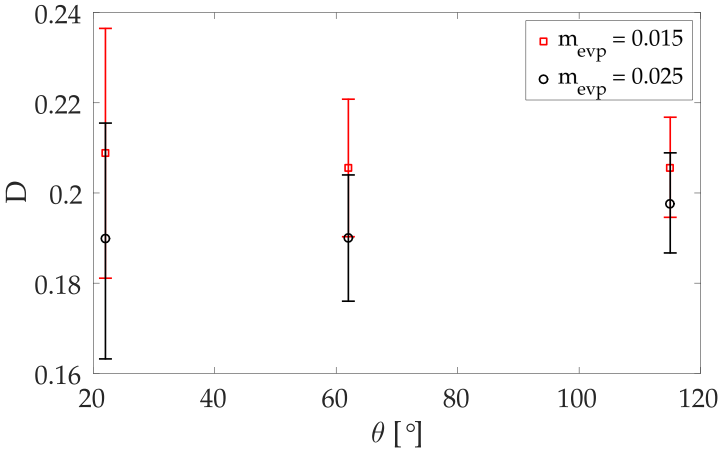

**Figure 4.6:** Results for the diffusion constant from the CA mode simulations where the initial volume of the droplet $V_0 = 4 \times 10^5$. The results are within the same error bars range. The diffusivity for $m_{evp} = 0.025$ is smaller, because the process is slower and thus might better approximates the theoretical assumptions for an infinite system.

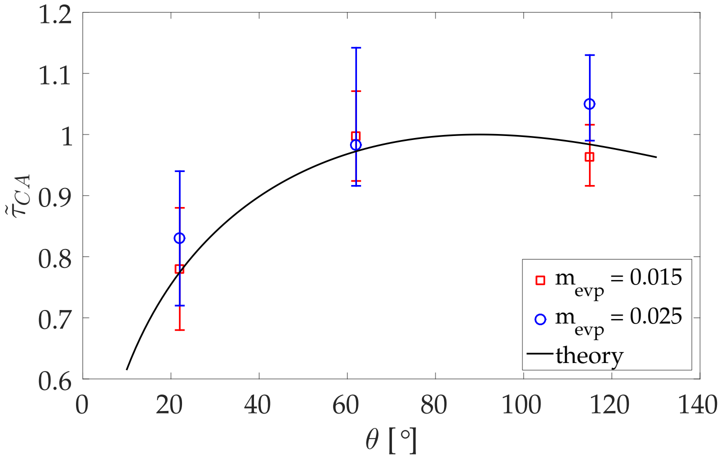

**Figure 4.7:** The rescaled lifetime of the droplet $\tilde{\tau}_{CA}$ has been calculated from simulation data: initial volume of the droplet, major and minor density, measured diffusivity and the lifetime of the droplet. The theoretical curve is drawn with eq. (2.12). The simulation data nicely follows the theoretical prediction.

### 4.2.2 Constant Radius mode

A droplet dissolving solely in the constant radius (CR) mode is, just like droplets dissolving in the CA mode, also difficult to observe in practice. At some point the droplet depins and starts dissolving in the CA mode in what resembles stick-slide behaviour. This depinning effect of the droplet can be explained by the free energy of the droplet. Assuming Young's equation (eq. (2.1)), i.e. equilibrium, the free energy $G$

of a droplet is given by [28, 29]

$$G = \gamma\pi\frac{L^2}{4}\left[\frac{2}{1+\cos\theta} - \cos\theta_Y\right], \tag{4.8}$$

where $\gamma$ is the surface tension, $\theta$ is the apparent contact angle of the droplet and $\theta_Y$ is the Young's (equilibrium) angle of the droplet on a surface. A system minimizes its free energy. Due to this, a droplet with a certain volume $V$ favours a certain lateral diameter $L_f$ with its equilibrium contact angle on a specific surface.

The free energy of a sessile droplet on a hydrophilic surface is less than the free energy of the same sessile droplet on a hydrophobic surface, thus the droplet sits on the hydrophilic surface. Therefore we initialize our system as follows: a droplet with a certain volume $V$ has been deposited on a hydrophilic disk with diameter $L_{disk}$. The disk is part of a hydrophobic surface, i.e. we have patterned the substrate with a hydrophilic disk and a hydrophobic part. We study two types of systems: system A has a hydrophilic disk with a contact angle of 30° and the hydrophobic part of the surface has a contact angle of 115°. System B has a hydrophilic disk with a contact angle of 60° and the hydrophobic part of the surface also has a contact angle of 115°. As already has been mentioned the droplet prefers to sit on this hydrophilic disk with its equilibrium contact angle. But since its volume is chosen such that $L_f > L_{disk}$, it does not reach this equilibrium contact angle. This causes the droplet to pin on this disk with an apparent contact angle $\theta$. This apparent contact angle is higher than its equilibrium contact angle on the hydrophilic disk $\theta_{Y,philic}$ and smaller than its equilibrium contact angle on the hydrophobic part of the surface $\theta_{Y,phobic}$. If we let the droplet dissolve in the system, its volume decreases. It minimizes its free energy by decreasing the apparent contact angle. At some point the apparent contact angle is equal to the equilibrium contact angle. From eq. (4.8) it follows that if the apparent angle reaches the value of the equilibrium contact angle, the droplet can reduce its free energy by decreasing its lateral diameter, thus the droplet depins and starts dissolving in the CA mode, i.e. it is energetically more favourable for the droplet to dissolve in the CA mode than to stay pinned. It is important for the simulations to choose the droplet's volume wisely, such that $L_f > L_{disk}$, in order for the droplet to dissolve in CR mode.

Apart from the two different systems A and B, we also vary the hydrophilic disk diameter, $L_{disk} = 96, 112, 130$ and 210 and the droplet's initial volume $V_0$. Also for these simulations, we use a $256 \times 256 \times 128$ system. The results for the contact angle $\theta$, lateral diameter $L$ and height $H$ as a function of time are depicted in fig. 4.8 for both systems A and B. The disk diameter is equal to 96 and the initial volume is $V_0 = \frac{2}{3}\pi(48)^3$. From these plots it is clear that the droplet does not solely dissolve in the CR mode. This is expected, because as can be seen from these plots, the droplet reaches its corresponding equilibrium contact angle and starts dissolving in the CA mode, thus minimizing its free energy. This phenomenon, where the droplet's dynamics switches from one mode to the other, has also been reported by Bao et al. [45] for growing droplets. They study the growth of femtoliter droplets through solvent exchange. These droplets nucleate on chemically patterned substrates and start growing in the CA mode until they get pinned. At this moment the growing mode of the droplet changes to the CR mode. This is indeed what we observe for all of the CR mode simulations on shrinking droplets. We are limited here by system size to let the droplet dissolve entirely or for longer time in the CR mode. From figs. 4.8(e) and 4.8(f) it is clear that the height of the droplet decreases faster in the CR mode than in the CA mode. This indicates that droplets dissolves faster in the CR mode. To illustrate this, we give the normalized volume as a function of time for dissolving sessile droplets both in system A and system B on a hydrophilic disk with diameter $L_d = 112$ and three different initial volumes $V_0$ in fig. 4.9. As has been discussed already, the droplet stays longer pinned in system A than in system B due to the smaller equilibrium contact angle in system A. Thus from fig. 4.9 it is clear that droplet dissolves faster in the CR mode, i.e. the volume of the droplet decreases relatively slower in the CA mode than in the CR mode. This explains why the height of the droplet changes faster in the CR mode than in the CA mode. We determine with eqs. (4.3) and (4.4b) the apparent initial contact angle $\theta_0$. We depict the results in fig. 4.10(a) where we give the droplet's apparent initial contact angle $\theta_0$ as a function of their initial volume $V_0$ on disks with varying diameters. As expected, increasing the droplet's initial volume $V_0$ on a disk with the same diameter $L_d$, leads to higher initial contact angles. Stauber et al. [3] report that identical droplets dissolve faster in the CR mode than in the CA mode if $\theta_0 < 148°$. From figure fig. 4.10(a) it is clear that our initial contact angles meet this criterion, thus our results in fig. 4.9 are consistent. Moreover from this figure it is also clear that the dissolution rate of the droplet is enhanced for smaller initial contact angles on the disk. In fig. 4.10(b) we depict the change in the droplet's interfacial energy with respect to their initial volume $V_0$ on a particular disk. If we compare the initial free energy of the droplet with the free energy at the moment of depinning from the disk, than we infer from fig. 4.10(b) that the difference in free energy $\frac{\Delta G}{\gamma}$ becomes larger if we increase the droplet's initial volume on a disk of same diameter. This is expected, because the depinning angle and the disk diameter are constant, but the droplet's initial contact angle is different.

The results for the decreasing contact angle in time has been compared to the analytical equation (see eq. (2.13)). We solve this differential equation numerically, where the diffusion constant has been used as a fitting parameter to the numerical data. In table 4.3 we list the obtained values for the diffusion constant $D$. It is clear from these results, that the diffusion constant becomes larger, if we increase the volume of the droplet on a disk with the same diameter. The reason for this is, as discussed before, that the distance of the droplet's interface to the evaporation boundary decreases. This is consistent with our findings in section 4.1, where we explicitly show with fig. 4.3 that the diffusion constant becomes larger if the droplet is closer to the evaporation boundary.

Using eq. (2.14), we theoretically predict $\tilde{\tau}_{CR}$ with the initial and depinning contact angle. We determine the time of depinning of the droplet $t_d$ from the simulations. Assuming an interface thickness of 5, the moment of depinning is determined when the lateral diameter of the droplet $L = L_d - 10$. We then rescale $t_d$ with eq. (2.10). In order to do this we use the diffusion constants determined from the fits of the CR mode results, the initial volume of the droplet and the major and minor density. We depict the results for system A in fig. 4.11(a) and for system B in fig. 4.11(b). Again from these two figures it is clear that the droplet stays longer pinned on a disk in system A than in B. Our results are comparable with the predicted values from the theory, but also here it should be noted that the diffusivity is measured from an equivalent equation to eq. (2.14). The theoretical curve in figs. 4.11(a) and 4.11(b) is drawn by measuring the initial and depinning contact angle from the simulation. We determine $\tilde{\tau}_{CR}$ with a constant lateral diameter, but as we learn from figs. 4.8(c) and 4.8(d) it is not entirely constant. We can also learn from figs. 4.11(a) and 4.11(b) that equally sized droplets dissolve longer in the CR mode on a disk with a smaller diameter, due to its larger initial contact angle $\theta_0$. Moreover droplets with different volume, but deposited on the same disk, dissolve longer in the CR mode if the droplet's volume is larger compared to the others.

After the droplet has depinned, it dissolves further in the CA mode. Since this resembles the stick-slide behaviour, we determine from eq. (2.15) $\tilde{\tau}_{stick-slide}$ theoretically. We then rescale the total lifetime $t_{life}$ of the droplet from the simulations with eq. (2.10). We follow the same route for this as we did for $\tilde{\tau}_{CR}$. The results for system A are depicted in fig. 4.11(c) and fig. 4.11(d). As we can see the results in system B deviate more from theory than the results from system A. An explanation for this is that the diffusion constant obtained from the CR mode is different when the droplet dissolves in the CA mode. If the droplet dissolves in the CA mode, the distance to the evaporation boundary changes and thus measured diffusivity becomes smaller. This explains that the results in system A are more comparable to the theory than in system B, i.e. the droplet dissolve longer in the CR mode in system A than in system B. This also explains, why $\tilde{\tau}_{stick-slide}$ for the large droplet which is very close to the boundary, deviates from the theoretical curve in system A. If we compare the results of system B to system A, then we infer that the droplet has a longer lifetime in system B. As already discussed, and as supported by the work of Stauber et al. [3], identical droplets dissolve slower in the CA mode than in the CR mode. Since the droplet in system B depins earlier than an identical droplet in system A, it dissolves longer in the CA mode and therefore has a longer lifetime.

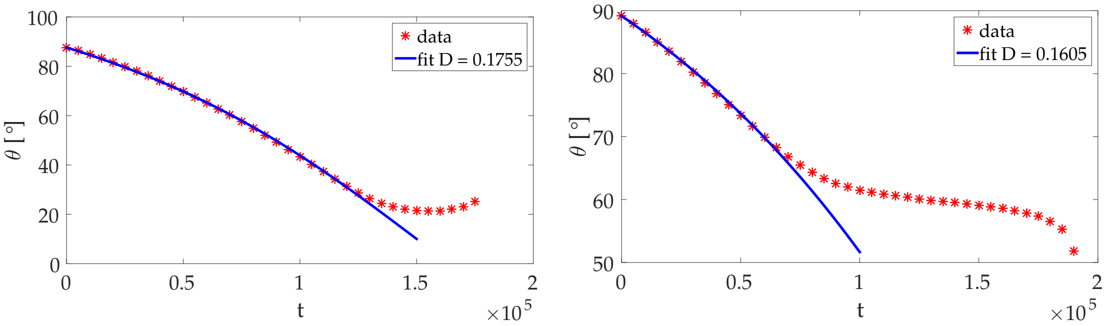

**(a)** Contact angle system A

**(b)** Contact angle system B

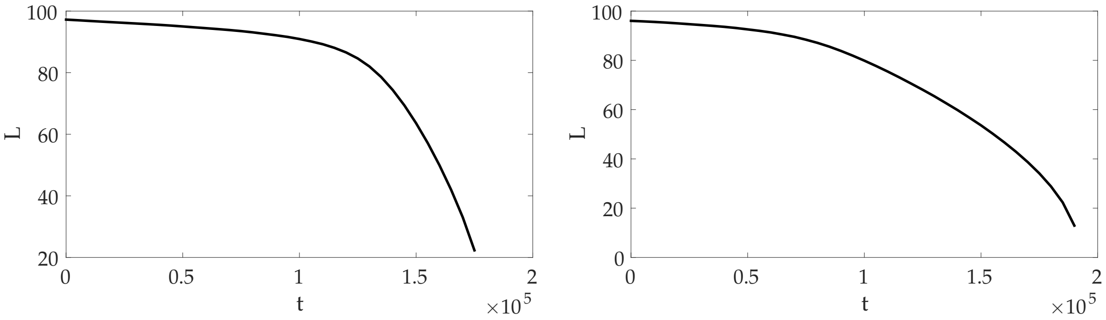

**(c)** Lateral diameter system A

**(d)** Lateral diameter system B

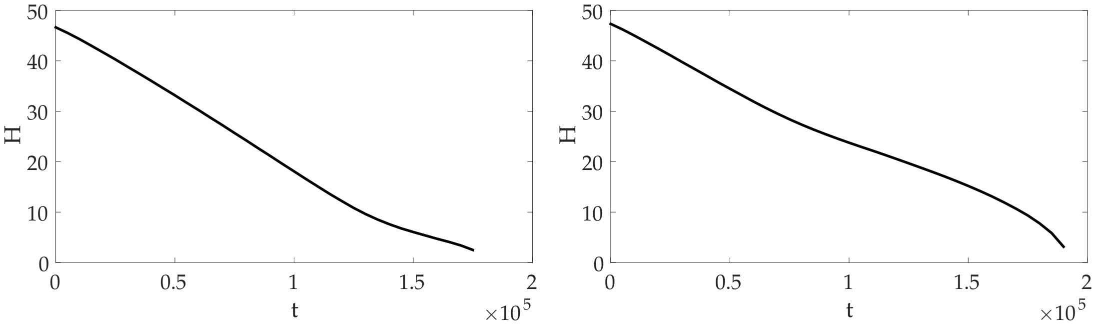

**(e)** Height system A

**(f)** Height system B

**Figure 4.8:** CR mode simulations of droplets in system A and B on a hydrophilic disk with diameter $L_d = 96$, volume $V_0 = \frac{2}{3}\pi(48)^3$ and $m_{evp} = 0.015$. We give the change in contact angle $\theta$, the lateral diameter $L$ and height $H$ of the droplet in time. Fitting the data of the contact angle to eq. (2.14) gives us the diffusion constant $D$.

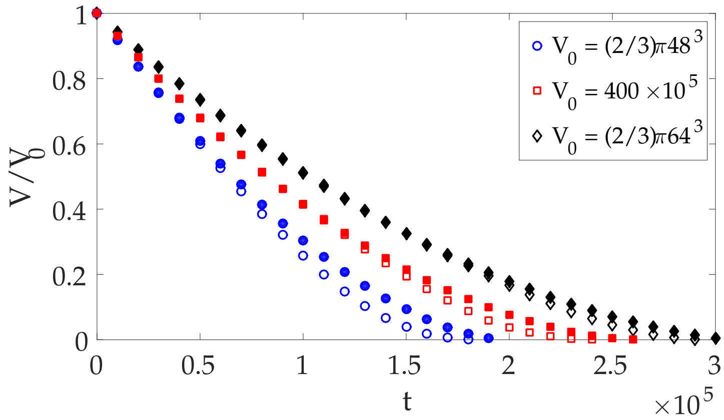

**Figure 4.9:** Normalized volume as a function of time for sessile droplets dissolving on a disk wit diameter $L_d = 112$. The results correspond to three different initial volumes. Open symbols correspond to sessile droplets in system A and closed symbols correspond to system B. Since the droplet depins at an earlier time in system B than in system A, we learn that the droplet dissolves faster in the CR mode than in the CA mode. Furthermore, the dissolution rate is enhanced for droplets with a smaller contact angle.

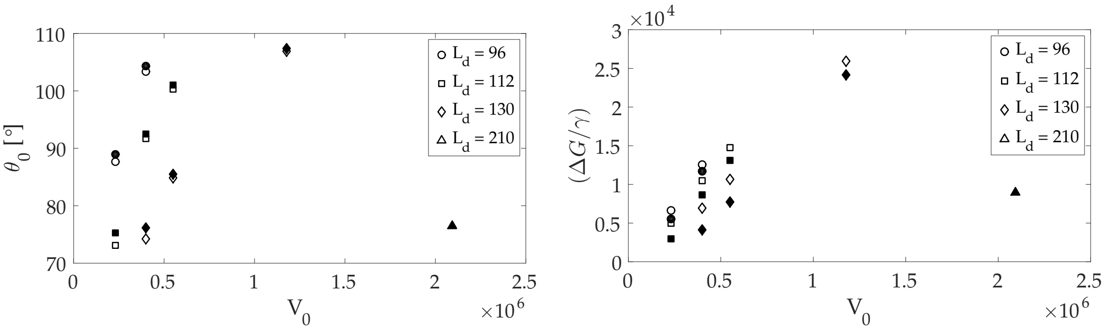

**(a)** Initial apparent contact angle **(b)** $\frac{\Delta g}{\gamma}$

**Figure 4.10:** The apparent initial contact angle $\theta_0$ has been measured, and the difference in interfacial energy $\frac{\Delta G}{\gamma}$ between the beginning and the moment when the droplet depins has been calculated as a function of the initial volume of the droplet. The open symbols correspond to the results obtained with system A and closed symbols depict the results of system B. We learn from this figure that the initial contact angle of the droplet becomes larger if we increase its volume and also the change in interfacial energy becomes larger.

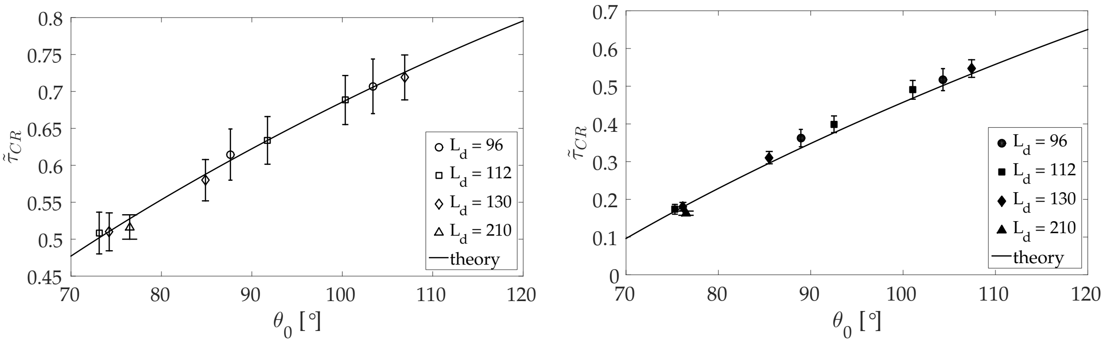

**(a)** system A $\tilde{\tau}_{CR}$

**(b)** system B $\tilde{\tau}_{CR}$

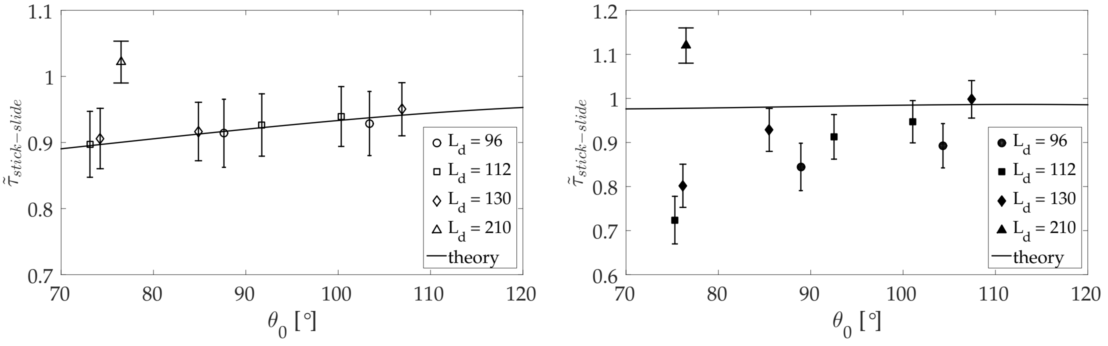

**(c)** system A $\tilde{\tau}_{stick-slide}$

**(d)** system B $\tilde{\tau}_{stick-slide}$

**Figure 4.11:** $\tilde{\tau}_{CR}$ and $\tilde{\tau}_{stick-slide}$ are calculated from the simulations as a function of the initial volume of the droplet. The open symbols correspond to the results obtained with system A and closed symbols depict the results of system B. The results are compared with the theory (solid line). We learn that droplets stay pinned for a longer time in system A than in system B. We see that the calculated values of $\tilde{\tau}_{CR}$ matches the theoretical curve. However, this theoretical curve is drawn with depinning contact angles which we measure from the simulations. It is also clear that the values for $\tilde{\tau}_{stick-slide}$ in system B has a large deviation from the theoretical curve, because the measured diffusion constant changes when the dissolution mode changes from CR to CA. However the data of system A matches the theoretical curve, except for the large droplet which is close to the boundary.

**Table 4.3:** Diffusion Constant determined from the CR mode simulations. The disk diameter and volume of the droplet are varied, whereas $m_{evp} = 0.015$.

| System | Volume | $L_d$ | $D$ |
|---|---|---|---|
| A | $\frac{2}{3}\pi(48)^3$ | 96 | 0.18 ±10% |
| B | $\frac{2}{3}\pi(48)^3$ | 96 | 0.16 ±10% |
| A | $400\times10^3$ | 96 | 0.19 ±10% |
| B | $400\times10^3$ | 96 | 0.16 ±10% |
| A | $\frac{2}{3}\pi(48)^3$ | 112 | 0.18 ±10% |
| B | $\frac{2}{3}\pi(48)^3$ | 112 | 0.13 ±10% |
| A | $400\times10^3$ | 112 | 0.20 ±10% |
| B | $400\times10^3$ | 112 | 0.18 ±10% |
| A | $\frac{2}{3}\pi(64)^3$ | 112 | 0.21 ±10% |
| B | $\frac{2}{3}\pi(64)^3$ | 112 | 0.20 ±10% |
| A | $400\times10^3$ | 130 | 0.20 ±10% |
| B | $400\times10^3$ | 130 | 0.16 ±10% |
| A | $\frac{2}{3}\pi(64)^3$ | 130 | 0.21 ±10% |
| B | $\frac{2}{3}\pi(64)^3$ | 130 | 0.19 ±10% |
| A | $1176\times10^3$ | 130 | 0.24 ±10% |
| B | $1176\times10^3$ | 130 | 0.23 ±10% |
| A | $\frac{2}{3}\pi(100)^3$ | 210 | 0.32 ±10% |
| B | $\frac{2}{3}\pi(100)^3$ | 210 | 0.30 ±10% |

### 4.2.3 Mixed mode

In section 4.2.2 we have studied droplets dissolving in the CR mode. However, as we have seen the droplets do not dissolve solely in the CR mode. They rather switch from dissolving in the CR mode to dissolving in the CA mode. This already resembles one of the mix modes, namely the stick-slide mode. For these simulations the droplets have been deposited on surfaces with just one hydrophilic disk and the rest of the surface being hydrophobic. The droplet thus encounters only one pinning site on the surface. Dietrich et al.[5] mention in their work that the other mixed mode which has been observed in experiments, the stick-jump mode, can be related to spatial variation in surface roughness and pinning sites. To study the dissolution dynamics of the stick-jump mode numerically, we need to add more pinning sites on the surface. Therefore we pattern the surface with concentric rings which have been centered in the system's center on the surface. We use different configurations of hydrophylic and hydrophobic rings. We start with a hydrophilic ring and then switch to a hydrophobic ring consecutively. The last ring is hydrophylic, while the remaining surface is hydrophobic. The spacing between the rings is 15. The different configurations are: $30° - 115°$, $30° - 145°$, $60° - 115°$ and $60° - 145°$. We simulate droplets on two systems: in system C (see fig. 4.12(a)) the last ring has an outer radius of 75 and in system D (see fig. 4.12(b)) the last ring has a radius of 105. A schematic sketch of these two systems and the ring configuration on the surface is given in fig. 4.12.

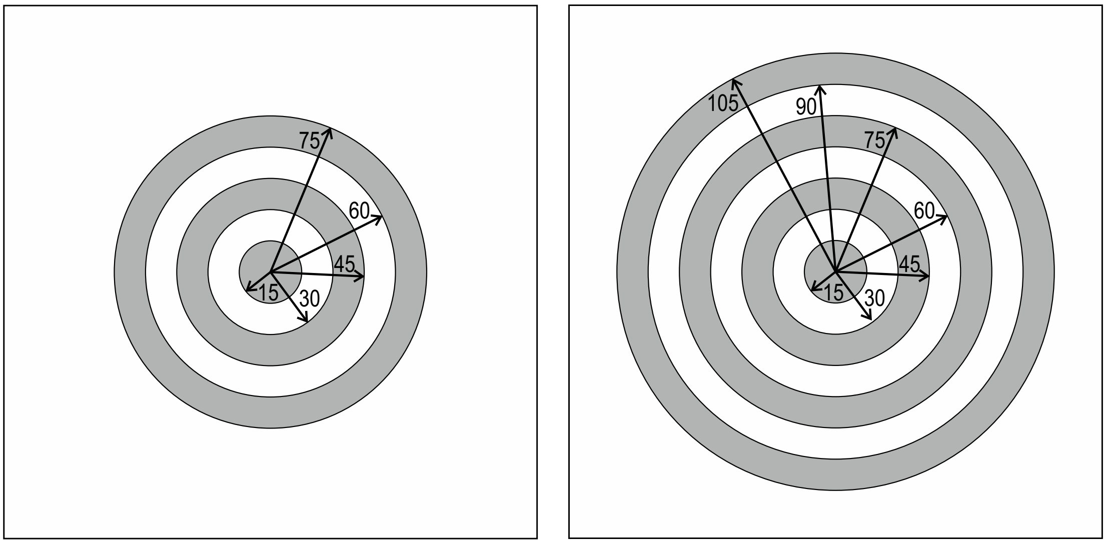

**(a)** System C **(b)** System D

**Figure 4.12:** Sketch of the substrate. Concentric rings are centered at the system's center. The dark rings correspond to the hydrophylic rings , while the other rings and surface are hydrophobic.

We initialize the droplet by depositing it on the last ring. Since the ring is hydrophilic and the wall hydrophobic the droplet gets pinned on the last ring. From fig. 4.13 we infer that the droplet dissolves in the stick-jump mode. In this figure we give the contact angle $\theta$, lateral diameter $L$ and height $H$ as a function of time. We already discussed in section 4.2.2 with the aid of eq. (4.8) the reason why the droplet stays pinned on the ring. After it reaches its equilibrium angle corresponding to the ring, the droplet will depin. When the droplet depins, it moves to the next available hydrophilic ring. At the moment the droplet passes through the hydrophobic ring, the contact angle jumps and the droplet moves to the next available hydrophilic ring and it pins there. If we compare fig. 4.13(a) with fig. 4.13(b), then we infer that the contact angle of the droplet jumps to higher values in the $60^\circ - 115^\circ$ than in the $30^\circ - 115^\circ$. The reason for this might be the pinning strength acting on the droplet, i.e. the droplet experiences a larger pinning force in the $30^\circ - 115^\circ$ configuration. We fit the numerical data for the contact angle as a function of time to the analytical solution of eq. (2.13), just as we did for the results of the CR mode. We find values for the diffusion constant, which we list in table 4.4. From these results we see that the measured diffusion constant changes during the simulation. The reason for this is that the gradient changes as the droplet is dissolving and the distance to the evaporation boundary becomes larger. The diffusion constants are similar to those that are obtained from the CR mode simulations. Also for the larger droplets, system D simulations, we get similar high values for the diffusion constant $D$ as the ones we obtained for the large droplet CR mode simulations. We also compute the energy barrier $\frac{\delta\tilde{G}}{\gamma}$ using eq. (2.18) and give the results for the different jumps in table 4.4. For droplets on the $30^\circ - 115^\circ$ and $30^\circ - 145^\circ$ configuration in system C, the energy barrier becomes smaller, because the lateral diameter becomes smaller. However, for the $60^\circ - 115^\circ$ and $60^\circ - 145^\circ$ configurations, the energy barrier increases. The reason for this is that the contact angle jumps to a higher value, compared to the initial contact angle $\theta_0$. This is also the reason why the barrier becomes larger in system D.

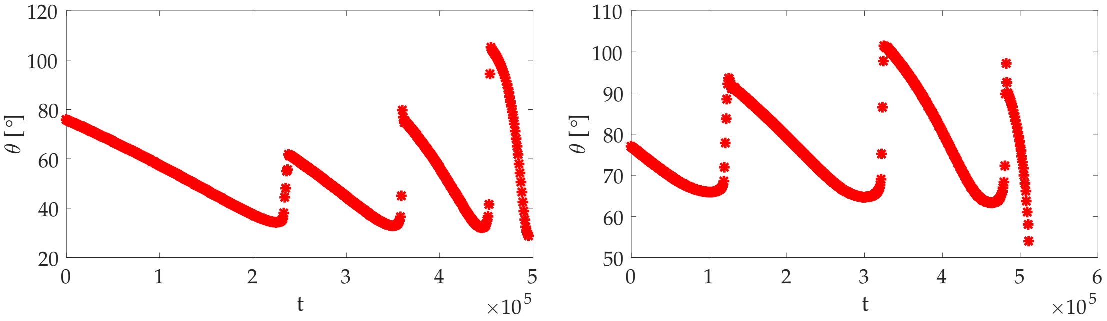

**(a)** Contact angle **(b)** Contact angle

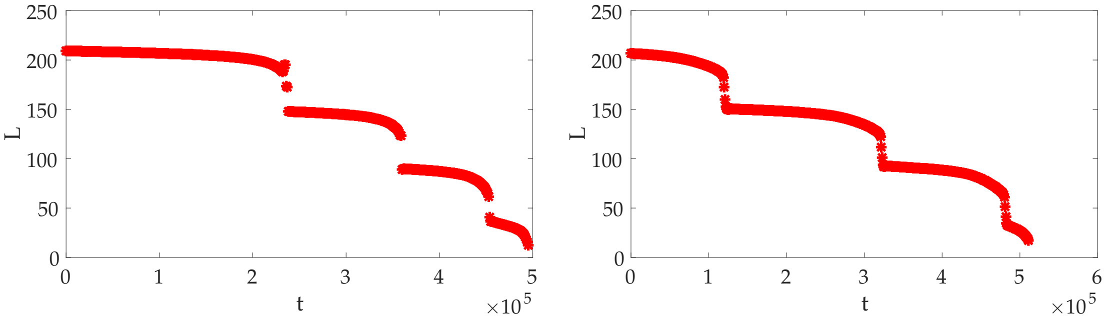

**(c)** Lateral diameter **(d)** Lateral diameter

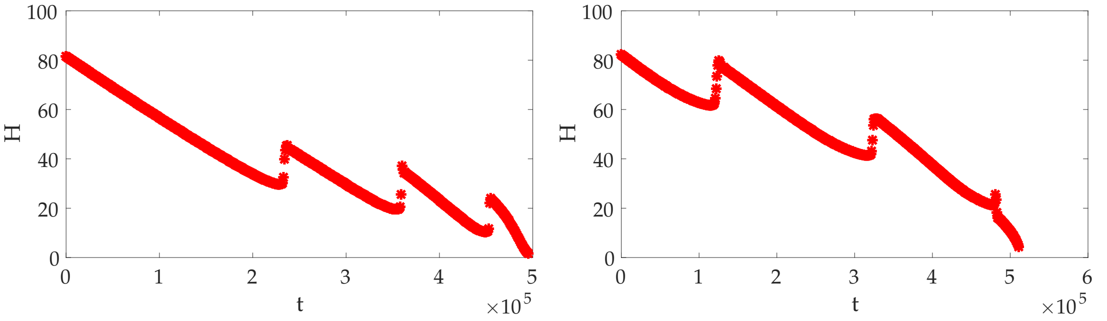

**(e)** Height **(f)** Height

**Figure 4.13:** Stick-jump mode simulations of droplets in system D on a $30° - 115°$ and $60° - 115°$ configuration with $V_0 = \frac{2}{3}\pi(100)^3$ and $m_{evp} = 0.015$. We give the change in contact angle $\theta$, the lateral diameter $L$ and height $H$ of the droplet in time. The left part of the figure depicts the result of a $30° - 115°$ configuration, while the right side of the figure depicts the result of a $60° - 115°$ configurations. We learn from this figure, that when the droplet depins from one hydrophylic ring to quickly move to another hydrophylic ring, the droplet its height and contact angle rapidly increases, thus the droplet "jumps".

**Table 4.4:** Diffusion constant determined from the stick-jump mode simulations and $\frac{\delta\tilde{G}}{\gamma}$. We learn that the diffusion constant becomes smaller if it is farther from the boundary.

| System | Volume | $D_1$ | $D_2$ | $D_3$ | $\frac{\delta\tilde{G}}{\gamma}_1$ | $\frac{\delta\tilde{G}}{\gamma}_2$ | $\frac{\delta\tilde{G}}{\gamma}_3$ |
|---|---|---|---|---|---|---|---|
| C 30-115 | $\frac{2}{3}\pi(70)^3$ | 0.22 ±10% | 0.18 ±10% | | 7.98 | 3.67 | |
| D 30-115 | $\frac{2}{3}\pi(100)^3$ | 0.35 ±10% | 0.22 ±10% | 0.17 ±10% | 11.31 | 3.45 | 5.78 |
| C 30-145 | $\frac{2}{3}\pi(70)^3$ | 0.21 ±10% | 0.17 ±10% | | 7.31 | 3.67 | |
| C 60-115 | $\frac{2}{3}\pi(70)^3$ | 0.21 ±10% | 0.17 ±10% | | 0.42 | 3.36 | |
| D 60-115 | $\frac{2}{3}\pi(100)^3$ | 0.33 ±10% | 0.22 ±10% | 0.17 ±10% | 0.82 | 4.43 | 4.42 |
| C 60-145 | $\frac{2}{3}\pi(70)^3$ | 0.21 ±10% | 0.19 ±10% | | 0.66 | 4.74 | |

## 4.3 Conclusions

We use the lattice Boltzmann model to study the contact line dynamics of dissolnving sessile droplets numerically. Therefore we employ the evaporation model which has been developed by Hessling et al. [1]. To test the consistency of this model we start with a benchmark of a classical problem, the Epstein-Plesset problem [2]. We start with a free spherical droplet in the system center surrounded by a liquid at rest. We simulate the droplets in three different system sizes: $64^3$, $128^3$ and $256^3$, and keep the fluid-fluid interaction parameter $g_{br} = 0.10$ constant. We fit our numerical data to eq. (4.1) to find the diffusion constant. We find that the diffusion constant becomes smaller if we increase the system size. We then continue to simulate droplets with different radii in a $128^3$ system, and also from these results it is clear that the diffusion constant becomes smaller and closer to the actual diffusivity of 0.12, if the droplet is farther away from the system's boundary. In the theory one assumes an infinite system, i.e. a system where the boundary is relatively far away from the droplet. Thus this explains why the measured diffusivity becomes smaller and closer to the actual value of 0.12 of the diffusivity, if the droplet has a larger distance to the system's boundary. This also implies that the theoretical equations are not applicable to a finite system. We then continue to study the influence of the fluid-fluid interaction parameter $g_{br}$ on the equilibrated radius and the diffusion constant. As expected the equilibrated radius increases due to the larger repulsive force from the Shan-Chen model. One would expect that due to this increasing repulsive force, the diffusion constant would become smaller. However, from our results we conclude that the diffusion constant becomes larger. The reason for this is the fact that the surface tension between the droplet and the other fluid increases, if the fluid-fluid interaction parameter becomes larger. For $g_{br} < 0.10$, the droplets are relatively small, thus the Laplace pressure becomes significant, i.e. the diffusion process is mostly pressure driven. For $g_{br} > 0.10$, the surface tension becomes higher, and thus might be more significant to include in the equations than for $g_{br} = 0.10$. Also since the equations are based on infinite system size assumption, we do not perceive the expected trend between the diffusivity and the fluid-fluid interaction parameter $g_{br}$.

To study the contact line dynamics of sessile droplets, we deposit droplets on chemically patterned surfaces in a 256 × 256 × 128 system. For the constant contact angle (CA) mode, we deposit droplets on flat substrates. We fit the results of the lateral diameter to eq. (4.6) and find the diffusion constant. Also here in the end the numerical data deviates from the analytical solution, because there is not much fluid left in the system and the droplet becomes so small, such that the diffusion process is mostly pressure driven, i.e. surface tension becomes significant due to the Laplace pressure. We compare the lifetime of the droplet with the theory. We do so using eq. (2.12), for which we need the initial volume $V_0$ of the droplet, the measured diffusivity, the major and minor density and the time step at which the droplet has completely dissolved. However, a critical remark on this comparison is the fact that we use the measured diffusivity that has been obtained from an equation (see eq. (4.6)) equivalent to eq. (2.12). For the constant radius (CR) mode we pattern the substrate with a hydrophilic disk on an hydrophobic surface. We initialize the droplet on a hydrophilic disk where the droplet gets pinned. When the droplet's volume becomes so small, such that it is energetically more favourable for the droplet to keep its contact angle constant than to keep its lateral diameter constant, the droplet depins, i.e. the droplet switches from dissolving in the CR mode to the CA mode. This resembles the stick-slide mode. We vary the volume of the droplet and the diameter of the hydrophylic disk. Furthermore we define two systems: system A has a hydrophylic disk with a contact angle of 30° and system B has a hydrophylic disk with a contact angle of 60°. In both systems the other part of the surface is hydrophobic with a contact angle of 115°. We find that the initial contact angle and the change in interfacial energy becomes larger if we keep the hydrophilic disk diameter constant and increase the volume of the droplet. We solve eq. (2.13) numerically and fit this solution to the data of the contact angle and find the diffusion constant from it. We compare the lifetime of the droplet to theory, and find that the lifetime closely follows the theoretical values. Again here we use the measured diffusivity from eq. (2.13) to an equivalent equation to determine the lifetime of the droplet. We find that droplet dissolves longer in the CR mode in system A than in system B. We also show that droplet dissolves faster in the CR mode than in the CA mode. However, for the stick-slide mode we find that the lifetime of the droplet dissolving in system B does not match the theoretical curve, because the measured diffusion constant changes, when the droplet switches from the CR to the CA mode. The measured diffusion constant changes, as already discussed, due to the fact that the droplet gets further away from the evaporation boundary and thus the measured diffusion constant becomes smaller. However, in system A the lifetime of the droplet dissolving in the stick-slide mode does match with the theory, because the droplet does not dissolve for a long time in the CA mode, thus the measured diffusivity is not much affected. However, for the droplet that is very close to the evaporation boundary, the droplet dissolves for a relatively longer time in the CA mode, because there is relatively more fluid in system A. This affects the measured diffusivity, which is why the lifetime of the droplet deviates from the theory. We continue to add more pinning sites on the surface, i.e. we pattern the surface with hydrophylic and hydrophobic concentric rings. We find that the droplet jumps between the hydrophilic rings. This implies that if the droplets encounters more hydrophylic disks, it “jumps” to the next energetically favourable position on the surface.

# CHAPTER 5

## Experimental Aspects

In the numerical part of this thesis, we have simulated droplets on chemical heterogeneous surfaces, i.e. surfaces that are patterned with different wettabilities. In this part of the thesis we explore the behaviour of dissolving droplets on rough surfaces. We prepare the samples by a chemical etching process. As mentioned in chapter 2 , surface roughness causes hysteresis. Therefore we perform ARCA (advancing and receding contact angle) measurements to determine contact angle hysteresis. In addition we perform dissolution experiments to characterize the different modes of dissolution and we measure the droplet its contact angle, height and lateral diameter.

### 5.1 Sample preparation

In order to study the influence of surface roughness on the behaviour of dissolving droplets, we first need to prepare samples, i.e. we need to apply roughness on the wafers. For this purpose we use an anisotropic wet chemical etching process. This process of surface roughening is easy and of low cost and provides rather rough surfaces without damaging the bulk structure of the material [46]. The anisotropy of this process refers to the difference of the etch rate at different surface sites, i.e. it is slower in certain directions than other orientations. The chemical reaction for silicon oxide in non-fluoride aqueous solutions which describes this wet chemical etching process with water, is [46]:

$$SiO_2 + 2H_2O = Si(OH)_4 \tag{5.1}$$

The reaction with water happens in three steps as depicted in fig. 5.1, namely adsorption, activated complex formation and hydrolysis [46]. The etching leads to the removal of silicon atoms as $Si(OH)_4$.

To prepare our samples we use ammonium hydroxide, $(NH_4OH)$, due to its mild toxicity and compatibility for working in our laboratory conditions[46]. Subsequently the steps listed below have been followed to prepare samples:

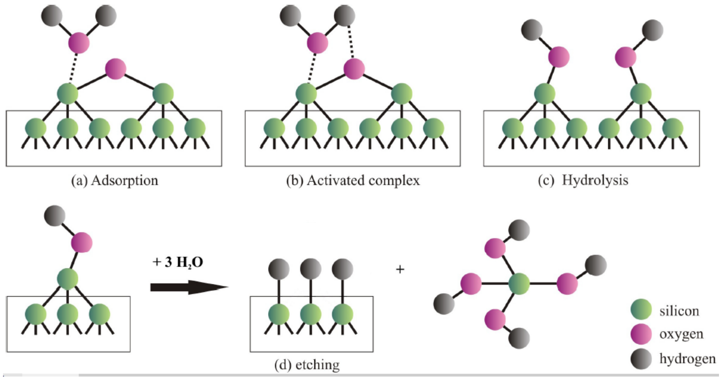

**Figure 5.1:** The three steps of the chemical etching process for silicon oxide in nonfluoride aqueous solutions. Figure taken from Colak [46]

- first we mark the polished silicon wafers and insonicate them in methanol for 15 minutes
- we rinse the wafers with Milli-Q water and dry them with pressurized nitrogen gas
- then mix three parts of sulphuric acid ($H_2SO_4$) with one part of hydrogen peroxide ($H_2O_2$) and individually place wafers in this solution, called piranha, for 10 minutes
- hereafter we rinse the wafers with water at room temperature, then place the wafer in a beaker with hot water in the ultrasonic bath for 15 minutes. After this step we dry the wafers with pressurized nitrogen gas
- for the chemical etching process we mix one part of $NH_4OH$ with 5 parts of water at a temperature of 80 °C. Wafers have been placed for varying amount of time ($t_{etch}$) in this aqueous solution (see table 5.1)
- again we rinse the wafers with Milli-Q water and dry them with pressurized nitrogen gas
- hereafter we place the wafers in a vacuum desiccator to coat them with monoethylperfluorodecyldimethylchlorosilane (PFDDMCS) via chemical vapour deposition
- we insonicate the wafers submerged in chloroform for 15 minutes and then dry them with pressurized nitrogen gas
- hereafter we anneal the wafers for one hour in an oven at 100 °C
- and finally we cut the wafers into samples of ~2 cm$^2$.

**Table 5.1:** Various etching times for each wafer

| **Wafer** | $t_{etch}$**(min.)** |
|---|---|
| 1 | 0 |
| 2 | 0.5 |
| 3 | 1.0 |
| 4 | 2.0 |
| 5 | 3.0 |
| 6 | 4.0 |
| 7 | 5.0 |
| 8 | 6.0 |
| 9 | 7.0 |
| 10 | 8.0 |
| 11 | 9.0 |

Prior to each experiment described in section 5.2, we insonicate the samples submerged in acetone for 10 minutes and after that dry them with pressurized nitrogen gas. To study the influence of the chemical etching process on the surface of the wafers, we have scanned the samples with a Scanning Electron Microscope (SEM) and an optical microscope. Our observations have been depicted in section 6.1.

We have also performed ARCA and dissolution experiments on glass and silicon samples with nanopancakes on them. Nanoimprint lithography (NIL) has been used to create holes. The size of these dots is around 300∼350 nm.

## 5.2 Experimental set-up

### 5.2.1 Droplet dissolution set-up

To study the droplet dissolution behaviour on these rough samples we use a customized set-up, which is schematically depicted in fig. 5.2. After cleaning the sample, we place it at the bottom of a cubic glass container filled with 0.1L of Milli-Q water. Beforehand the Milli-Q water has been stored in a clean glass flask to reach room temperature. In this manner we study the case where we initially have fresh water, i.e. $c_\infty = 0$. During the experiment the droplet dissolves and the water gets contaminated with 1-hexanol ($C_6H_{14}0$) during the experiment. This implies that $c_\infty$ changes, slowing down the dissolution process [7]. The container has been positioned between the light source and the PCO.pixelfly camera, 1392x1040 pixel. Since the difference in the refractive index between water and alcohol is small, we have used a parallel monochromatic light source for illumination, which provides better contrast than standard diffusive (white) light. This is a big advantage, because it eases the detection of the droplet.

The 1-hexanol liquid which has been used during these experiments is supplied by Sigma-Aldrich and is of 99% purity. As the name already implies 1-hexanol is an alcohol with a chain of six carbon atoms and the number in the name stand for the position of the OH-group in the chain, thus for 1-hexanol the OH group is connected to the first carbon atom. The properties of 1-hexanol are: $\rho = 814$ kg/m$^3$, $c_s = 6.13$ kg/m$^3$ [47] and $D = 0.830.10^{-9}$ m$^2$/s [48].

After the container with the sample at its bottom has been positioned on the stage of the set-up, we can deposit 1-hexanol droplets on the sample. We dispense these droplets via glass syringes with stainless steel needles (Hamilton 100 $\mu$L) mounted in a motorized syringe pump. Beforehand the syringe and needle have been rinsed a few times with acetone, then disassembled, dried with nitrogen gas and then reassembled. Hereafter we rinse the syringe with 1-hexanol, since we want to deposit droplets of this fluid on the samples. We set the syringe pump to the desired volume of the droplet. As a precaution that there are no air bubbles within the droplet, a tiny bit of 1-hexanol has been manually drained from the syringe, before depositing the droplet on the sample. After the droplet has been deposited on the sample we start recording the experiment with the camera. After a few images we retract the needle from the container and cover the top of the container with a lid. Since we can measure the outer diameter of the needle, the first image with the needle serves as calibration for image analysis, i.e. we want to convert our experimental data from pixels to real physical units. The camera takes pictures with a frequency of 1 Hz and after the experiment these images are analyzed with a MATLAB code (see section 5.3).

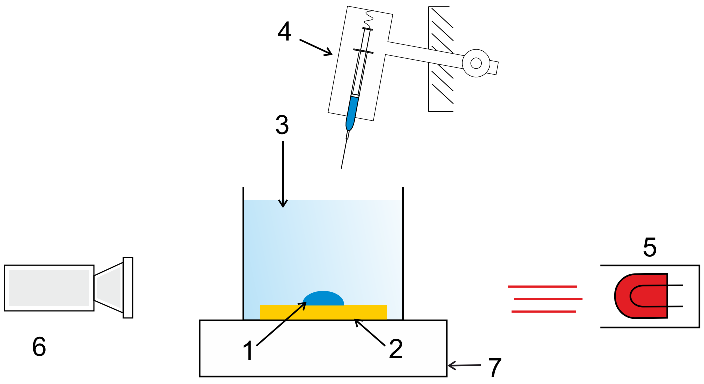

**Figure 5.2:** Schematic illustration of the experimental set-up:1. droplet sitting on 2. the substrate, 3. cubic glass container has been filled with water, 4. syringe filled with the droplet fluid has been attached to a pump, 5. light source with red parallel beam, 6. camera with lens and 7. the stage on which the container has been positioned.

After each experiment there might be residue of 1-hexanol and/or other (non)polar contaminants. Therefore we clean the container thoroughly with ethanol and rinse it with Milli-Q water. And we repeat the process described above before conducting a new experiment.

### 5.2.2 ARCA set-up

In this part of the experiment we examine two systems: sessile water droplets in air and sessile 1-hexanol droplets in water. To measure their advancing and receding contact angle (ARCA) we use the SCA20 software. We replace the camera of the set-up described in section 5.2 with the CCD camera, while the rest of the set-up remains unchanged. The experiments with 1-hexanol droplets in water have been conducted within the glass container and the same glass syringe (Hamilton 100 $\mu$L) has been used. However, for the water droplets we use a different glass syringe (Hamilton 500 $\mu$L) and for this set of experiments we place the samples on the stage of the set-up, thus we have a system of water droplets in air. We perform the ARCA measurements with the SCA20 software, which is supplied by the OCA instruments from Dataphysics to determine contact angles. The software detects the droplet's profile through bright-dark difference (contrast). The contact angle has been determined by a tangent leaning to the droplet's curve at the so called "three-phase contact point" (see fig. 5.3).

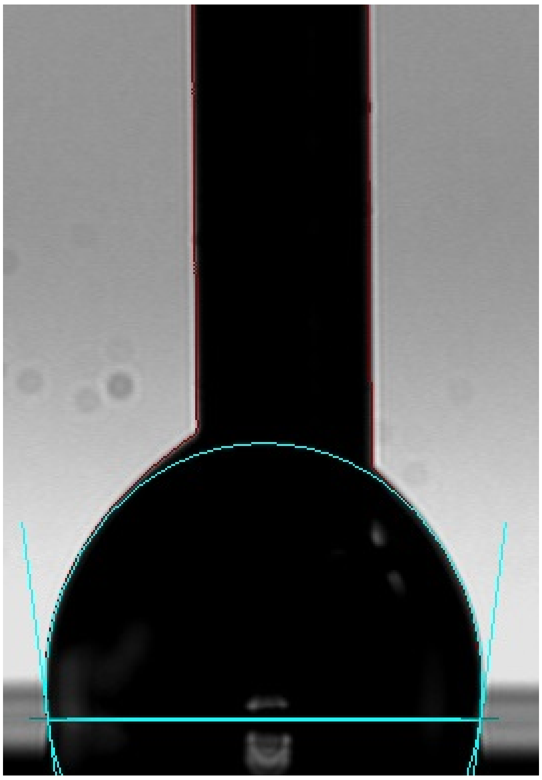

**Figure 5.3:** Profile extraction of the droplet to determine the dynamic contact angle by the SCA20 software during the ARCA measurement.

We start the experiment and the syringe pump automatically dispenses liquid to and reverse dispenses liquid from the droplet, i.e. when we inflate the droplet the interface advances along the sample (advancing angle) and when we deflate the droplet the interface recedes on the sample (receding angle). Due to dynamic tracking of the software it is possible to measure the advancing and receding angle (see fig. 5.4), from which the surface hysteresis has been calculated.

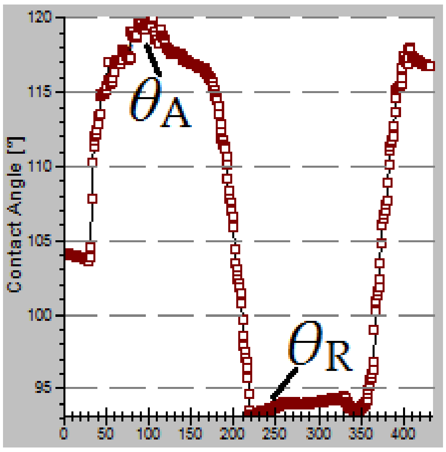

**Figure 5.4:** Dynamic tracking of the droplet's contact angle during the ARCA measurement by the SCA20 software.

## 5.3 Image analysis

As has been stated before, the images have been analysed with MATLAB. The aim is to find the geometric properties of the droplet at any instant in time during the experiment. The code subsequently does the following:

- first of all the user should specify the left and right contact point of the droplet. The line connecting those two points is the baseline of the droplet
- secondly the points on the droplet's edge have been detected by means of the intensity gradient, i.e. the transition from dark (droplet) to light (surrounding medium) causes a large gradient in intensity. If this gradient is higher than the specified threshold, the code detects points on the droplet's edge. Unfortunately also points in the centre of the droplet are detected, but those points are discarded to fit a circle through the actual edge of the droplet
- the gradients have been used again to detect fit points, but now along the lines normal to the fitted circle. We use a three point parabolic assumption to find the inflection point of the intensity gradient with sub-pixel accuracy. This assumption also makes this detection independent of the light intensities of the image.
- these fit points have been used to fit a new circle. The information of this circle determines our droplet parameters in which we are interested (see eq. (2.3)).

# CHAPTER 6

## Experimental Results and Discussion

### 6.1 Images of the wafers

We use a Scanning Electron Microscope (ZEISS MERLIN HR-SEM) and an optical microscope (LEICA DM2500 MH) to image different samples from each wafer. From the images in figs. 6.1 and 6.2 we learn that pyramidal hillocks with different sizes randomly distributed on the wafers appear. The etching time of wafer numbers are according to table 5.1. These hillocks only appear if the following four conditions are satisfied simultaneously [49]: (i) existence of a micromasking agent which stabilizes the apex atom/s, (ii) a fast downward motion of the floor surface, (iii) stable edges and (iv) very stable pyramidal facets. If any of these conditions fail, the pyramidal hillocks do not form. If the stabilizing condition is not present, shallow round pits may appear on the surface. Due to this, pyramidal hillocks and shallow round pits never appear together on a surface [50]. The density of the hillocks on the surface decreases with an increasing concentration of the etchant and the density increases with increasing temperature of the etching process [49, 50]. The inhomogeneous sizes of the pyramidal hillocks indicates that the they form continuously during the etching process [50]. Compared to Colak [46] we do observe pyramidal hillocks for every amount of etching time. However, from fig. 6.1 it is clear that this depends on which part of the surface we image. As has been stated already, the temperature and concentration are important parameters for the formation pyramidal hillocks. During the etching process the temperature changes from 65 °C in the beginning to 85 °C in the end. It is rather difficult to keep the temperature constant during the etchant process, because it rises during the process. When pouring $NH_4OH$ to water at 80 °C, the temperature first drops and then gradually increases. In case of wafer 7 the temperature rose above 80 °C. On the contrary to what Colak [46] has reported, the wafers that have been etched for 4 minutes (see figs. 6.1(b) and 6.1(c)) and 5 minutes (see figs. 6.1(d) to 6.1(f)) do show extensive hillock formation. The reason for this being during the etching process a lot of bubbles start appearing, which in this case can be hydrogen bubbles. It has been reported that hydrogen bubbles induces the formation of hillocks on the evolving surface by serving as a micromask before detachment [50]. Also the concentration may be different during all of the processes, but not significant. In conclusion the temperature is difficult to control during the process and gives different texture to each wafer. Thus the amount of etching time is not the only parameter that determines the pyramidal hillock density. This problem may be solved by heating up the water above 80 °C, which will bring it closer to 80 °C after pouring the $NH_4OH$ to the water.

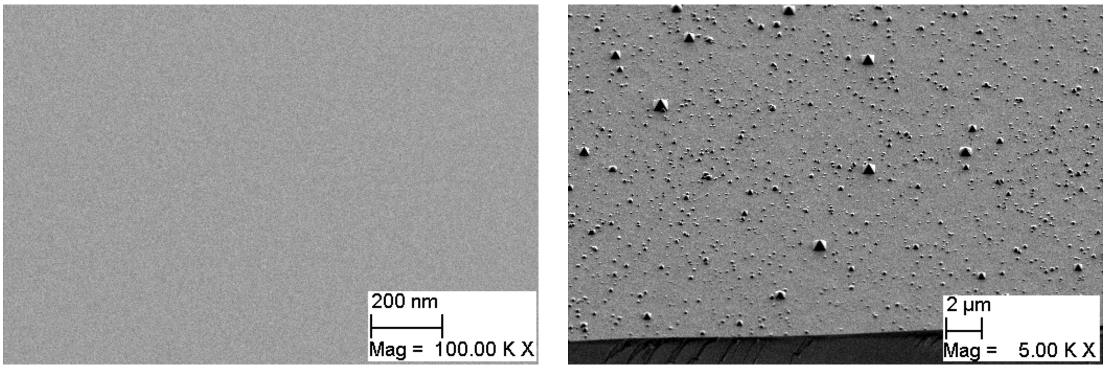

**(a)** Wafer 1 ($t_{etch} = 0$ min) **(b)** Wafer 6 ($t_{etch} = 4$ min)

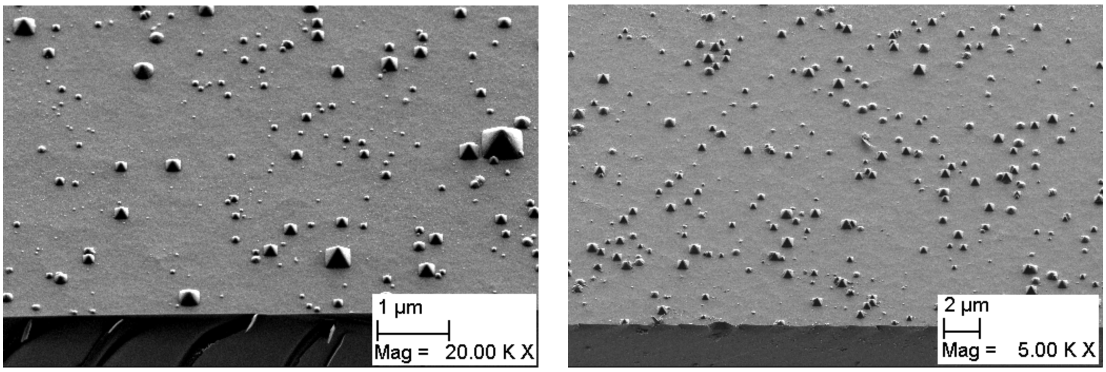

**(c)** Wafer 6 ($t_{etch} = 4$ min) **(d)** Wafer 7 ($t_{etch} = 5$ min) sample 1

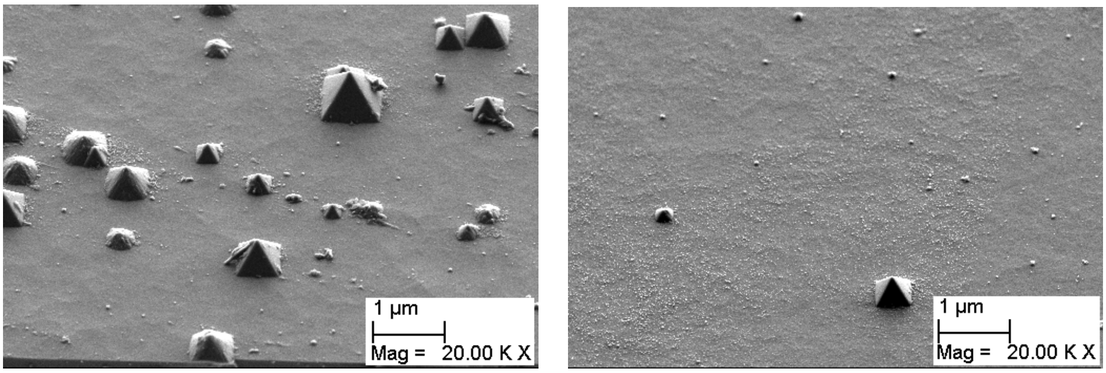

**(e)** Wafer 7 ($t_{etch} = 5$ min) sample 1 **(f)** Wafer 7 ($t_{etch} = 5$ min) sample 2

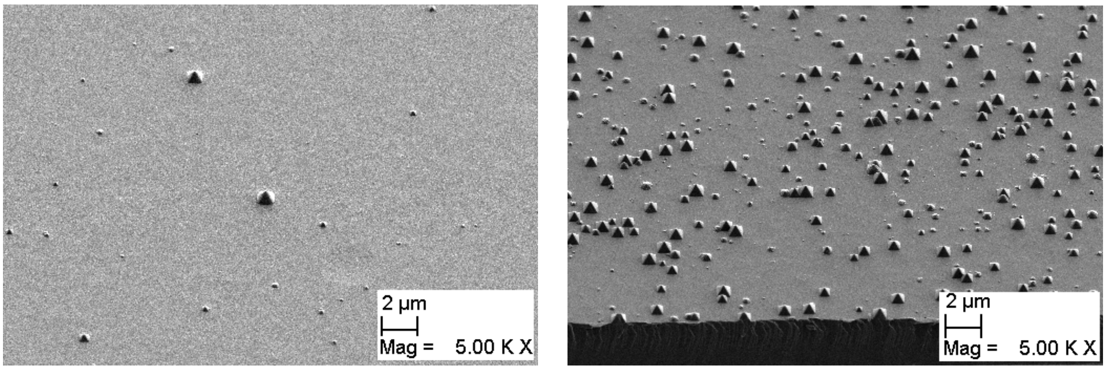

**(g)** Wafer 8 ($t_{etch} = 6$ min) sample 1 **(h)** Wafer 8 ($t_{etch} = 6$ min) sample 2

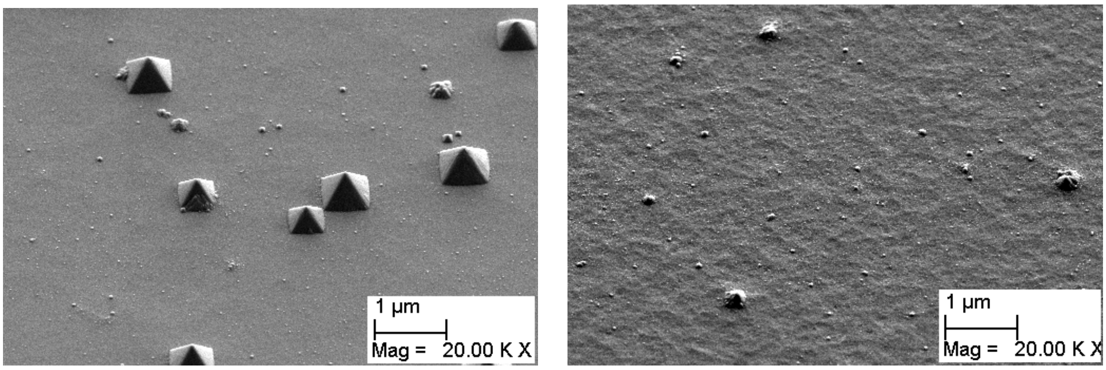

**(i)** Wafer 8 ($t_{etch} = 6$ min) sample 2 **(j)** Wafer 9 ($t_{etch} = 7$ min) sample 1

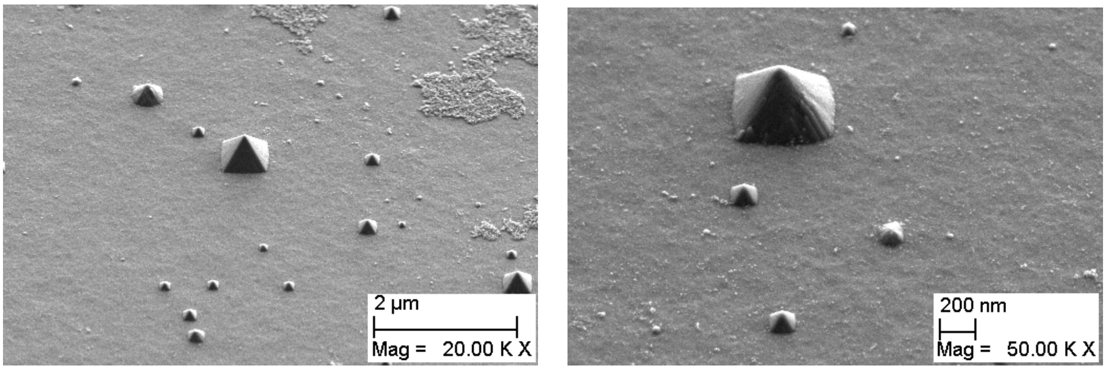

**(k)** Wafer 9 ($t_{etch} = 7$ min) sample 2 **(l)** Wafer 9 ($t_{etch} = 7$ min) sample 2

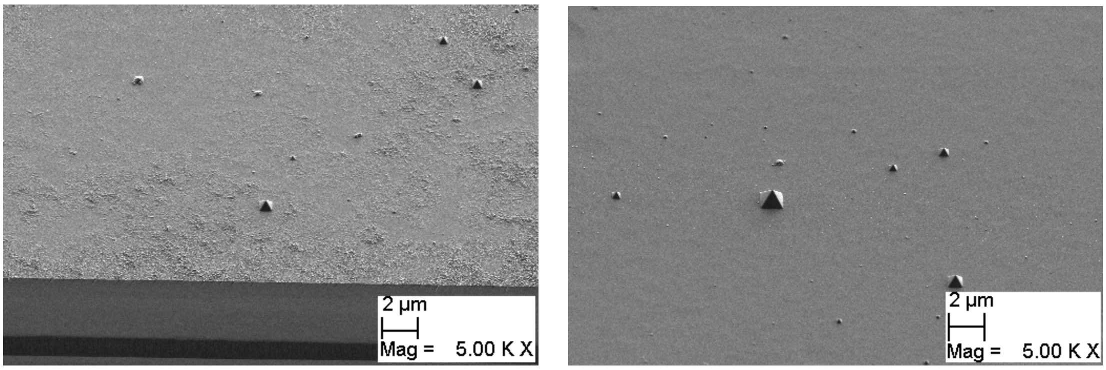

**(m)** Wafer 10 ($t_{etch} = 8$ min) sample 1 **(n)** Wafer 10 ($t_{etch} = 8$ min) sample 2

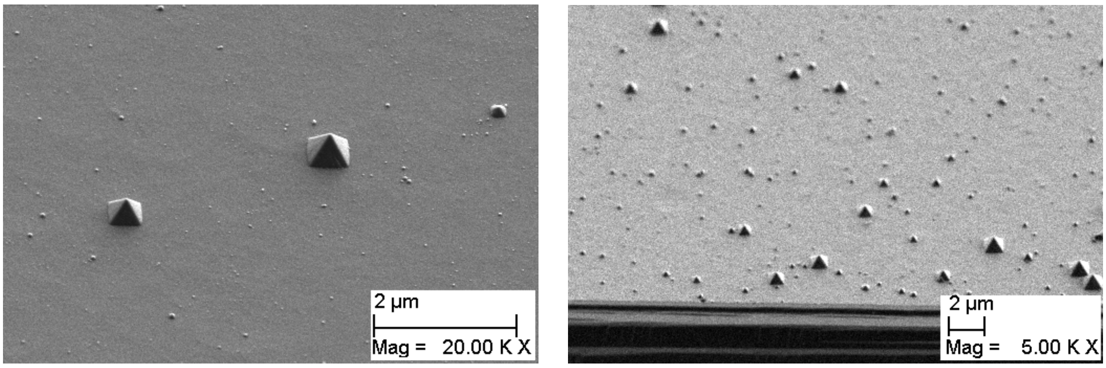

**(o)** Wafer 10 ($t_{etch} = 8$ min) sample 2 **(p)** Wafer 11 ($t_{etch} = 9$ min) sample 1

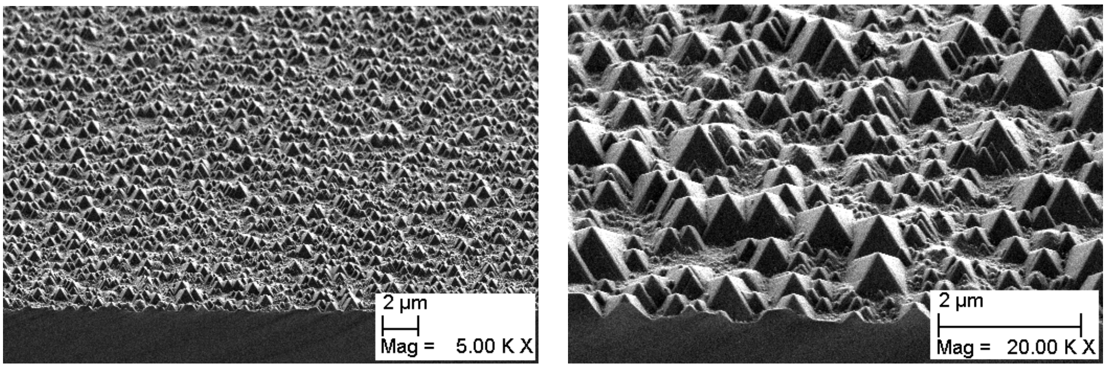

**(q)** Wafer 11 ($t_{etch} = 9$ min) sample 2 **(r)** Wafer 11 ($t_{etch} = 9$ min) sample 2

**Figure 6.1:** Scanning Electron Microscope (SEM) images with different magnification of different samples from wafers with different etching times $t_{etch}$.

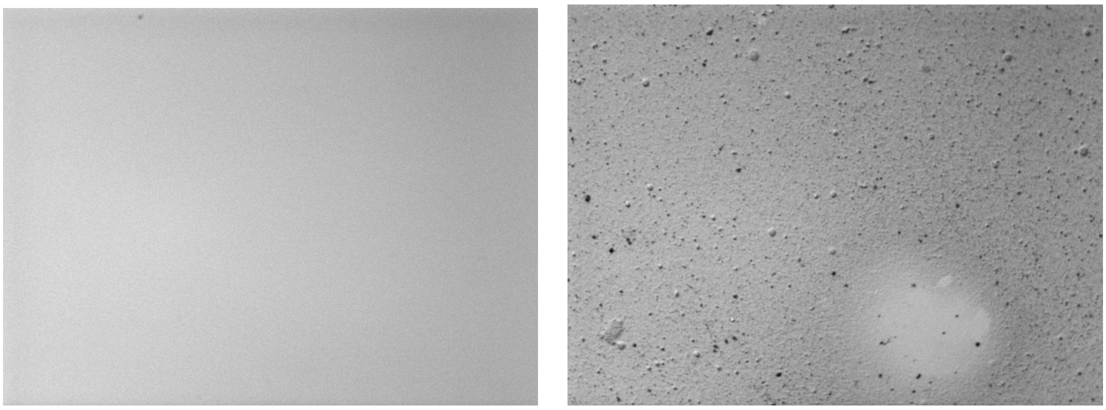

**(a)** Wafer 1 ($t_{etch} = 0$ min) **(b)** Wafer 2 ($t_{etch} = 0.5$ min)

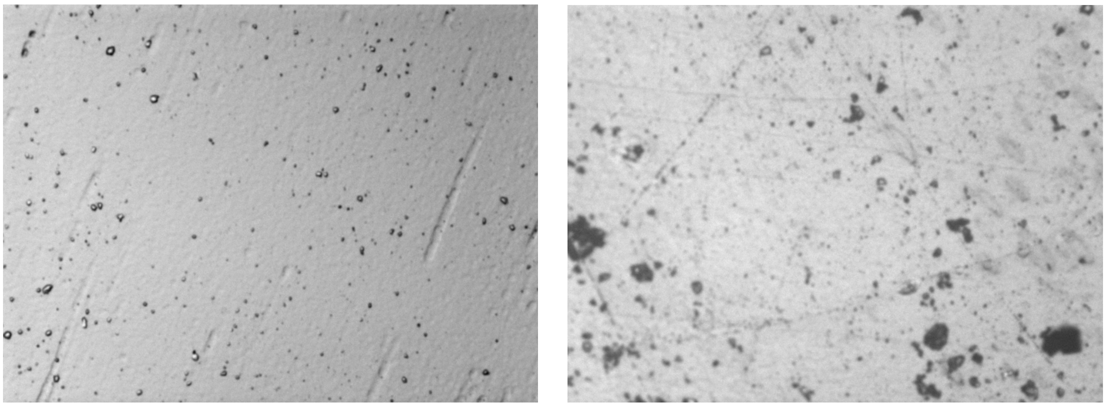

**(c)** Wafer 3 ($t_{etch} = 1$ min) **(d)** Wafer 4 ($t_{etch} = 2$ min)

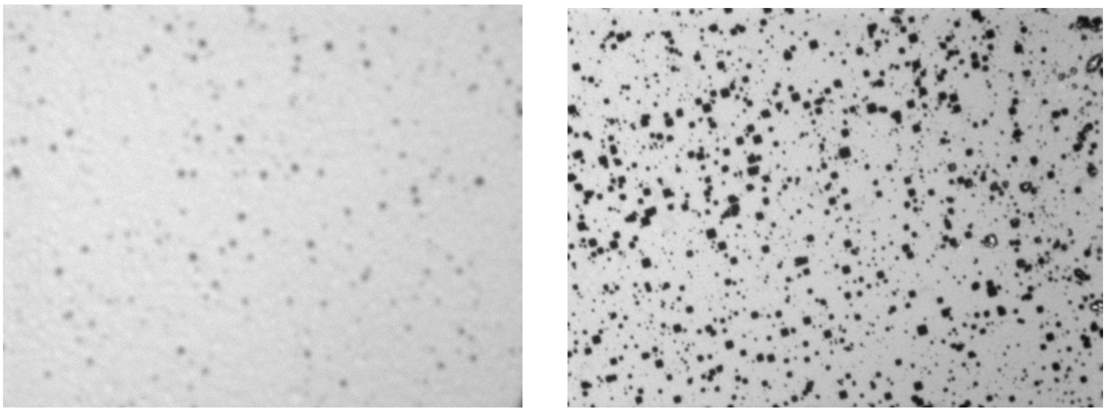

**(e)** Wafer 5 ($t_{etch} = 3$ min) **(f)** Wafer 11 ($t_{etch} = 9$ min)

**Figure 6.2:** Images of the etched samples taken with an optical microscope with a water immersed objective with a 63x magnification.

## 6.2 ARCA experiments

We perform ARCA measurements on three different samples of each wafer. On each sample we measure the advancing and receding contact angle on three different positions, i.e. we measure nine contact angles on each wafer. As has been stated already in section 5.2.2 we perform the ARCA measurements in two systems: (i) water-air system and (ii) hexanol-water system. In fig. 6.3 we depict the results of the advancing contact angle, the receding contact angle and the hysteresis as a function of the amount of etching time for the different wafers. From this figure we can infer that due to the randomly distributed pyramidal hillocks, we have large spread in the data. Furthermore we learn from the same figure that the etching process enhances hysteresis, because the average hysteresis increases for the etched wafers compared to our unetched wafer. The advancing angle $\theta_A$ and receding angle $\theta_R$ that have been measured are not equal for both systems due to the different surface tensions in both systems. It is has been reported [12, 51, 52] that the contact angle hysteresis increases with the surface defect density until it reaches a critical value for the defect density. This critical value depends on the surface tension between the droplet and surrounding fluid, the size of the defect and the range of deformation of the contact line. Above this critical value the hysteresis starts decreasing. The reason for this being the fact that at low defect density the contact line is individually pinned by the defects, whereas at a higher defect concentration an overlap in deformation of the contact line occurs which leads to a collective effect in pinning of the contact line [12, 51, 52]. As we can infer from fig. 6.1 the roughness on our wafers is inhomogeneous. This implies that the hysteresis depends on which part of the sample the experiment has been performed. A consequence of this varying roughness is the large variation in the hysteresis measurements (see fig. 6.3). It is therefore difficult to state on which wafer the droplet experiences the largest hysteresis. If we first consider the hexanol droplet in water system, then it is plausible that wafer 11 ($t_{etch} = 9$ minutes) does not have the largest hysteresis due to high defect density on some parts of this wafer as depicted in figs. 6.1(q) and 6.1(r), i.e. this sample is fully covered with pyramidal hillocks. However, if we study the images (see figs. 6.1(m) to 6.1(o)) and ARCA results of sample 10 than one would expect small hysteresis, due to the lower surface defect density compared to wafer 11. This seems to be true for the hexanol-water system, but not for the water-air system, where it also has a large spread in the measurements. This is not odd, because it is significant to mention that not all samples of each wafer have been scanned and that just a part of each sample has been imaged. Moreover, the three spots on the samples on which the ARCA measurements have been performed are different for both systems. It is rather difficult to perform the experiments on the exact same spots, because these spots have not been marked.

In fig. 6.4 we plot the hysteresis that has been measured in the water-air system as a function of the hysteresis measured in the hexanol-water system. For the etched wafers it is clear that the hysteresis for the water droplet in air system increases as a function of the hysteresis measured for the hexanol droplet in water system until it reaches a plateau. This implies that the hysteresis is independent of the amount of etching time after one minute. For the samples prepared with nanopancakes the hysteresis for the silicon wafers drops, whereas it increases for the glass samples.

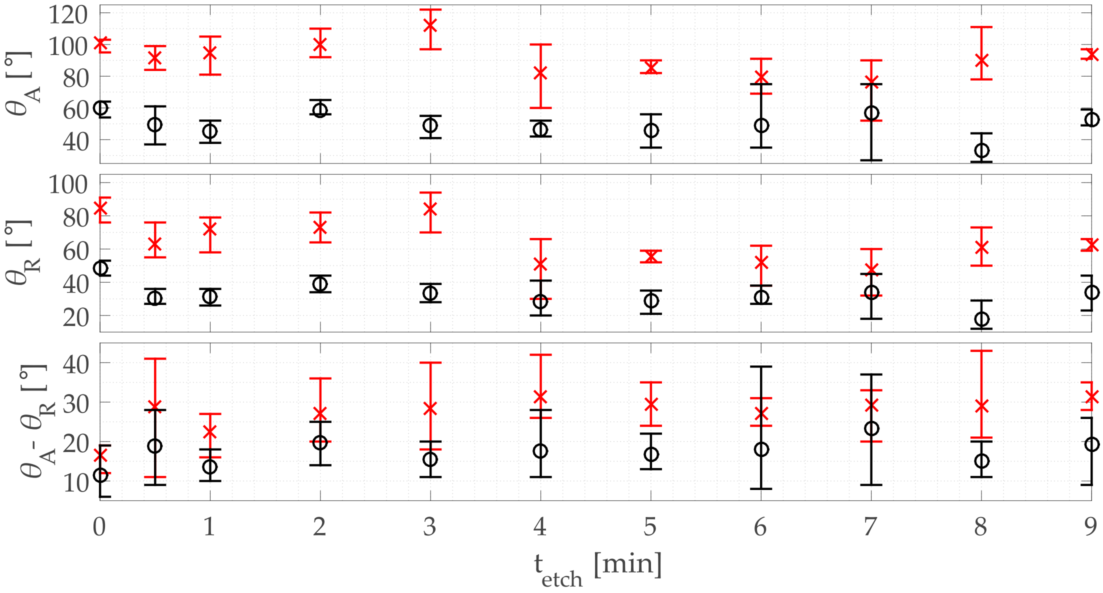

**Figure 6.3:** The ARCA measurements for two systems, namely: waterdroplets in air, marked with ×, and the hexanol droplets in water, marked with ○, as a function of ethcing time of the wafers $t_{etch}$.

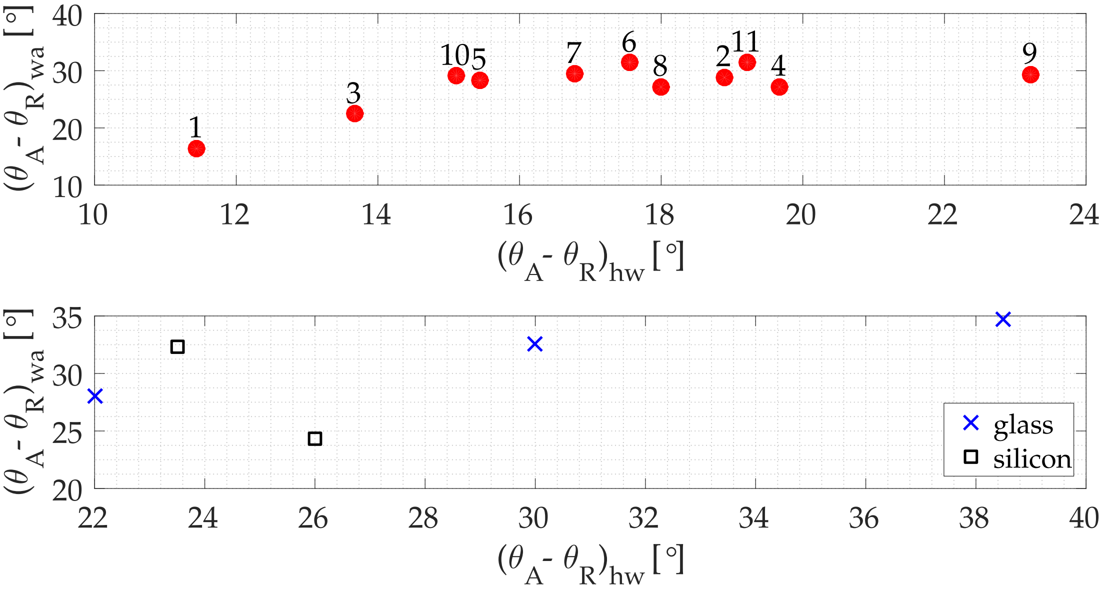

**Figure 6.4:** The average contact angle hysteresis measured in the water-air system (wa) as a function of the average hysteresis measured in the hexanol-water system (hw). The top plot correspond to measurements performed on the etched wafers and the bottom figure corresponds to the measurements performed on the samples prepared with nanopancakes.

## 6.3 Dissolution experiments

Dissolution experiments have been performed on three different samples from each wafer. We only observe the stick-slide and stick-jump mode during these experiments. This is in agreement with our expectation, because we have prepared the samples with roughness (physical heterogeneities). In practice usually the mixed modes have been observed due to the heterogeneities which are omnipresent on samples. In fig. 6.5 we depict the initial contact angle $\theta_0$, the depinning contact angle $\theta_d$ and the difference between these two angles as a function of the average hysteresis of the wafers. We directly learn from this figure that more droplets dissolve in the the stick-slide mode than in the stick-jump mode. For wafers with low contact angle hysteresis only the stick-slide mode has been observed. The reason for these observations might be the pinning strength of the pyramidal hillocks on the droplet and also the low density of pyramidal hillocks on the surface. If we first consider fig. 6.5 then it is clear that the initial contact angle $\theta_0$ is smaller on the etched samples than the unetched sample. In some cases the difference between $\theta_0$ on the etched samples and the unetched samples is rather small and in some rather large. It should be noted that the initial contact angle also depends on the way the droplet has been deposited on the sample. Wenzel's model suggests that surface roughness enhances the wettability of the surface, i.e. the initial contact angles are smaller on etched samples than on unetched samples. The angle at which the droplet starts depinning on etched samples is smaller than on the reference wafer. From section 6.1 it is already clear that we have a spatial variation of surface roughness on etched samples. This leads to a difference in pinning force on the droplet, which results in varying depinning contact angles on the wafers. The wafer that is etched the longest, have less spatial variation, giving comparable depinning contact angles and more droplets that dissolve in the stick slide mode. We depict $\theta_j$ and the difference between this contact angle and the depinning contact angle as a function of the hysteresis for the stick-jump mode in fig. 6.6. In some cases the difference between $\theta_j$ and $\theta_d$ is small. This might be due to the low surface defect density and different pinning strength of the contact line by the pyramidal hillocks. In fig. 6.7 the time, $t$, at which the droplet depins for the first time is presented as a function of the hysteresis. This time is normalized by the lifetime of the droplet $t_{life}$ as $t_{norm} = \frac{t}{t_{life}}$. We already know from eq. (2.5) that the dissolution time of the droplet also depends on its contact angle, i.e. the wall correction factor accounts for this. In their work Zhang et al. [7] have shown that droplets with same size and contact angle have different lifetimes due to the pinning strength at different pinning sites.

From these results we infer that we are unable to predict in which of the dissolution dynamic mode the droplets dissolve. We ascribe these observations to the pyramid shape of the structures on the wafers (see fig. 6.8). Apparently the size of the pyramidal hillocks does not effect the pinning strength, but it rather depends on the inclination of the planes. This implies that rougher substrates (a larger density of pyramidal hillocks) and/or substrates with larger pyramidal hillocks, do not exert larger pinning strengths on the droplet. Another reason for our observations are the fact that the droplet experiences different pinning strengths due to non-uniformity of the surface roughness.

Furthermore we have conducted measurements on both glass and silicon samples patterned with dots (nanopancakes). The dots have a diameter of 300 nm and 350 nm and the spacing between the dots is 300 nm and 350 nm respectively. These dots have been created with nanoimprint litography. The experiments which have been performed on glass and silicon samples with nanopancakes gave only droplets dissolving in the stick-jump mode as a result (see figs. 6.9 to 6.11). It should be noted that after performing the ARCA experiments on the silicon samples, they shattered into small pieces during insonication. For the dissolution experiments the silicon samples have therefore been rinsed thoroughly with ethanol and acetone. The glass samples have been cleaned in the exact same way as the samples of the etched wafers. The glass samples have an intrinsic roughness. However in most cases the initial contact angle, $\theta_0$ and the depinning contact angle, $\theta_d$, of the silicon samples and glass samples are comparable. This implies that the contact line experiences a comparable pinning force due to the nanopancakes.

We have also calculated the energy barrier $\delta\tilde{G}$ (see fig. 6.12) associated with the experiments where the stick-jump mode has been observed, using eq. (2.18). For the etched samples the results may be different due to the size of the pyramidal hillocks.

For larger pyramidal hillocks more energy is required for the droplet to make the jump. For the samples prepared with nanopancakes the energy barrier is for some experiments of the same order of magnitude and for some it is not. The reason for this might be that the pancakes exerts different pinning forces on the droplet and in case of the silicon wafers there might be some leftover dust particles.

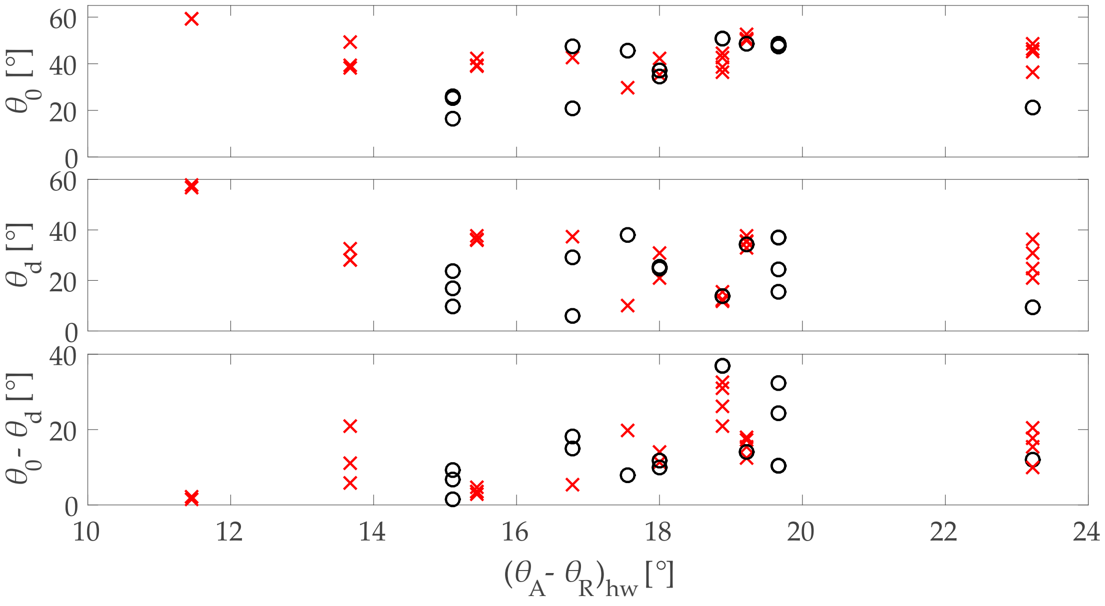

**Figure 6.5:** Measured initial contact angle (top figure), depinning contact angle (middle figure) and the difference between these two angles (bottom figure) as a function of the average hysteresis of the wafers on which the dissolution experiments are performed. Here the experiments in which the droplets dissolved in the stick-slide mode are marked with ×, and the droplets that dissolved in the stick-jump mode are marked with ∘.
]

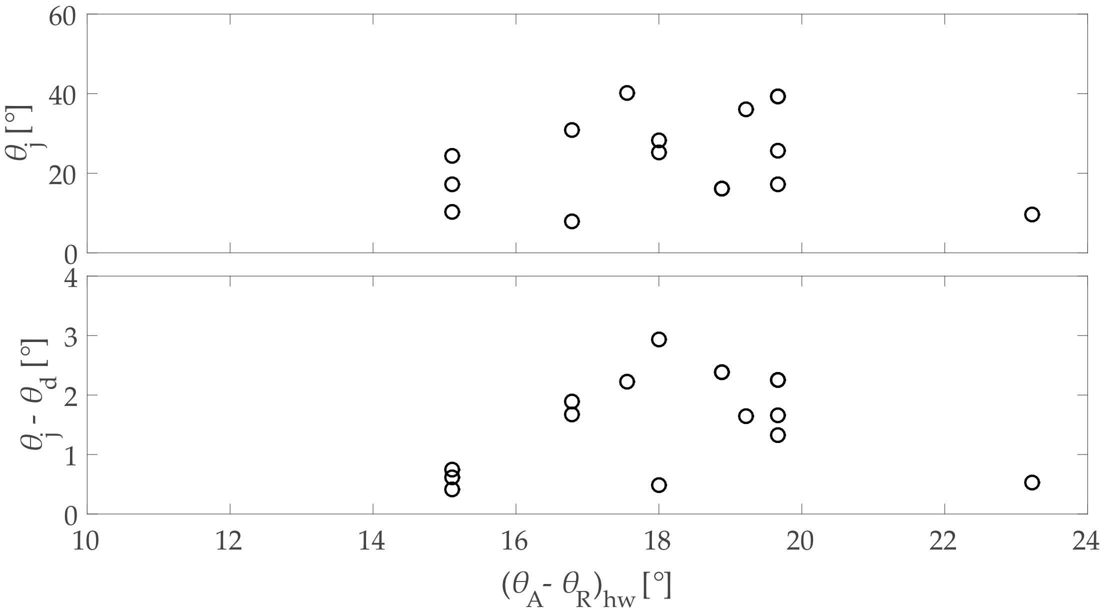

**Figure 6.6:** $\theta_j$ and the difference between this angle and the depinning angle $\theta_d$ as a function of the average hysteresis of the wafers on which the dissolution experiments are performed.

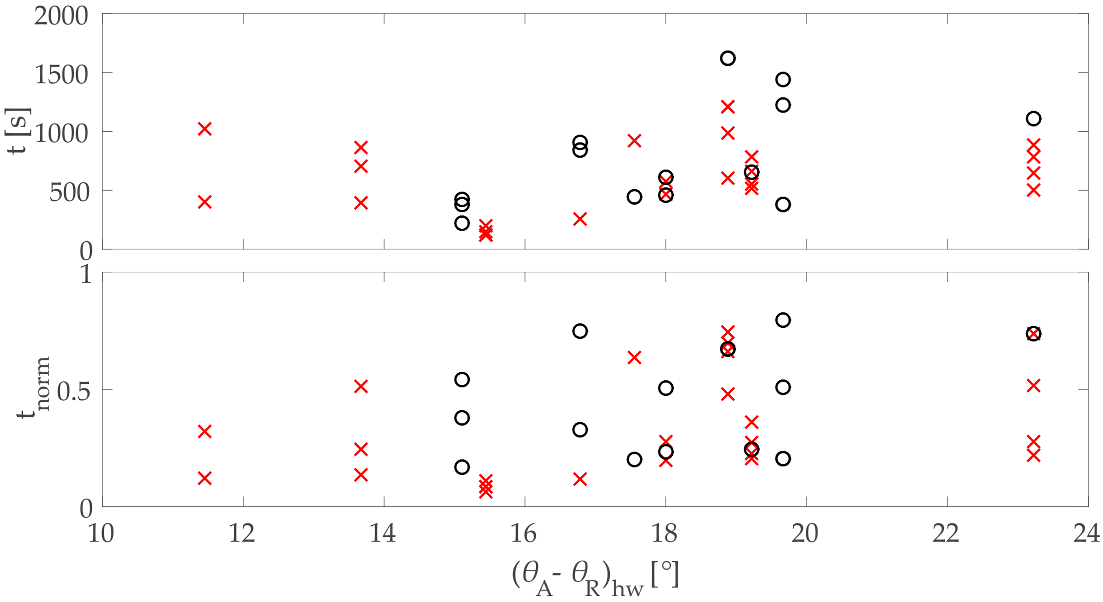

**Figure 6.7:** The time $t$ at which the droplet first depins and the the normalized time $t_{norm}$ are plotted as a function of the average hysteresis of the wafers on which the dissolution experiments are performed. Here the experiments in which the droplets dissolved in the stick-slide mode are marked with ×, and the droplets that dissolved in the stick-jump mode are marked with ∘.

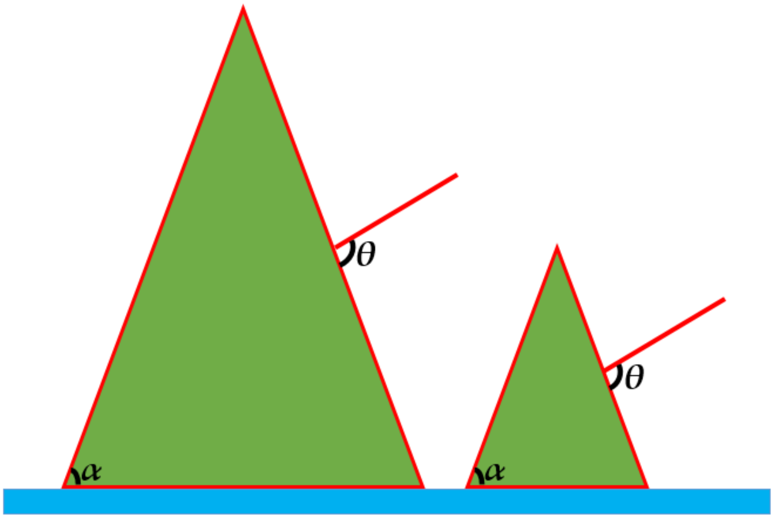

**Figure 6.8:** Crosssection of different sizes of pyramidal hillocks with same inclination $\alpha$ on which the contact line is pinned.

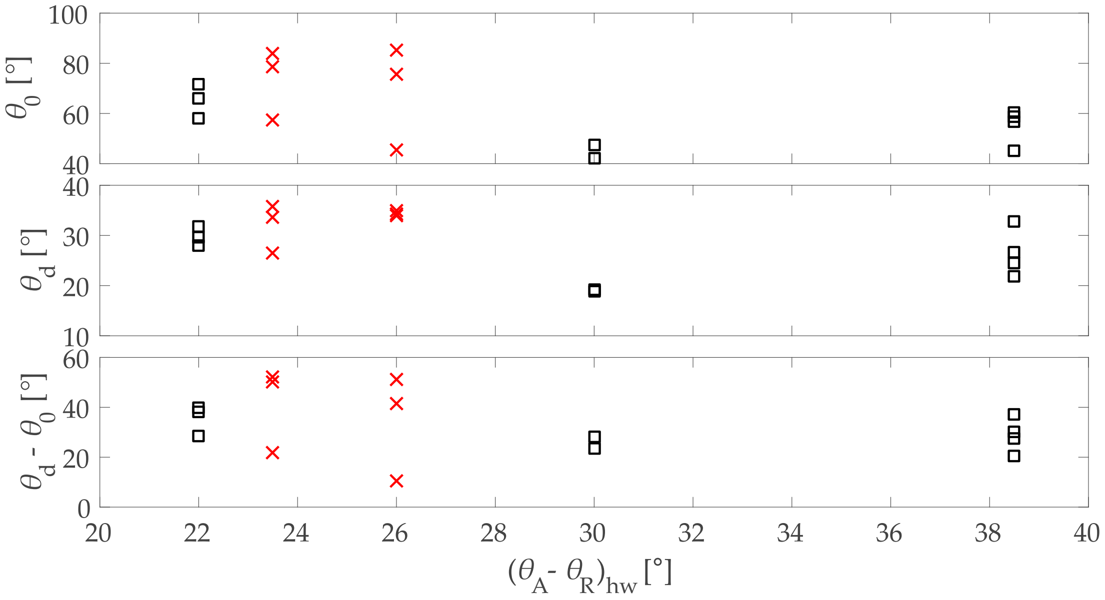

**Figure 6.9:** Measured initial contact angle (top figure), depinning contact angle (middle figure) and the difference between these two angles (bottom figure) as a function of the average hysteresis of the samples. Here the experiments performed on the silicon samples are marked with ×, and the experiments performed on the glass samples are marked with □.

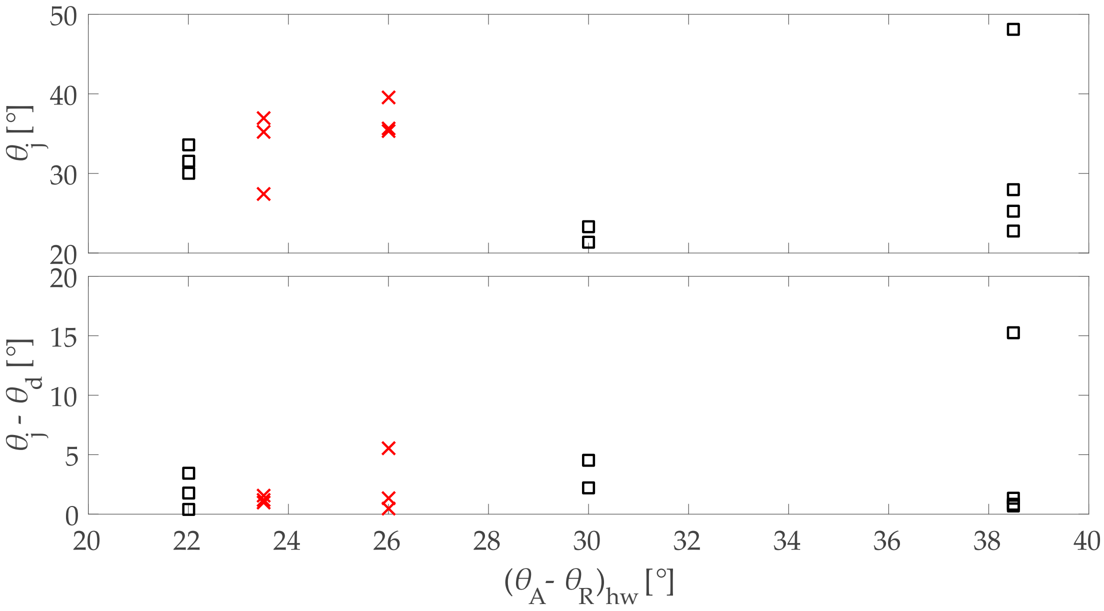

**Figure 6.10:** $\theta_j$ and the difference between this angle and the depinning angle $\theta_d$ as a function of the average hysteresis of the samples. Here the experiments performed on the silicon samples are marked with ×, and the experiments performed on the glass samples are marked with □.

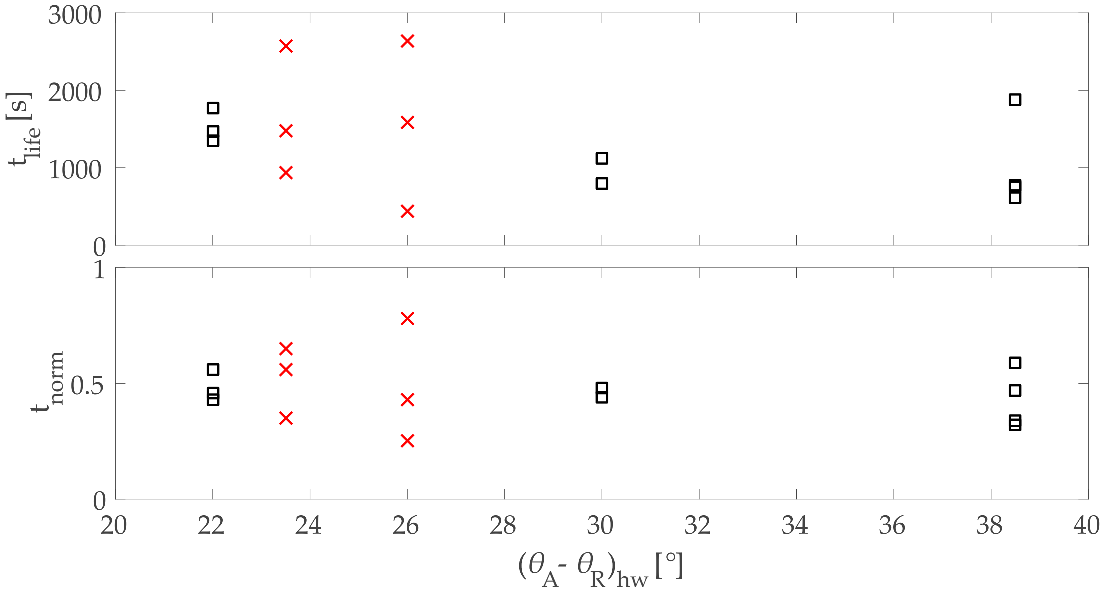

**Figure 6.11:** The time $t$ at which the droplet first depins and the the normalized time $t_{norm}$ are plotted as a function of the average hysteresis of the samples. Here the experiments performed on the silicon samples are marked with ×, and the experiments performed on the glass samples are marked with □.

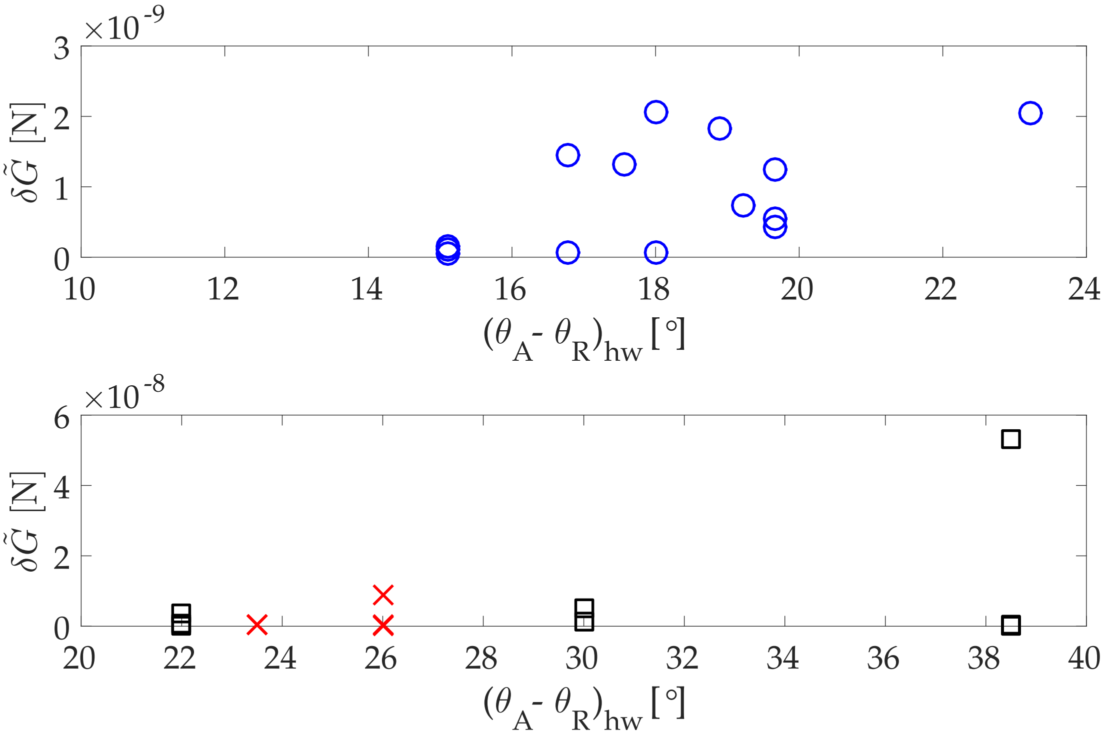

**Figure 6.12:** $\delta\tilde{G}$ calculated using eq. (2.18) for the samples with pyramidal hillocks (top figure) and the samples covered with nanopancakes (bottom figure) as a function of the contact angle hysteresis.

## 6.4 Conclusions

In order to study the effect of physical heterogeneities on the contact line dynamics of dissolving sessile droplets, we apply an anisotropic wet chemical etching process. We place silicon wafers in an non-fluoride aqueous solution of water at a temperature of 80 °C with $NH_4OH$ as an etchant. This etching process leads to the removal of silicon atoms as $Si(OH)_4$ after silicon oxide has reacted with water. We vary the total amount of etching time $t_{etch}$ between 30 seconds and 9 minutes. We image different samples from the etched silicon wafers with a Scanning Electron Microscope (SEM) and an optical microscope. We compare these images to the images of an unetched wafer and we infer that this etching process has led to formation of pyramidal hillocks on the surface. Furthermore we find that these pyramidal hillocks are randomly distributed on the surface. The wafer that has been etched the longest ($t_{etch} = 9$ minutes), has the largest pyramidal hillock structures. However, for all the wafers it is clear that the density of the pyramidal hillocks depends on which sample from the wafer has been imaged. The reason for this is two fold: during the etching process the temperature varies, i.e. when pouring the $NH_4OH$ to the hot water the temperature first drops and during the etching process the temperature rises again. The hillock formation increases when the temperature rises. Another reason is that during the process bubbles starts appearing. It is plausible that these bubbles are hydrogen bubbles, which induces the formation of these hillocks.

We know that surface roughness enhances contact angle hysteresis. Therefore we measure the advancing and receding contact angle (ARCA) of droplets on the surfaces, from which we can determine the contact angle hysteresis. For these hysteresis measurements we examine two systems: sessile water droplets in air and sessile 1-hexanol droplets in water. The ARCA measurements are conducted using SCA20 software, which detects the droplet's profile through contrast and it draws a tangent leaning to the droplet's curve at the "three-phase contact point". From this the dynamic contact angle of the droplet has been measured. We perform these ARCA measurements on three different samples of each wafer. We conduct these ARCA measurement at three different positions on each sample, i.e. we have nine measurements on each wafer. We find that on average the hysteresis increases for the etched wafers compared to the unetched wafers. However, the data shows a large spread and inconsistency due to the spatial variation of the pyramidal hillocks. Therefore it is difficult to state how the amount of etching time influences the contact angle hysteresis. The wafer that has been etched the longest, $t_{etch} = 9$ minutes does not necessarily has the largest contact angle hysteresis, because it has been reported [12, 51, 52] that the hysteresis increases until it reaches a critical value for the defect density. In our case there is a spatial variation in the density of the pyramidal hillocks.

We continue with experiments on dissolving sessile droplets. We deposit 1-hexanol droplets on samples of each of the wafers. We use three different samples form each wafer. Water surrounds the droplet and we close the container filled with water and the sample at its bottom with a lid. We use a parallel monochromatic light source for illumination, and record the dissolution process with a PCO.pixelfly camera. We analyze the images taken by the camera with a MATLAB code, and determine the lateral diameter $L$, the height $H$ and the contact angle $\theta$ of the droplet. We find that the droplets dissolve in the stick-slide mode and the stick-jump mode. For wafers with low contact angle hysteresis, presumably with a small pyramidal hillock density, the droplets dissolve solely in the stick-slide mode. The reason for this are relatively weak pinning sites on the surface or the lack of pinning sites on the surface. We find that the initial contact angle $\theta_0$ is smaller for the etched wafer than the unetched wafers. In some cases it becomes considerably small. This is in agreement with Wenzel's model, which suggest that surface roughness enhances the wettability of the surface. However it should be noted that $\theta_0$ is also dependent on the way of deposition of the droplet. Furthermore we find that the contact angle at which the droplet depins also becomes smaller for the etched wafers compared to the unetched wafers. However, the results of the depinning contact angle $\theta_d$ are also inconsistent compared to the amount of etching time, due to the spatial variation of the pyramidal hillocks. This causes a difference in pinning force, and thus a variation in depinning angles. For droplets dissolving in the stick-jump mode the difference between $\theta_d$ and the contact angle it jumps to right after depinning, $\theta_j$, is small in some cases. The reason for this is two fold: low surface defect density and different pinning strength of the contact line by the pyramidal hillocks. These results imply that we are not able to predict in which mode the droplet dissolves as a function of the etching time or at which angle the droplet depins. We think that the size of the pyramidal hillocks does not effect the pinning force, but it rather depends on the inclination of these planes, i.e. substrates covered with a larger density of pyramidal hillocks and/or substrates with larger pyramidal hillocks, do not exert larger pinning strengths on the droplet. For the glass and silicon samples covered with nanopancakes, we find that the droplets dissolve solely in the stick-jump mode.

# CHAPTER 7

## Conclusions and Recommendations

Our main interest is in the contact line dynamics of dissolving sessile droplets. Therefore we perform an experimental and numerical study on dissolving droplets surrounded by another fluid and deposited on (patterned) substrates.

We employ the lattice Boltzmann model and the evaporation model from Hessling et al. [1] to study the contact line dynamics of sessile droplets numerically. From the benchmark of the free spherical droplet in the system center surrounded by still liquid, we conclude that the system size affects the measured diffusion constants. The measured diffusion constant becomes smaller if we increase the distance to the evaporation boundary. This originates from the infinite system assumption in the theory. We also find that the diffusion constant becomes larger if the fluid-fluid interaction parameter $g_{br}$ increases. However, one would expect that the diffusion constant becomes smaller, because the repulsive force between the fluids from the Shan-Chen model becomes larger with increasing $g_{br}$. An explanation for this is the fact that surface tension is neglected and the fact that the system size affects the results of the measured diffusivity. We are able to simulate the droplets dissolving in different modes by patterning the surfaces: the constant contact angle (CA) mode, partly the constant radius (CR) mode, the stick-slide mode and the stick-jump mode. For the CA mode we use flat surfaces, for the CR and stick-slide mode we use a hydrophobic surface with one hydrophylic disk and for the stick-jump mode we use a configuration where we switch between hydrophylic and hydrophobic rings. We fit our data to analytical solutions to find the diffusion constant. At the end of the simulation the data deviates from the analytical solution, due to the fact that the droplet becomes so small that the surface tension becomes significant. We find that the lifetime of the droplet matches the theory and that the droplet dissolve faster in the CR mode than in the CA mode. From all of the simulations it is clear that in order to reach convergence for the measured diffusivity in the system, we need to use larger systems for the simulations. Larger system sizes will better match the infinite system assumption. Another solution is to find analytical equations that explicitly account for the system size, from which we can find the diffusivity in the system. This will make it possible to study the evaporation of droplets in finite systems. Also if we increase the system size, it will be possible to simulate droplets which dissolve for a longer time in the CR mode, i.e. we can simulate larger droplets such that there is enough fluid in the system for the droplet to dissolve in the CR mode. To improve the results for the dissolving sessile droplets, it would be good to use a spherical evaporation boundary instead of a flat plane. This would result in a homogeneous density gradient in the system.

In the numerical part we study droplets on chemically patterned surfaces, whereas for the experimental part we study the dynamics of sessile droplets on surfaces with physical heterogeneities. We apply an anisotropic chemical etching process for this purpose. The chemical etching process results in pyramidal hillocks randomly distributed on the samples of each wafer. We measure the advancing and receding contact angle (ARCA) on three different spots on three different samples from each wafer. We study two systems: water droplets in air and 1-hexanol droplets in water. It is difficult to compare the results of these two systems, since they have not been performed on the exact same positions on the samples. This can be solved in the future by cutting the samples in such a shape that is recognizable in which area one should measure the hysteresis or mark the spots at the back of each sample or one should consider another method to apply roughness on the surface for more reproducible results. We have seen that the amount of etching time did not influence the depinning contact angle of the dissolving droplets during the experiment. We conclude that the depinning contact angle rather depends on the inclination angle of the pyramidal surface than the size of these pyramidal hillocks.

In the experiments we observe that the surface droplets dissolve in the stick-slide and the stick-jump mode. Moreover, we find that for surfaces with low contact angle hysteresis, presumably covered with low pyramidal hillock density, the droplets only dissolve in the stick-slide mode. In general we know from our numerical results, that if there are more hydrophylic disks on the surface the droplet “jumps” to the next available hydrophylic position on the surface and thus dissolves in the stick-jump mode. This implies that we observe the stick-slide mode in experiments only if the droplet does not encounter other pinning sites on the surface. We indeed find with our simulations, that the droplet dissolves in the stick-slide mode if our surface only has one hydrophylic disk. Another reason why we do not always observe the stick-jump mode in experiments, is due to optical limitations, i.e. the jumps might be too small to observe it with optical instruments.

A more systematic numerical study can be performed on the behaviour of dissolving droplets on surfaces covered with e.g., pyramidal hillocks or other randomly distributed physical heterogeneities. For this a LB3D approach can be used with an addition of the Shan-Chen model and evaporation model developed by Hessling et al. [1]. With the numerical simulations we can for instance confirm if the depinning contact angle depends on the size of these pyramidal hillocks. But this also gives us the opportunity to study the dynamics of dissolving surface droplets on other geometries than flat surfaces. Moreover, by adding surfaces roughness in a controlled way in both experiments and numerical simulations, which is of course more complicated in the former, we can study the influence of pinning sites on droplets and bubbles. With this we can confirm the theory of Lohse and Zhang [14] that explains the stabilizing effect by pinning sites on nanobubbles. Also other chemical patterns can be added to the surfaces to study the bottom view of the droplet when it depins in the stick-slide or stick-jump mode. We are then able to view in which way the contact line retracts during the jump phase. We have studied the dissolution of single droplets, but we know that systems where droplets are surrounded by neighbouring droplets are of equal importance and relevance. Laghezza et al. [53] have studied such systems both numerically and experimentally. We can extend their work by adding convection in the system. This would give us insight in how natural convection will influence the lifetime in a neighbouring droplet system. But first it is important to test the applicability of scaling relations given by Dietrich et al. [54] for droplets dissolving through natural convection and diffusion. We have studied systems of single fluid droplets. We can extend our work in the future by studying binary or multicomponent droplets. It is especially interesting how the contact line dynamics and lifetime of binary or multicomponent droplets will change compare to single fluid droplets. For instance, how will the depinning contact angle of the droplet change with composition of the droplet?

# Bibliography

[1] Dennis Hessling, Qingguang Xie, and Jens Harting: ‘A diffusion based evaporation method in multicomponent lattice Boltzmann system’. preprint (cit. on pp. c, 3, 19, 25, 46, 71, 72).

[2] Paul S Epstein and Milton S Plesset: ‘On the Stability of Gas Bubbles in Liquid-Gas Solutions’. In: *The Journal of Chemical Physics* (1950), vol. 18(11): pp. 1505–1509 (cit. on pp. c, 3, 9, 25, 46).

[3] Jutta M Stauber, Stephan K Wilson, Brian R Duffy, and Khellil Sefiane: ‘On the lifetimes of evaporating droplets’. In: *Journal of Fluid Mechanics* (2014), vol. 744: R2 (cit. on pp. 1, 10, 11, 37, 38).

[4] RG Picknett and R Bexon: ‘The evaporation of sessile or pendant drops in still air’. In: *Journal of Colloid and Interface Science* (1977), vol. 61(2): pp. 336–350 (cit. on pp. 1, 9, 10).

[5] Erik Dietrich, E Stefan Kooij, Xuehua Zhang, Harold JW Zandvliet, and Detlef Lohse: ‘Stick-jump mode in surface droplet dissolution’. In: *Langmuir* (2015), vol. 31(16): pp. 4696–4703 (cit. on pp. 1, 2, 10–12, 42).

[6] Detlef Lohse, Xuehua Zhang, et al.: ‘Surface nanobubbles and nanodroplets’. In: *Reviews of modern physics* (2015), vol. 87(3): p. 981 (cit. on pp. 1, 6).

[7] Xuehua Zhang, Jun Wang, Lei Bao, Erik Dietrich, Roeland C. A. van der Veen, Shuhua Peng, James Friend, Harold J. W. Zandvliet, Leslie Yeo, and Detlef Lohse: ‘Mixed mode of dissolving immersed nanodroplets at a solid-water interface’. In: *Soft Matter* (10 2015), vol. 11: pp. 1889–1900 (cit. on pp. 1, 2, 6, 7, 9–11, 32, 51, 63).

[8] H Yildirim Erbil: ‘Evaporation of pure liquid sessile and spherical suspended drops: A review’. In: *Advances in Colloid and Interface Science* (2012), vol. 170(1): pp. 67–86 (cit. on p. 1).

[9] Aijing Ma, Jie Xu, Li Yu, Xuehua Zhang, Dayang Wang, and Haolan Xu: ‘Adsorbed emulsion droplets: capping agents for in situ heterogeneous engineering of particle surfaces’. In: *Chemical Communications* (2013), vol. 49(98): pp. 11563–11565 (cit. on p. 1).

[10] Feng-Chao Wang and Heng-An Wu: ‘Pinning and depinning mechanism of the contact line during evaporation of nano-droplets sessile on textured surfaces’. In: *Soft Matter* (2013), vol. 9(24): pp. 5703–5709 (cit. on p. 1).

[11] Antonio Méndez-Vilas, Ana Belén Jódar-Reyes, and Mar´ia Luisa González-Mart´in: ‘Ultrasmall liquid droplets on solid surfaces: production, imaging, and relevance for current wetting research’. In: *small* (2009), vol. 5(12): pp. 1366–1390 (cit. on p. 1).

[12] Melanie Ramiasa, John Ralston, Renate Fetzer, Rossen Sedev, Doris M Fopp-Spori, Christoph Morhard, Claudia Pacholski, and Joachim P Spatz: ‘Contact line motion on nanorough surfaces: A thermally activated process’. In: *Journal of the American Chemical Society* (2013), vol. 135(19): pp. 7159–7171 (cit. on pp. 1, 60, 69).

[13] David Quéré: ‘Surface wetting: Model droplets’. In: *Nature Materials* (2004), vol. 3(2): pp. 79–80 (cit. on p. 1).

[14] Detlef Lohse, Xuehua Zhang, et al.: ‘Pinning and gas oversaturation imply stable single surface nanobubbles’. In: *Physical Review E* (2015), vol. 91(3): p. 031003 (cit. on pp. 1, 73).

[15] Shiyi Chen and Gary D Doolen: ‘Lattice Boltzmann method for fluid flows’. In: *Annual review of fluid mechanics* (1998), vol. 30(1): pp. 329–364 (cit. on p. 3).

[16] Haibo Huang, Daniel T Thorne Jr, Marcel G Schaap, and Michael C Sukop: ‘Proposed approximation for contact angles in Shan-and-Chen-type multicomponent multiphase lattice Boltzmann models’. In: *Physical Review E* (2007), vol. 76(6): p. 066701 (cit. on pp. 3, 17–19, 21).

[17] Roberto Benzi, Mauro Sbragaglia, Sauro Succi, Massimo Bernaschi, and Sergio Chibbaro: ‘Mesoscopic lattice Boltzmann modeling of soft-glassy systems: theory and simulations’. In: *The Journal of Chemical Physics* (2009), vol. 131(10): p. 104903 (cit. on p. 3).

[18] Pierre-Gilles De Gennes, Françoise Brochard-Wyart, and David Quéré: *Capillarity and wetting phenomena: drops, bubbles, pearls, waves.* Springer Science & Business Media, 2013 (cit. on p. 5).

[19] Thomas Young: ‘An essay on the cohesion of fluids’. In: *Philosophical Transactions of the Royal Society of London* (1805), vol.: pp. 65–87 (cit. on p. 5).

[20] David Quéré: ‘Wetting and roughness’. In: *Annu. Rev. Mater. Res.* (2008), vol. 38: pp. 71–99 (cit. on p. 5).

[21] Robert N Wenzel: ‘Surface Roughness and Contact Angle.’ In: *The Journal of Physical Chemistry* (1949), vol. 53(9): pp. 1466–1467 (cit. on p. 6).

[22] ABD Cassie and S Baxter: ‘Wettability of porous surfaces’. In: *Transactions of the Faraday Society* (1944), vol. 40: pp. 546–551 (cit. on p. 6).

[23] Edward Lansing Cussler: *Diffusion: mass transfer in fluid systems*. Cambridge university press, 2009 (cit. on p. 7).

[24] Walter H Corkern and Linda L Munchausen: ‘Solubility of alcohols’. In: *Journal of Chemical Education* (1992), vol. 69(11): p. 928 (cit. on p. 7).

[25] Robert D Deegan, Olgica Bakajin, Todd F Dupont, Greb Huber, Sidney R Nagel, and Thomas A Witten: ‘Capillary flow as the cause of ring stains from dried liquid drops’. In: *Nature* (1997), vol. 389(6653): pp. 827–829 (cit. on pp. 7, 10).

[26] Hua Hu and Ronald G Larson: ‘Evaporation of a sessile droplet on a substrate’. In: *The Journal of Physical Chemistry B* (2002), vol. 106(6): pp. 1334–1344 (cit. on pp. 7, 10).

[27] Yuri O Popov: ‘Evaporative deposition patterns: spatial dimensions of the deposit’. In: *Physical Review E* (2005), vol. 71(3): p. 036313 (cit. on pp. 7, 8, 10).

[28] Martin ER Shanahan: ‘Simple theory of” stick-slip” wetting hysteresis’. In: *Langmuir* (1995), vol. 11(3): pp. 1041–1043 (cit. on pp. 10, 11, 36).

[29] Melik Oksuz and H Yildirim Erbil: ‘Comments on the Energy Barrier Calculations during “Stick–Slip” Behavior of Evaporating Droplets Containing Nanoparticles’. In: *The Journal of Physical Chemistry C* (2014), vol. 118(17): pp. 9228–9238 (cit. on pp. 11, 36).

[30] Hendrik Patrick Jansen: ‘Droplet dynamics on chemically striped patterned surfaces: An experimental and computational study’. PhD thesis. Universiteit Twente, 2014 (cit. on pp. 13–15, 19).

[31] D Raabe: ‘Overview of the lattice Boltzmann method for nano-and microscale fluid dynamics in materials science and engineering’. In: *Modelling and Simulation in Materials Science and Engineering* (2004), vol. 12(6): R13 (cit. on pp. 14, 15).

[32] MC Sukop: ‘DT Thorne, Jr. Lattice Boltzmann Modeling Lattice Boltzmann Modeling’. In: (2006), vol. (cit. on pp. 14–17, 21).

[33] Shiyi Chen and Gary D Doolen: ‘Lattice Boltzmann method for fluid flows’. In: *Annual review of fluid mechanics* (1998), vol. 30(1): pp. 329–364 (cit. on p. 15).

[34] Xiaoyi He and Li-Shi Luo: ‘Theory of the lattice Boltzmann method: From the Boltzmann equation to the lattice Boltzmann equation’. In: *Physical Review E* (1997), vol. 56(6): p. 6811 (cit. on p. 16).

[35] Sauro Succi: *The lattice Boltzmann equation: for fluid dynamics and beyond*. Oxford university press, 2001 (cit. on pp. 16, 17).

[36] Prabhu Lal Bhatnagar, Eugene P Gross, and Max Krook: ‘A model for collision processes in gases. I. Small amplitude processes in charged and neutral one-component systems’. In: *Physical review* (1954), vol. 94(3): p. 511 (cit. on p. 16).

[37] Martin Hecht and Jens Harting: 'Implementation of on-site velocity boundary conditions for D3Q19 lattice Boltzmann simulations'. In: *Journal of Statistical Mechanics: Theory and Experiment* (2010), vol. 2010(01): P01018 (cit. on pp. 16–18, 21).

[38] Xiaowen Shan and Gary Doolen: 'Diffusion in a multicomponent lattice Boltzmann equation model'. In: *Physical Review E* (1996), vol. 54(4): p. 3614 (cit. on pp. 17, 20).

[39] Xiaowen Shan and Hudong Chen: 'Lattice Boltzmann model for simulating flows with multiple phases and components'. In: *Physical Review E* (1993), vol. 47(3): p. 1815 (cit. on p. 18).

[40] Xiaowen Shan and Hudong Chen: 'Simulation of nonideal gases and liquid-gas phase transitions by the lattice Boltzmann equation'. In: *Physical Review E* (1994), vol. 49(4): p. 2941 (cit. on p. 18).

[41] Sebastian Schmieschek and Jens Harting: 'Contact angle determination in multicomponent lattice Boltzmann simulations'. In: *arXiv preprint arXiv:0910.3915* (2009), vol. (cit. on p. 18).

[42] P Brent Duncan and David Needham: 'Microdroplet dissolution into a second-phase solvent using a micropipet technique: test of the Epstein-Plesset model for an aniline-water system'. In: *Langmuir* (2006), vol. 22(9): pp. 4190–4197 (cit. on pp. 25, 26, 28).

[43] Jonathan T Su and David Needham: 'Mass transfer in the dissolution of a multicomponent liquid droplet in an immiscible liquid environment'. In: *Langmuir* (2013), vol. 29(44): pp. 13339–13345 (cit. on pp. 25, 28).

[44] Erwin Berthier and David J Beebe: 'Flow rate analysis of a surface tension driven passive micropump'. In: *Lab on a Chip* (2007), vol. 7(11): pp. 1475–1478 (cit. on p. 30).

[45] Lei Bao, Zenon Werbiu, Detlef Lohse, and Xuehua Zhang: 'Controlling the Growth Modes of Femtoliter Sessile Droplets Nucleating on Chemically Patterned Surfaces'. In: *The journal of physical chemistry letters* (2016), vol. (cit. on p. 36).

[46] Arzu Colak: *Measuring adhesion forces between hydrophilic surfaces with atomic force microscopy using flat tips*. Universiteit Twente, 2013 (cit. on pp. 49, 50, 55).

[47] Richard Stephenson, James Stuart, and Mary Tabak: 'Mutual solubility of water and aliphatic alcohols'. In: *Journal of chemical and engineering data* (1984), vol. 29(3): pp. 287–290 (cit. on p. 52).

[48] Ling Hao and Derek G Leaist: 'Binary mutual diffusion coefficients of aqueous alcohols. Methanol to 1-heptanol'. In: *Journal of Chemical & Engineering Data* (1996), vol. 41(2): pp. 210–213 (cit. on p. 52).

[49] MA Gosálvez, K Sato, AS Foster, RM Nieminen, and H Tanaka: ‘An atomistic introduction to anisotropic etching’. In: *Journal of Micromechanics and Microengineering* (2007), vol. 17(4): S1 (cit. on p. 55).

[50] MA Gosálvez and RM Nieminen: ‘Surface morphology during anisotropic wet chemical etching of crystalline silicon’. In: *New Journal of Physics* (2003), vol. 5(1): p. 100 (cit. on pp. 55, 56).

[51] SMM Ramos, E Charlaix, and A Benyagoub: ‘Contact angle hysteresis on nano-structured surfaces’. In: *Surface science* (2003), vol. 540(2): pp. 355–362 (cit. on pp. 60, 69).

[52] SMM Ramos, E Charlaix, A Benyagoub, and M Toulemonde: ‘Wetting on nanorough surfaces’. In: *Physical Review E* (2003), vol. 67(3): p. 031604 (cit. on pp. 60, 69).

[53] Gianluca Laghezza, Erik Dietrich, Julia M Yeomans, Rodrigo Ledesma-Aguilar, E Stefan Kooij, Harold JW Zandvliet, and Detlef Lohse: ‘Collective and convective effects compete in patterns of dissolving surface droplets’. In: *Soft matter* (2016), vol. (cit. on p. 73).

[54] Erik Dietrich, Sander Wildeman, Claas Willem Visser, Kevin Hofhuis, E Stefan Kooij, Harold JW Zandvliet, and Detlef Lohse: ‘Role of natural convection in the dissolution of sessile droplets’. In: *Journal of Fluid Mechanics* (2016), vol. 794: pp. 45–67 (cit. on p. 73).

# Acknowledgments

This thesis would not have been completed without the help of a number of people.

First of all, I want to thank Detlef for giving me the opportunity to work on my master thesis in the Physics of Fluids group. Detlef thank you for giving me the opportunity to attend a conference and Summer School on lattice Boltzmann modeling. You always encourage people in an excellent way and provide an excellent research environment. Jens thank you for giving me the opportunity to work on a numerical project. Before starting this project, I did not have enough experience with numerical work, but this project has definitely contributed to my expertise. I have appreciated your critical questions and comments to keep me on track. Also I want to thank the people from your group in Eindhoven, especially Dennis and Qingguang. Dennis many thanks for spending your precious time to guide me through this project. I know that I have even challenged your patience sometimes, but you have always been critical, supportive and willing to help. So once again my sincere gratitude to you! Erik you have been a great mentor. You guided me well and I gained more experience on cleaning procedures and conducting experiments. You are always very patient and friendly and above that you explain everything really well. Thanks Erik!

Shantanu and Stefan I owe you a big thank you for your approval to take part in my defense committee!

I would like to thank all the students of the master room. Also a special thanks to Christa, Dennis, Leonie, Martin, Mathijs, Mirjam, Pilar, Rodrigo, Sebastian and Yaxing for the nice and diverse diners we enjoyed together. Mirjam, Leonie and Sebastian, you guys made the Roti so perfect for the first time, that I will always remember it. I have not even tried it to make it myself. So all the credit to you guys!

Rudy, I have always enjoyed working with you on our assignments. You were always very helpful and I have learned a lot from you. Thank you! And yes we even manged to successfully complete the Experimental Techniques in Physics of Fluids course after two years. Something we still have to celebrate!

A very special thanks to Anil, Arnoud, Dave, Jinhua, Lorenzo and Viola for a really nice IAESTE Twente Board experience.

And Twente feels as home because of all the Surinamese students in Twente. I especially enjoy our Christmas diners and yearly borrels. Gran tangi! Especially Cyrano and Nelson thank you for your invaluable support and friendship! Chefiek thanks for your help on the nice images in this thesis and especially your help with the cover page image!

A special thanks to the Anton de Kom University of Suriname for granting me a scholarship to study Applied Physics at the University of Twente.

And last but not least I want to thank my family and friends in Suriname, especially my grandmother for her invaluable moral support and for being present at my defense!